A Practical and Optimal Approach to CNC Programming for Five-Axis Grinding of the End-Mill Flutes

Mahmoud Mohammad Rababah

A Thesis
in
The Department
of
Mechanical and Industrial Engineering

Presented in Partial Fulfillment of the Requirements

for the Degree of Doctor of Philosophy (Mechanical Engineering) at

Concordia University

Montreal, Quebec, Canada

September, 2011

CONCORDIA UNIVERSITY
SCHOOL OF GRADUATE STUDIES

This is to certify that the thesis prepared

By: Mahmoud Rababah

Entitled: A Practical and Optimal Approach to CNC Programming for Five-Axis Grinding of the End-Mill Flutes

and submitted in partial fulfillment of the requirements for the degree of

Doctor of Philosophy (Mechanical Engineering)

complies with the regulations of the University and meets the accepted standards with respect to originality and quality.

Signed by the final examining committee:

Dr. A.C. Lopes	Chair
Dr. Deyi Xue	External Examiner
Dr. W. Tian	External to Program
Dr. M. Chen	Examiner
Dr. O. Kuzgunkaya	Examiner
Dr. Z.C. Chen	Thesis Supervisor

Approved by

Chair of Department or Graduate Program Director

Dean of Faculty

Abstract

A Practical and Optimal Approach to CNC Programming for Five-Axis Grinding of the End-Mill Flutes

Mahmoud M. Rababah, PhD.

Concordia University, 2011

For a solid carbide tapered end-mill, every flute includes a flute surface and a rake face along a helical side cutting edge, and the end-mill core is at the center and is tangent to all the flutes. The flutes significantly affect the tools cutting performance and life, and the core radius mainly affects the tools rigidity. Mainly, two methods are adopted in industry to grind the flutes; these are: the direct method and the inverse method. In the direct method, a flute is ground using a standard grinding-wheel moving in multi-axis machining to generate the rake face and the flute surface. However, the flute is the natural outcome of the grinding process without any control. On the other side, the inverse method employs the concept of inverse engineering to build a grinding-wheel that accurately grinds the end-mill flutes. This yields a free-form grinding-wheel profile that is used on a 2-axis grinding machine; however, the flute shapes are only exact on one section of the end-mill; when the grinding-wheel moves along the side cutting edge to smaller sections; the deviation of the generated flute from the designed one will be increased. Thus, neither can this method grind the rake face with the prescribed normal rake angle, nor generate the side cutting edge in good agreement with its design. Moreover, the grinding-wheel profile is very difficult and expensive to make.

To address these problems, a practical and optimal approach for five-axis grinding of prescribed end-mill flutes is proposed by; first, establishing a 5-axis flute grinding theory describing the wheels locations and orientations during grinding the rake faces with constant normal rake angles; Second, introducing a simple grinding-wheel consisting of lines and circular arcs; and finally, applying an optimization algorithm to optimize the grinding-wheel shape and path. Overall, this approach significantly advances the CNC programming technique for the 5-axis flute grinding, and can substantially increase the quality of the solid carbide end-mills and lays a good foundation for the CAD/CAE/CAM of end-mills. The advantages of this approach over the other approaches are verified using computer simulation.

Dedication

To my parents, my wife and my two kids; Osamah and Qais.

Acknowledgments

I would like to express my great thanks and appreciations to my supervisor Dr. Chevy Chen for his guidance and support during the period of my PhD. work. His way of guidance developed my research experience and significantly improved my technical skills.

I also would like to show my sincere appreciation to my fellows and friends in the CAD/CAM lab. (Maqsood Khan, Muhammad Wasif, Aqeel Ahmad and Xie Shuangxi). The warm environment we had in the lab. and the support I got from them encouraged me to pursue and improve my ideas for the research. Among them, special and big thanks to Maqsood Khan, for his endless supports and creative advices.

Finally, I sincerely thank my wife for her support and patience.

Contents

List of Figures

List of Tables

Chapter 1

Introduction

1.1 Research Problems

Complex parts machining requires the use of different conventional and non conventional cutting tool shapes. While flat end-mills are sufficient for $2\frac{1}{2}$D machining and some surface finish functions, more complicated tools are needed for more complex parts where multi-axis machining is involved. End-mill cutting tools can be cylindrical flat end-mill, fillet end-mill, taper ball end-mill, etc. (Fig. 1.1). The end-mill cutting tools are normally generated using milling or grinding operations. The efficiency of the generated end-mills is mainly dependent on the material used and the geometry obtained. The end-mill cutting tool material should satisfy toughness, hot hardness and wear resistance properties required to perform the cutting operations. The geometry has direct impact on the tool strength, the chip evacuation capabilities, the tool dynamics and the tool life. It can be described mainly by the cutting edges and the tool flutes.

While milling can be sufficient to produce end-mills from high speed steel

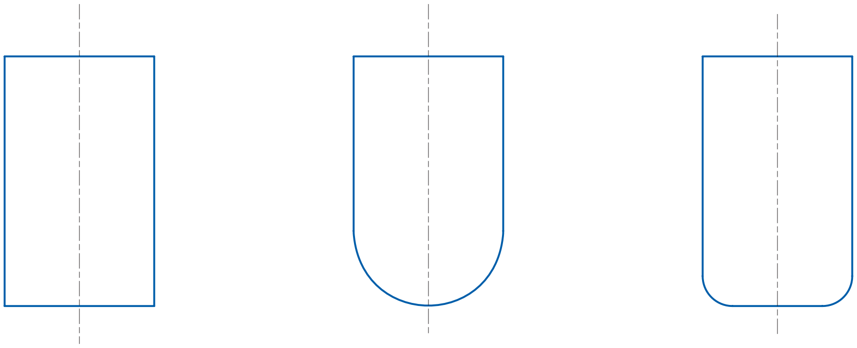

(a) Cylindrical (b) Ball end (c) Fillet end

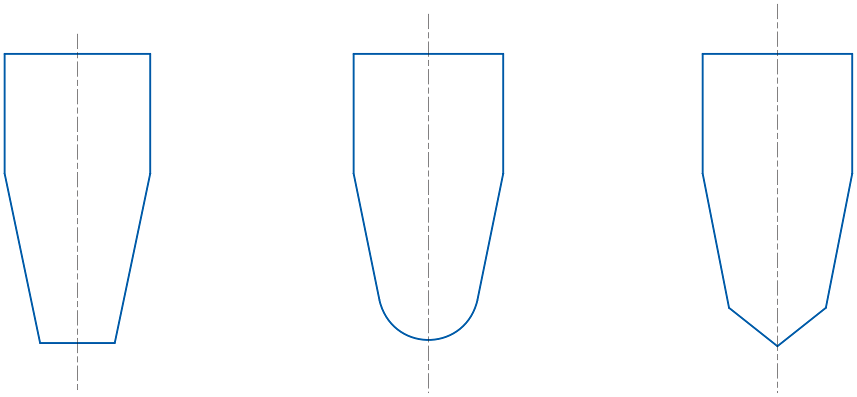

(d) Tapered flat end (e) Tapered ball end (f) Cone end

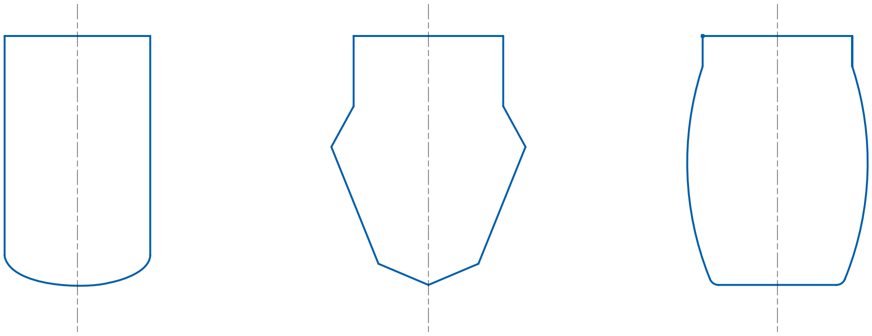

(g) Rounded end (h) Inverted cone end (i) Circular arc generatrix

Figure 1.1: Different shapes of end-mill cutting tools.

workpieces, it is not sufficient for harder materials as carbide or ceramics. Thus, grinding will be involved. It can be defined as a material-removal process in which abrasive particles (grains) are contained in a bonded grinding-wheel operating at a high speed [1]. The grinding-wheels are normally of standard shapes (Fig. 1.2) that are precisely balanced for high rotational speeds. However, non-standard wheels can sometimes be involved to perform specific grinding functions. Grinding is considered as a multi-points cutting process in which some of the randomly positioned and oriented grains will be engaged with the workpiece and perform cutting, plowing or rubbing operations depending on the orientations of the grains and their rake angles.

Analogues to milling; grinding has many cutting teeth engaged with the workpiece at the same time, the workpiece is fed relative to the grinding-wheel, and face and peripheral grinding can be conducted. Despite these similarities, major differences exist; these are: the cutting teeth of the engaged grains are more numerous than the cutting points in milling, cutting speeds are much higher, no unique rake angle exists for the grinding-wheels and, on average, these rake angles are of very high negative values. Moreover, more control can be achieved on the final parts dimensions.

Grinding operations in general can be categorized into [2]: (a) Surface grinding which is the most common operation that generally involves grinding of flat surfaces. (b) Cylindrical grinding operations grind the external surface of the workpiece (crankshaft bearings, spindles, pins, etc.) using traverse, plunge or profile grinding. (c) Internal grinding using small wheels to grind the inside diameter of the

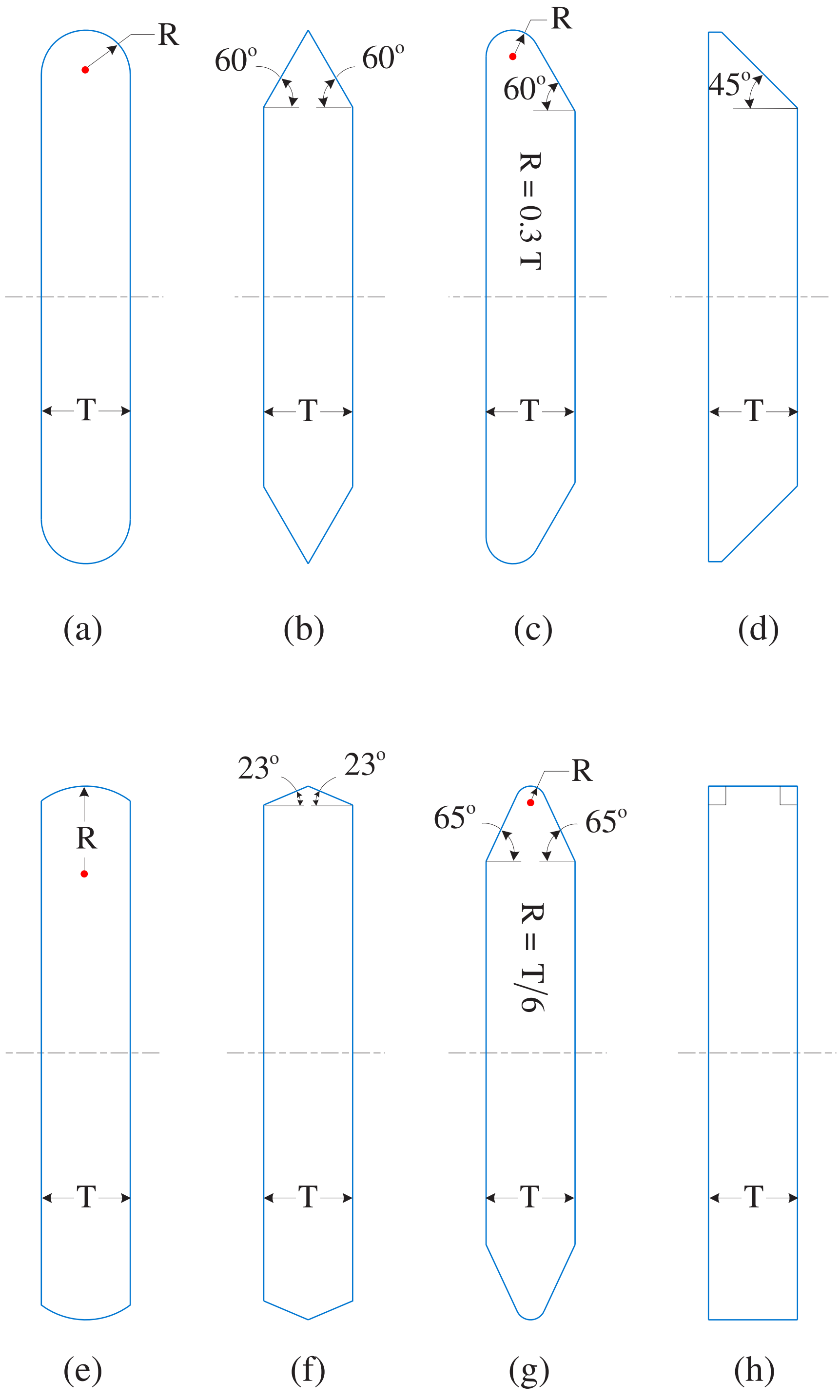

Figure 1.2: Some of standard grinding-wheel shapes.

workpiece. (d) Centerless grinding which is a high production process for continuously grinding cylindrical surfaces where the workpiece is not supported by centers. (e) Other grinding operations including tool grinding, heavy stock removal grinding, creep feed grinding, etc.

Since our concern in this dissertation is the end-mill grinding, it will be explored in details in the coming chapters. However, it can be mainly categorized into: (1) two-axis end-mill grinding using non-conventional grinding-wheels (inverse method), (2) multi-axis end-mill grinding using standard grinding-wheels (direct method) and (3) novel multi-axis tool grinding using a novel grinding-wheel that is optimized together with its path to generate accurate flute shapes [3]- [6] .

As the two-axis and the multi-axis grinding processes available both do not have much control on the end-mill shapes, the ground flutes will not be optimal for tool dynamics, tool strength and chip evacuations. Also, the processes will be unable to produce end-mills matching the optimally designed ones; leading to inaccurate cutting analysis. Thus, the need arises for a novel process that can better control the flutes shapes and ensures accurate cutting edges and constant normal rake angles along those edges. With the novel multi-axis grinding theory introduced in this dissertation, a simple prismatic grinding-wheel consisting of lines and circular arcs is adopted to grind end-mill cutting tools using five-axis CNC grinding machines. The wheel path and geometry are both optimized for more accurate tool flute shapes, accurate cutting edges and constant normal rake angles along those edge.

1.2 Research Objectives

The first objective of this work is to establish a five-axis tool grinding theory. Thus, the grinding-wheel location and orientation will be described during the grinding process using explicit mathematical representations. This is carried out while ensuring an accurate side cutting edge and a constant normal rake angle along that edge. The grinding-wheel will follow the side cutting edge in similar manner to a cutter in milling process when it follows the set of the cutter contact points (CC points).

The second objective is to grind the end-mill flutes with close matching to the designed ones. This is achieved by optimizing the geometric parameters and the path of the grinding-wheel. The grinding-wheel is of a novel shape and is first introduced in this dissertation. It can represent many of standard grinding-wheels already available in industry.

As a result, a true tool model will be generated that can be directly used in the finite element analysis to accurately predict the tool strength and dynamics during the cutting process. It is unlike the available tool models which are based only on design and are unattainable in a real manufacturing process.

1.3 Dissertation Organization

The remaining sections of this dissertation are organized as follows. Chapter 2 reviews the concept of the swept surface and the current approaches to obtain it. It also discusses the current tool grinding processes and the improvements that has been gained in the last few years. Chapter 3 simulates one of the main grinding processes currently available in academia and industry; that is the inverse method. The advantages and the disadvantages of this method will also be highlighted in this chapter. Chapter 4 will establish a five-axis tool grinding theory and will derive the grinding-wheel location and orientation during the grinding process (wheel path) in order to grind the end-mill flutes with accurate side cutting edges and constant normal rake angles along those edges. Chapter 5 will introduce a novel grinding-wheel profile consisting of lines and circular arcs. The profile of the grinding-wheel will be optimized with its path in order to grind the tool flutes with close matching to the designed ones. Chapter 6 contains the summary of this work and the future work the author is intending to pursue.

Chapter 2

Literature Review

This chapter reviews the concept of the swept surface, its importance to the grinding process and the methods available to generate it. Then, a comprehensive review for the grinding processes described in literature and adopted in industry is conducted.

2.1 Grinding–Wheel Swept Volume

The importance of the swept volume in CAD/CAM comes from its role in (1) calculating the cutter-workpiece engagements for the cutting force calculations [7] - [11] and (2) machining simulation as many software codes are already available in hands (eg. Catia and MasterCam). The in-process workpiece can be updated every tool path step by subtracting the swept volume generated from the workpiece using the Boolean operation (Fig. 2.1). This will give the CAD/CAM engineer an insight on the final product without the need to do real machining. Hence, the design-machining cycle will be reduced and will be more efficient.

The swept volume can be defined as the volume generated from moving an object (generator) along a prescribed path. Moving a sphere along a circular path

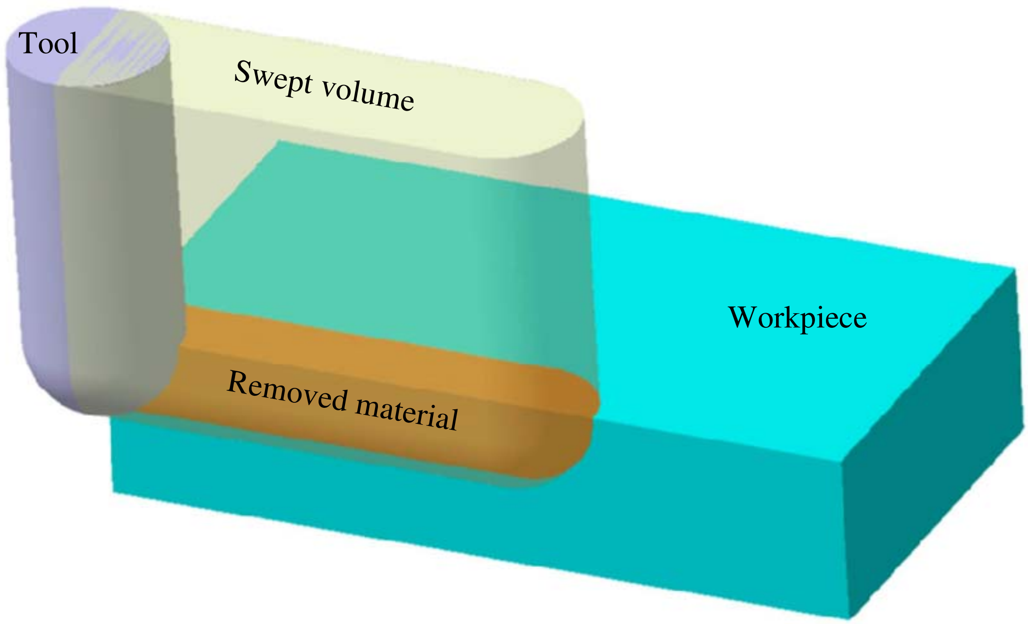

Figure 2.1: In-process workpiece updated using the swept volume.

generates a torus shape swept volume (Fig. 2.2). Most researchers explore generating the swept volume of cutting tools following a specific tool path in multi-axis CNC machines. However, there is no closed-form expression for the swept volume of cutting tools moving in a general multi-axis motion [12]. One way around this is to use the swept surface (also called the swept envelope) instead of the swept volume.

The swept envelope is defined as the enclosing envelope that is constructed of the intermediate swept profiles of the cutting tool. A general method for developing the envelope was introduced by Wang and Wang [13] and Sambandan and Wang [14]. A moving Frenet frame with an origin coincides with a reference point on the moving cutter was proposed in order to extend the domain of the parametric equation of the cutting tool to 4D space. The fourth dimension can be eliminated by considering the fact that the velocity vector of any point on the swept envelope should be tangential

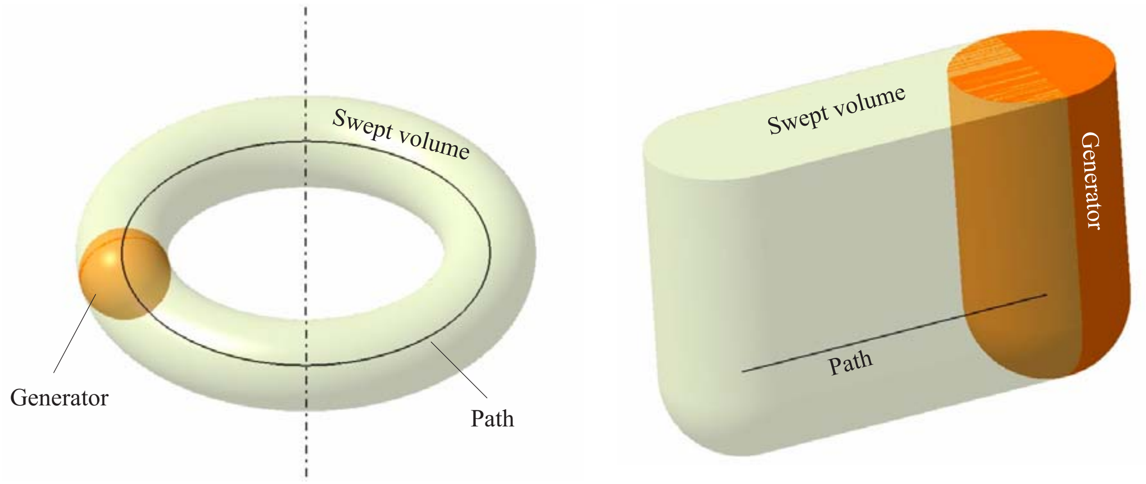

Figure 2.2: Swept volume generated by moving the generator along a prescribed path.

to the envelope.

Chung *et al.* [15] developed their approach to generate the swept envelope for three-axis cutter motion by modeling the swept envelope in a single-valued form as a family of tangential curves (silhouette curves). However, a forth order polynomial needs to be solved for each silhouette curve and the approach is not extendable to a higher axis motion.

Chiou and Lee [16] proposed one method that provides a parametric solution for the swept envelope of a generalized cutter. They considered the kinematics of one specific five-axis machine and then obtained the velocity at each point of the generalized cutter from that machine kinematics. The swept envelope was obtained based on the envelope theory, that is, the velocity vector of any point on the swept envelope should be tangential to the envelope.

Since the envelope was obtained in a parametric form, it was not possible to represent it as a simple surface, thus, an approximation algorithm was proposed by Weinert *et al.* [17] to represent the envelope as a NURBS surface. The method is robust and can be applied to the material removal simulations using the Boolean operation. However, the envelope was generated for cylindrical and fillet-end cutters only, and not for general shape cutters.

Du *et al.* [18] proposed, using the rigid body motion theory, a moving frame on the cutter surface. A parametric closed-form solution of the swept envelope was obtained for generalized cutter shapes. The developed method can be used for NC simulation and verification.

Simpler and more generic swept envelope formulation based on the tangency condition in the envelope theory was proposed by Li *et al.* [19], the simplicity in his method comes from dealing with the surface of the cutter as a revolving surface in the cutter moving frame instead of using the generic cutter shape geometry. Also, the method proposed by Aras [20] developed a parametric representation of the swept envelope for general cutter shapes in multi-axis milling using two families of spheres. The surface of the cutter was modeled as a canal surface constructed from generating circles. Those generating circles are obtained from the tangency of the first family of spheres with the cutter surface. The second family of spheres, representing the cutter motion, generates characteristic circles in directions normal to the spheres motions. The intersection points between the generating circles and the characteristic circles lie on the swept envelope.

While all the aforementioned researchers obtained parametric closed-form solutions for the swept envelope, Chen and Wei [21] developed an efficient and accurate approach to generate an explicit closed-form solution for the swept envelope. The cutter was modeled as a set of thin disks. The disks generate a family of circles at each specific height that can be enclosed by an envelope profile. While excellent, it is only applicable for three-axis motion.

As previously mentioned, the closed-form solution is mostly represented in parametric form. This requires surface approximations. Thus, many researchers had trend toward numerical solutions for the swept envelope. Their works can be categorized into two main approaches; vector representation approach [22]- [26] and cutter slice model approach [27], [28].

A numerical approximation of the swept envelope can be generated by calculating the intersection of the cutter with vectors emanating from or representing the workpiece designed surface. The vectors can be normal to the workpiece surface [29], unidirectional along the cutter axis [23]- [25] or a combination of both (also called hybrid) [22]. The accuracy of these methods is strongly proportional to the vectors resolution.

The cutter slice approach models the surface of the cutter as a set of circles [27], [28]. For each circle in the set, the normal to the plane containing the circle and the velocity vector are calculated. The grazing points (points on the swept envelope) are then generated from the cross product of these two vectors. The family of the grazing points for the set of circles represents the silhouette curve. The accuracy is directly proportional to the number of circles representing the cutter. At this moment it is worth to tell that the grinding-wheel swept volume can be found in the same manner of the cutting tools swept volumes as it also has a revolving shape and moving along a prescribed path.

2.2 End–Mill Cutting Tools Grinding

As a main type of cutting tools, solid carbide end-mills are very important to metal cutting, and there are always high demand for better end-mills in the manufacturing industry. The criteria for a solid carbide end-mill with high machinability on a type of metal are (1) the cutting force and the cutting edge temperature are comparatively low while the tool cutting the metal, (2) the integrity of the machined surface is good, and (3) the tool life is long. In practice, some end-mills are well designed [30]- [32], and a tool design includes all information about the functional features, e.g., 2 to 5 flutes, the primary and the secondary flanks along the side cutting edges, the bottom cutting edges with the rake faces and the flanks. The rake angle of the rake face influences the cutting force in machining, and the flute shape and size determine the tool rigidity and the chip evacuation ability. Thus, the flutes eventually affect the tools cutting performance and life. In order to accurately grind prescribed flutes, the side cutting edge should be derived first.

The side cutting edge equation is normally derived by considering a constant helical angle to the generatrix [33]- [40], a constant helical angle to the revolving axis [41]- [43], a constant pitch [44], [45] or, in some situations, a combination of two [46]. For example, a ball end-mill having a cutting edge with a constant helical angle to the cutting tool axis will not have a mathematical description for the cutting edge at the top of the ball. For the top of the ball, a constant helical angle to the generatrix or a constant pitch should be considered. At the common point of the two segments of the cutting edge, the continuity and the smoothness should be maintained.

A general mathematical model of the APT tool side cutting edge was introduced by Engin and Altintas [47]. With this model, many cutters used in industry such as cylindrical end-mills, ball end-mills, fillet end-mills, etc., have well-established mathematical representations for their side cutting edges. For other cutting tools that cannot be defined using the APT model such as parabolic cutting tools, a parametric form can be used to represent the revolving profile of the cutting tool [48] (eg. Hermite, Bezier or B-Spline representations) and the side cutting edge can be found numerically.

After deriving the mathematical equation of the side cutting edge, two main methods are normally adopted in end-mills grinding; the first method deals with determining the flute shape generated by a given grinding-wheel (direct method), and the second method focuses on designing a grinding-wheel profile that generates accurate end-mill flutes.

While the first method can be easily applied using the concept of the envelope theory, previous works focused on modeling the grinding-wheel and the cutting tool as two sets of finite thickness disks [49], [50], the problem is then simplified into calculating disk-disk intersections. The advantage of these works is that they built the basic foundation for grinding machining simulation; in particular, they were able to represent the geometry of the ground flutes, based on the selected standard grinding-wheel and its path during grinding. For example, Puig *et al.* [51] developed a 3D tool grinding simulation system. In this system, based on the CNC program (or codes) of grinding a tool, the grinding-wheel movements were represented with a number of Boolean operations; and the computer solid model of the tool is built by applying the Boolean operations on the discrete 2D cross-sections of the tool billet and rendering them in the three dimensions. Also, Kim and Ko [52] were able to construct the solid models of the ground end-mills in their computer simulation software system and retrieve from the models some tool geometric information that is difficult to physically measure in order to virtually inspect the tools.

The same grinding simulation methodology can be used to perform the inverse method grinding; that is to generate a wheel profile from a prescribed end-mill flute. For a given wheel location, this is carried out by repeatedly increasing the radius of each disk in the wheel until it contacts the desired helical surface profile [50]. Accuracy of the simulation can be controlled by varying the number of disks representing the grinding-wheel and the end-mill. However, no closed-form solution was obtained using these methods.

A part from the simulation methodology, obtaining a wheel profile from a prescribed flute profile has been investigated in many papers [33]- [45]. Assuming first that the grinding-wheel axis makes a particular angle with the cutting tool axis, and second that the distance between the tool coordinate system and the grinding-wheel coordinate system is known, then, the profile of the wheel can be generated according to the principle of reverse engineering of the envelope, which states that any contact point between the helical surface and the revolving surface must have its normal vector passing through the revolving axis. This method will yield a grinding-wheel with a free-form profile for the 2-axis flute grinding. For example, Tsai and Hsieh [33] generated a grinding-wheel profile to manufacture a ball end-mill cutting tool, Chen and Chen [37] generated a grinding-wheel profile for a fillet end-mill cutting tool with a concave-arc generatrix. Many other researchers employed the same principle of reverse engineering to generate the wheel profile; for example, Chen *et al.* [35] generated the wheel profile for a concave cone cutting tool. Chang and Chen [36] obtained the wheel profile for a cutting tool with a circular arc generatrix, and Chen *et al.* [42] developed the wheel profile for circular arc ball end-mill cutting tools. The main steps of their works are similar, including (1) determining the profile of the grinding-wheel for the 2-axis tool grinding and (2) calculating the tool rotation speed and the grinding-wheel feed rate.

The generated grinding-wheel profiles from the aforementioned works made the relative motions between the grinding-wheel and the cutting tool simple and decreased the simultaneous cooperative axes of the CNC tool grinding machine to 2 axes. However, as many researchers pointed out [42], [43]; there are residual surfaces on the tool and the side cutting edge strip is narrower near the tool tip. Thus post-processing is needed. Beside this, the free-form shapes of the grinding-wheels made them very difficult and expensive to make. Also, this current method cannot grind the rake faces with the specified normal rake angles. Moreover, the end-mill flute is exact only on one cross-section of the end-mill and the flute shape will be uncontrolled when moving to smaller end-mill cross-sections as the case in tapered end-mills grinding.

Different from the grinding methods mentioned above, Chen and Bin [53] and Feng and Bin [54] proposed a novel coordinate system on the side cutting edge and used a four-axis grinding machine with a standard grinding-wheel to grind the rake face of the end-mill. With a simple standard wheel, more relative motions were required to ensure constant normal rake angles along the side cutting edges. However, the proposed method is only applicable for special grinding-wheel shapes (torus and spherical) and no full flute grinding has been conducted.

Now, 5-axis CNC tool grinding machines are more popular, and it is required to machine the flute in one path, instead of multiple paths. To precisely machine the flutes of the tapered end-mills in 5-axis grinding, an optimal and practical approach to CNC programming is originally proposed [3]- [5] and will be introduced in the proceeding chapters.

2.3 Summary

In this chapter we closely reviewed current techniques related to our research topic, including geometric modeling of the swept volume and the end-mill tools grinding. The tools grinding research was described briefly in this chapter to cover most of the development in the field. Thus, next chapter will describe in detail one of the main tools grinding processes, that is; the two-axis tool grinding (inverse method, also known as indirect method), and will generate the grinding-wheel profile required to grind a prescribed tool flute by direct implementation of the method.

Chapter 3

Two–Axis Tool Grinding (Inverse Method)

3.1 Introduction

The principle of reverse engineering of the envelope will be described in detail in this chapter and will be employed in finding a grinding-wheel that grinds a prescribed tool flute shape along a two-axis path. Then, a grinding simulation will be carried out and the method drawbacks will be identified. But first, the geometric model of the end-mill cutting tool will be described.

3.2 Geometric Model of the End–Mills

End-mills mainly include several geometric features, such as several helical flutes and the corresponding side and bottom cutting edges, the first and the second flanks of each cutting edge, a gash (or a split) on the bottom, and the central core. As our work focus is the flutes grinding; two features are of our concern: the side cutting edge and the flute profile.

3.2.1 Side cutting edge

To design an end-mill, a Cartesian coordinate system $\Re^{\mathrm{T}} =: \left(\mathrm{o}^{\mathrm{T}}\mathbf{x}^{\mathrm{T}}\mathbf{y}^{\mathrm{T}}\mathbf{z}^{\mathrm{T}}\right)$ is established. Its origin o^{T} is located at a reference point on the tool axis. The reference point is normally selected on the end face in case of the flat end-mills or the fillet end-mills or the center of the ball in case of the ball end-mills, etc. The $\mathbf{z}^{\mathrm{T}}$-axis coincides with the tool axis and the $\mathbf{x}^{\mathrm{T}}$- axis is defined in relative with the starting point of the cutting edge. In this coordinate system, the side cutting edge of the end-mill is a helix on the cutting surface and is formulated with a parametric form.

First, the helical angle at any point on the side cutting edge can have one of two definitions: (1) the angle between the tangent vector of the cutting edge at that point and the tool axis or (2) the angle between the tangent vector and the generatrix. By adopting the second definition of the tool revolving surface $\mathbf{S}_{\mathrm{T}}$, where

$$\mathbf{S}_{\mathrm{T}}\left(z^{\mathrm{T}},\theta\right) = \left[\begin{array}{ccc} r_{\mathrm{T}}\left(z^{\mathrm{T}}\right)\cdot\cos\theta & r_{\mathrm{T}}\left(z^{\mathrm{T}}\right)\cdot\sin\theta & z^{\mathrm{T}} \end{array}\right]^{\mathrm{T}} \tag{3.1}$$

as shown in Fig. 3.1, the partial derivatives of the surface vector are calculated as

$$\frac{\partial\mathbf{S}_{\mathrm{T}}}{\partial z} = \left[\begin{array}{ccc} \frac{\partial r_{\mathrm{T}}\left(z^{\mathrm{T}}\right)}{\partial z^{\mathrm{T}}}\cdot\cos\theta & \frac{\partial r_{\mathrm{T}}\left(z^{\mathrm{T}}\right)}{\partial z^{\mathrm{T}}}\cdot\sin\theta & 1 \end{array}\right]^{\mathrm{T}} \tag{3.2}$$

and

$$\frac{\partial\mathbf{S}_{\mathrm{T}}}{\partial\theta} = \left[\begin{array}{ccc} -r_{\mathrm{T}}\left(z^{\mathrm{T}}\right)\cdot\sin\theta & r_{\mathrm{T}}\left(z^{\mathrm{T}}\right)\cdot\cos\theta & 0 \end{array}\right]^{\mathrm{T}} \tag{3.3}$$

In general, the tangent vector $d\mathbf{S}_{\mathrm{T}}$ of the helical curve and the tangent vector

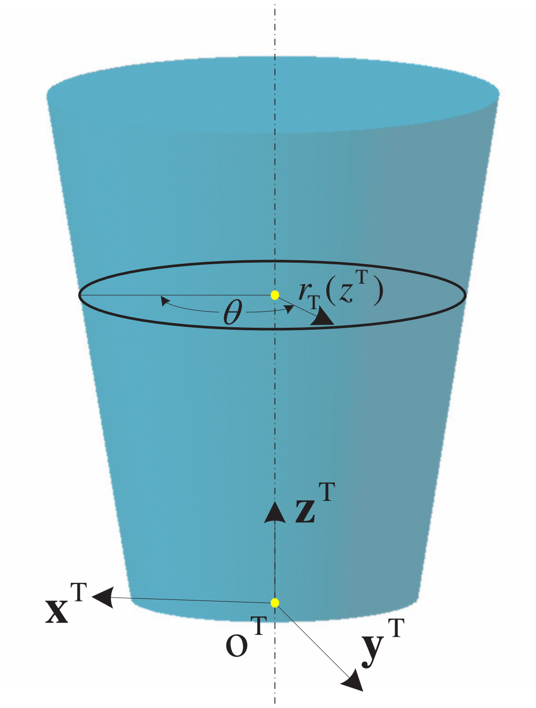

Figure 3.1: The cutting surface of an end-mill.

$\delta\mathbf{S}_\mathrm{T}$ of the generatrix can be estimated as

$$d\mathbf{S}_\mathrm{T} = \frac{\partial \mathbf{S}_\mathrm{T}}{\partial z^\mathrm{T}} \cdot dz^\mathrm{T} + \frac{\partial \mathbf{S}_\mathrm{T}}{\partial \theta} \cdot d\theta \tag{3.4}$$

and

$$\delta\mathbf{S}_\mathrm{T} = \frac{\partial \mathbf{S}_\mathrm{T}}{\partial z^\mathrm{T}} \cdot \delta z^\mathrm{T} \tag{3.5}$$

The helical angle ψ between the two vectors is obtained as

$$\cos^2\psi = \left(\frac{d\mathbf{S}_\mathrm{T} \cdot \delta\mathbf{S}_\mathrm{T}}{\|d\mathbf{S}_\mathrm{T}\| \cdot \|\delta\mathbf{S}_\mathrm{T}\|} \right)^2 \tag{3.6}$$

with more simplifications, we get

$$\left(dz^\mathrm{T}\right)^2 = \left(\left(\frac{\partial \mathbf{S}_\mathrm{T}}{\partial \theta} \right)^2 \Bigg/ \left(\frac{\partial \mathbf{S}_\mathrm{T}}{\partial z^\mathrm{T}} \right)^2 \right) \cdot \cot^2\psi \cdot d\theta^2 \tag{3.7}$$

Thus, the positive square root of the above equation is given as

$$dz^\mathrm{T} = \sqrt{\left(\frac{\partial \mathbf{S}_\mathrm{T}}{\partial \theta} \right)^2 \Bigg/ \left(\frac{\partial \mathbf{S}_\mathrm{T}}{\partial z^\mathrm{T}} \right)^2} \cdot \cot\psi \cdot d\theta \tag{3.8}$$

By first, integrating both sides of Eq.(3.8) and then, substituting the integration constant using the starting point of the side cutting edge, a relationship can be established between $z^{\mathrm{T}} = z_{\mathrm{C}}^{\mathrm{T}}$ and $\theta = \theta_{\mathrm{C}}$. Apply this relationship back into Eq.(3.1) to obtain the side cutting edge equation as

$$\mathbf{C}_{\mathrm{C}}^{\mathrm{T}} = \begin{bmatrix} x_{\mathrm{C}}^{\mathrm{T}} \\ y_{\mathrm{C}}^{\mathrm{T}} \\ z_{\mathrm{C}}^{\mathrm{T}} \\ 1 \end{bmatrix} = \begin{bmatrix} r_{\mathrm{T}}\left(z_{\mathrm{C}}^{\mathrm{T}}\right) \cdot \cos\theta_{\mathrm{C}} \\ r_{\mathrm{T}}\left(z_{\mathrm{C}}^{\mathrm{T}}\right) \cdot \sin\theta_{\mathrm{C}} \\ z_{\mathrm{C}}^{\mathrm{T}} \\ 1 \end{bmatrix} \tag{3.9}$$

3.2.2 Tool flute

Flutes are important geometric elements of the end-mills as they significantly affect the tools cutting performance. Specifically, the flutes of an end-mill are relevant to its core thickness, its rake angle, and the space for chips, so they determine the tools rigidity, cutting forces, and chip evacuation flow in machining. The flute surface is generated by sweeping the cross-sectional flute profile along the side cutting edge. Fig. 3.2 shows a general flute profile of a four-flute end-mill in the tool coordinate system $\Re^{\mathrm{T}}$ mentioned previously. In detail, the profile is normally considered on the tool major section between the circles of the maximum tool radius $r_{\mathrm{T}}^{\max}$ and the maximum core radius $r_{\mathrm{C}}^{\max}$ and consists of five segments. (1) Line segment $\mathrm{F}_0\mathrm{F}_1$ forms the rake face with radial rake angle α_{R} , which is the angle between $\mathrm{F}_0\mathrm{F}_1$ and $\mathbf{x}^{\mathrm{T}}$-axis; (2) circular arc $\mathrm{F}_1\mathrm{F}_2$ of radius r_1 is tangent to both $\mathrm{F}_0\mathrm{F}_1$ and the core circle of radius $r_{\mathrm{C}}^{\max}$;

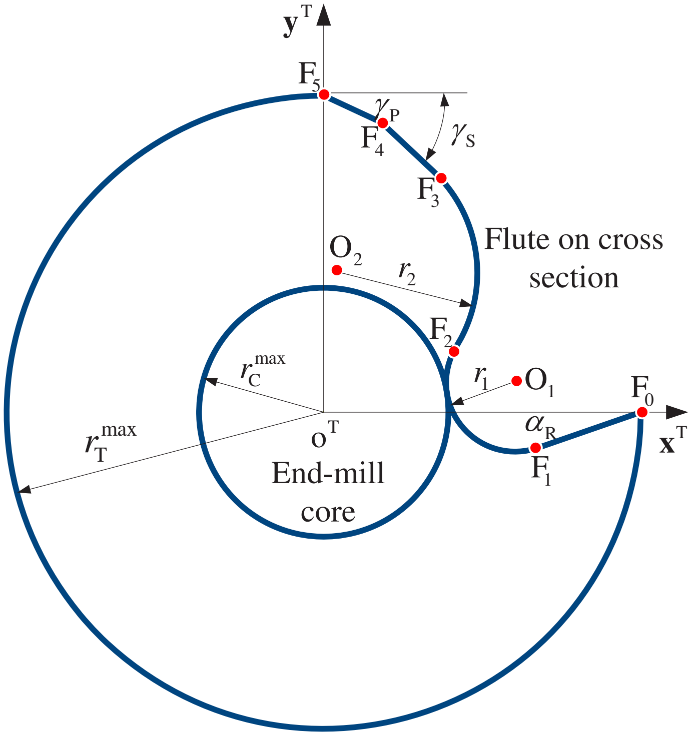

Figure 3.2: A general flute design of a four flute end-mill on the tool coordinate system.

(3) circular arc F_2F_3 of radius r_2 is tangent to F_1F_2, and the two circular arcs form the flute surface; (4) line segment F_3F_4, tangent to F_2F_3, generates the secondary relief surface with relief angle γ_S; and (5) line segment F_4F_5 generates the primary relief surface with relief angle γ_P. Taking a four-flute end-mill as an example does not lose the generality, the flute parametric representation is derived and provided in the following.

The length of the flute profile is adopted as parameter l starting from point

F_0 where $l = 0$. The parametric equation of segment F_0F_1 is

$$\mathbf{F}(l) = \begin{bmatrix} r_{\mathrm{T}}^{\max} \\ 0 \end{bmatrix} - l \cdot \begin{bmatrix} \cos\alpha_{\mathrm{R}} \\ \sin\alpha_{\mathrm{R}} \end{bmatrix} \text{ where } \; l \in [0, l_{\mathrm{F}_1}] \tag{3.10}$$

In same manner, the parametric equation of F_1F_2 is described as

$$\mathbf{F}(l) = \mathrm{O}_1 + \begin{bmatrix} r_1 \sin\left(\alpha_{\mathrm{R}} - \frac{l - l_{\mathrm{F}_1}}{r_1}\right) \\ -r_1 \cos\left(\alpha_{\mathrm{R}} - \frac{l - l_{\mathrm{F}_1}}{r_1}\right) \end{bmatrix} \text{ where } \; l \in [l_{\mathrm{F}_1}, l_{\mathrm{F}_2}] \tag{3.11}$$

and for F_2F_3 the equation is

$$\mathbf{F}(l) = \mathrm{O}_2 + \begin{bmatrix} -r_2 \sin\left(\alpha_{\mathrm{R}} - \frac{l_{\mathrm{F}_2} - l_{\mathrm{F}_1}}{r_1} + \frac{l - l_{\mathrm{F}_2}}{r_2}\right) \\ r_2 \cos\left(\alpha_{\mathrm{R}} - \frac{l_{\mathrm{F}_2} - l_{\mathrm{F}_1}}{r_1} + \frac{l - l_{\mathrm{F}_2}}{r_2}\right) \end{bmatrix} \text{ where } \; l \in [l_{\mathrm{F}_2}, l_{\mathrm{F}_3}] \tag{3.12}$$

For a given length of segment F_4F_5, $l_{\mathrm{F}_4\mathrm{F}_5}$, the parametric equation of F_3F_4 can be represented as

$$\mathbf{F}(l) = \begin{bmatrix} l_{\mathrm{F}_4\mathrm{F}_5} \cos\gamma_{\mathrm{P}} \\ r_{\mathrm{T}} - l_{\mathrm{F}_4\mathrm{F}_5} \sin\gamma_{\mathrm{P}} \end{bmatrix} + (l_{\mathrm{F}_4} - l) \,.\, \begin{bmatrix} \cos\gamma_{\mathrm{S}} \\ -\sin\gamma_{\mathrm{S}} \end{bmatrix} \text{ where } \; l \in [l_{\mathrm{F}_3}, l_{\mathrm{F}_4}] \tag{3.13}$$

Now the parametric equation of the last segment, F_4F_5 , can be expressed as

$$\mathbf{F}(l) = \begin{bmatrix} 0 \\ r_{\mathrm{T}}^{\max} \end{bmatrix} + (l_{\mathrm{F}_5} - l) \,.\, \begin{bmatrix} \cos\gamma_{\mathrm{P}} \\ -\sin\gamma_{\mathrm{P}} \end{bmatrix} \text{ where } \; l \in [l_{\mathrm{F}_4}, l_{\mathrm{F}_5}] \tag{3.14}$$

In the previous equations, l_{F_i} is the length of the flute profile at point F_i, where $i \in \{0, 1, ..., 5\}$, and can be obtained together with the two arcs centers O_1 and O_2 using the geometric relations.

3.3 Grinding–Wheel Profile Shape

Starting from the parametric equation derived in the previous section for the tool flute, the flute surface generated from sweeping $\mathbf{F}(l)$ along the side cutting edge can be easily obtained. In general, the flute surface is represented as

$$\mathbf{S}_{\mathrm{F}}^{\mathrm{T}}(l, \theta_{\mathrm{C}}) = \begin{bmatrix} x_{\mathrm{F}}^{\mathrm{T}} \\ y_{\mathrm{F}}^{\mathrm{T}} \\ z_{\mathrm{F}}^{\mathrm{T}} \end{bmatrix} = \begin{bmatrix} \cos\theta_{\mathrm{C}} & -\sin\theta_{\mathrm{C}} & 0 \\ \sin\theta_{\mathrm{C}} & \cos\theta_{\mathrm{C}} & 0 \\ 0 & 0 & z_{\mathrm{C}}^{\mathrm{T}}(\theta_{\mathrm{C}}) \end{bmatrix} \mathbf{F}(l) \tag{3.15}$$

here, for cylindrical surfaces, we have

$$z_{\mathrm{C}}^{\mathrm{T}} = \frac{r_{\mathrm{T}}^{\max}\theta_{\mathrm{C}}}{\tan\psi} \tag{3.16}$$

By establishing the grinding-wheel coordinate system $\Re^{\mathrm{G}}$, where $\mathbf{x}^{\mathrm{G}}$-axis lies on the $\mathbf{x}^{\mathrm{T}}\mathbf{y}^{\mathrm{T}}$ plane at an angle 45^{o} (the superscript "o" stands for degree) from $\mathbf{x}^{\mathrm{T}}$-axis, and $\mathbf{z}^{\mathrm{G}}$-axis as the grinding-wheel axis. Here, $\mathrm{o}^{\mathrm{G}}\mathbf{z}^{\mathrm{G}}$ line and $\mathrm{o}^{\mathrm{T}}\mathbf{z}^{\mathrm{T}}$ line are skew lines that lie on two different planes with a common normal line $\mathrm{o}^{\mathrm{T}}\mathrm{o}^{\mathrm{G}}$ of length a. $\mathbf{z}^{\mathrm{G}}$-axis can now be found by rotating $\mathbf{z}^{\mathrm{T}}$-axis about $\mathbf{x}^{\mathrm{G}}$-axis with angle $90^{\mathrm{o}} - \psi$. $\mathbf{y}^{\mathrm{G}}$-axis is now found from the right hand rule (Fig. 3.3). The equation of the line $\mathrm{o}^{\mathrm{G}}\mathbf{z}^{\mathrm{G}}$ can now be expressed in the tool coordinate system $\Re^{\mathrm{T}}$ as

$$\mathbf{r}_{z^{\mathrm{G}}}^{\mathrm{T}} = \begin{bmatrix} \frac{\sqrt{2}}{2}a \\ \frac{\sqrt{2}}{2}a \\ 0 \end{bmatrix} + \lambda_1 \begin{bmatrix} \frac{\sqrt{2}}{2}\cos\psi \\ -\frac{\sqrt{2}}{2}\cos\psi \\ \sin\psi \end{bmatrix} \tag{3.17}$$

where λ_1 is the length parameter. Since the grinding-wheel has a revolving surface, the normal vector of any point on that surface must pass through the grinding-wheel axis $\mathbf{z}^{\mathrm{G}}$. Then

$$\mathbf{r}_{z^{\mathrm{G}}}^{\mathrm{T}} = \mathbf{S}_{\mathrm{F}}^{\mathrm{T}}(l, \theta_{\mathrm{C}}) + \lambda_2\mathbf{N}_{\mathrm{F}} \tag{3.18}$$

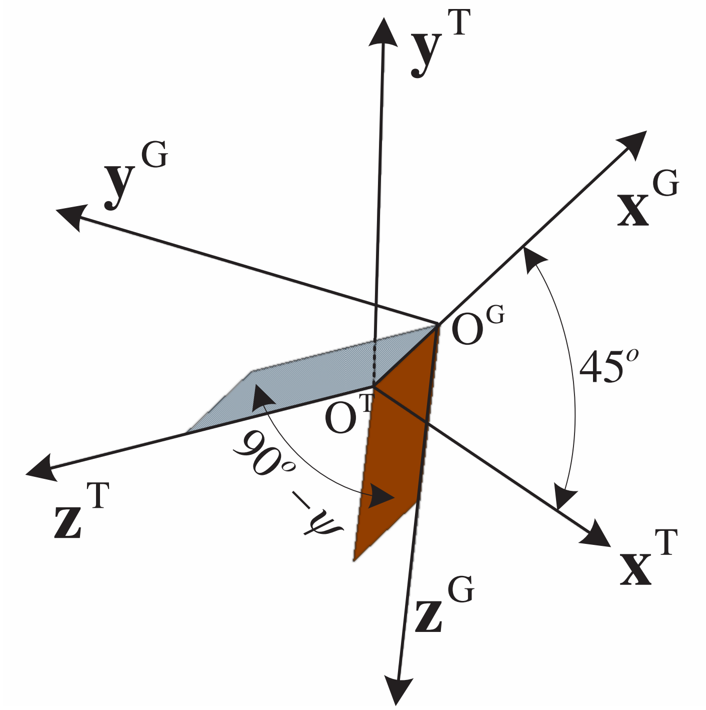

Figure 3.3: Tool and grinding-wheel coordinate systems relationship.

where

$$\mathbf{N}_{\mathrm{F}} = \left[\begin{array}{ccc} \mathbf{N}_{\mathrm{F},x^{\mathrm{T}}} & \mathbf{N}_{\mathrm{F},y^{\mathrm{T}}} & \mathbf{N}_{\mathrm{F},z^{\mathrm{T}}} \end{array}\right]^{\mathrm{T}} = \frac{\partial \mathbf{S}_{\mathrm{F}}^{\mathrm{T}}}{\partial l} \times \frac{\partial \mathbf{S}_{\mathrm{F}}^{\mathrm{T}}}{\partial \theta_{\mathrm{C}}} \tag{3.19}$$

By eliminating λ_1 and λ_2, the equation can now be expressed as

$$\begin{gathered} a\left(\sqrt{2}\mathbf{N}_{\mathrm{F},z^{\mathrm{T}}} + \mathbf{N}_{\mathrm{F},y^{\mathrm{T}}}\tan\psi - \mathbf{N}_{\mathrm{F},x^{\mathrm{T}}}\tan\psi\right) + z_{\mathrm{F}}^{\mathrm{T}}\cdot\left(\mathbf{N}_{\mathrm{F},x^{\mathrm{T}}} + \mathbf{N}_{\mathrm{F},y^{\mathrm{T}}}\right) \\ -\mathbf{N}_{\mathrm{F},z^{\mathrm{T}}}\cdot\left(x_{\mathrm{F}}^{\mathrm{T}} + y_{\mathrm{F}}^{\mathrm{T}}\right) + \sqrt{2}\tan\psi\cdot\left(y_{\mathrm{F}}^{\mathrm{T}}\cdot\mathbf{N}_{\mathrm{F},x^{\mathrm{T}}} - x_{\mathrm{F}}^{\mathrm{T}}\cdot\mathbf{N}_{\mathrm{F},y^{\mathrm{T}}}\right) = 0 \end{gathered} \tag{3.20}$$

Now, by using the property of the helical surface

$$y_{\mathrm{F}}^{\mathrm{T}}\mathbf{N}_{\mathrm{F},x^{\mathrm{T}}} - x_{\mathrm{F}}^{\mathrm{T}}\mathbf{N}_{\mathrm{F},y^{\mathrm{T}}} = \frac{r_{\mathrm{T}}^{\max}}{\tan\psi}\mathbf{N}_{\mathrm{F},z^{\mathrm{T}}} \tag{3.21}$$

Eq.(3.20) can be expressed as

$$\begin{gathered} a\left(\sqrt{2}\mathbf{N}_{\mathrm{F},z^{\mathrm{T}}} + \mathbf{N}_{\mathrm{F},y^{\mathrm{T}}}\tan\psi - \mathbf{N}_{\mathrm{F},x^{\mathrm{T}}}\tan\psi\right) + z_{\mathrm{F}}^{\mathrm{T}}\cdot\left(\mathbf{N}_{\mathrm{F},x^{\mathrm{T}}} + \mathbf{N}_{\mathrm{F},y^{\mathrm{T}}}\right) \\ -\mathbf{N}_{\mathrm{F},z^{\mathrm{T}}}\cdot\left(x_{\mathrm{F}}^{\mathrm{T}} + y_{\mathrm{F}}^{\mathrm{T}}\right) + \sqrt{2}r_{\mathrm{T}}^{\max}\mathbf{N}_{\mathrm{F},z^{\mathrm{T}}} = 0 \end{gathered} \tag{3.22}$$

solving Eq.(3.15) and Eq.(3.22) simultaneously for l and θ_{C}, the contact curve between the tool and the grinding-wheel (effective grinding edge EGE) can be obtained as

$$\mathbf{C}_{\mathrm{F}}^{\mathrm{T}} = \begin{bmatrix} x_{\mathrm{F}}^{\mathrm{T}} \\ y_{\mathrm{F}}^{\mathrm{T}} \\ z_{\mathrm{F}}^{\mathrm{T}} \\ 1 \end{bmatrix} \tag{3.23}$$

Then, the grinding-wheel surface $\mathbf{S}_{\mathrm{W}}^{\mathrm{G}}$ can be obtained by first transforming the contact curve $\mathbf{C}_{\mathrm{F}}^{\mathrm{T}}$ to the grinding-wheel coordinate system $\Re^{\mathrm{G}}$ to get $\mathbf{C}_{\mathrm{F}}^{\mathrm{G}}$, then rotating a full rotation about $\mathbf{z}^{\mathrm{G}}$-axis. Mathematically, this can be represented as

$$\mathbf{C}_{\mathrm{F}}^{\mathrm{G}} = \mathrm{ROT}(\psi - 90^o, x) \cdot \mathrm{T}(-a, 0, 0) \cdot \mathrm{ROT}(-45^o, z) \cdot \mathbf{C}_{\mathrm{F}}^{\mathrm{T}} \tag{3.24a}$$

$$\mathbf{S}_{\mathrm{W}}^{\mathrm{G}} = \begin{bmatrix} x_{\mathrm{W}}^{\mathrm{G}} \\ y_{\mathrm{W}}^{\mathrm{G}} \\ z_{\mathrm{W}}^{\mathrm{G}} \\ 1 \end{bmatrix} = \begin{bmatrix} \cos\theta & -\sin\theta & 0 & 0 \\ \sin\theta & \cos\theta & 0 & 0 \\ 0 & 0 & 1 & 0 \\ 0 & 0 & 0 & 1 \end{bmatrix} \mathbf{C}_{\mathrm{F}}^{\mathrm{G}} \tag{3.24b}$$

where

$$\mathrm{ROT}(\theta, x) = \begin{bmatrix} 1 & 0 & 0 & 0 \\ 0 & \cos\theta & -\sin\theta & 0 \\ 0 & \sin\theta & \cos\theta & 0 \\ 0 & 0 & 0 & 1 \end{bmatrix} \tag{3.25a}$$

$$\mathrm{T}(a,b,c) = \begin{bmatrix} 1 & 0 & 0 & a \\ 0 & 1 & 0 & b \\ 0 & 0 & 1 & c \\ 0 & 0 & 0 & 1 \end{bmatrix} \tag{3.25b}$$

$$\mathrm{ROT}(\theta,z) = \begin{bmatrix} \cos\theta & -\sin\theta & 0 & 0 \\ \sin\theta & \cos\theta & 0 & 0 \\ 0 & 0 & 1 & 0 \\ 0 & 0 & 0 & 1 \end{bmatrix} \tag{3.25c}$$

The grinding-wheel cross-section can now be calculated by intersecting surface $\mathbf{S}_{\mathrm{W}}^{\mathrm{G}}$ with $\mathbf{x}^{\mathrm{G}}\mathbf{z}^{\mathrm{G}}$ plane. Thus, the wheel profile can be represented as

$$\mathbf{C}_{\mathrm{W}}^{\mathrm{G}} = \begin{bmatrix} R_{\mathrm{W}} \\ 0 \\ z_{\mathrm{W}}^{\mathrm{G}} \end{bmatrix} \tag{3.26}$$

where

$$R_{\mathrm{W}} = \sqrt{(x_{\mathrm{W}}^{\mathrm{G}})^2 + (y_{\mathrm{W}}^{\mathrm{G}})^2} \tag{3.27}$$

3.4 Grinding Process Parameters

After deriving the grinding-wheel profile, only two parameters are required to completly describe the grinding process, these are:

1. The axial feed rate V_z, and can be estimated as

$$V_z = \frac{\partial z_{\mathrm{C}}^{\mathrm{T}}}{\partial t} = \frac{\partial z_{\mathrm{C}}^{\mathrm{T}}}{\partial \theta_{\mathrm{C}}} \cdot \frac{\partial \theta_{\mathrm{C}}}{\partial t} = \omega \frac{\partial z_{\mathrm{C}}^{\mathrm{T}}}{\partial \theta_{\mathrm{C}}} \tag{3.28}$$

   where ω is the angular velocity of the tool about its axis.

2. The radial feed rate V_{r}, and can be derived from the radial displacement d_s. If the radial displacement is determined by the variation of the outer radius of the cutting tool only; then over-cut will occur. Thus, the radial displacement will be determined as (Fig. 3.4)

$$d_s = r_{\mathrm{C}}^{\max} - \frac{r_{\mathrm{C}}^{\max}}{r_{\mathrm{T}}^{\max}} \cdot r_{\mathrm{T}}(z_{\mathrm{C}}^{\mathrm{T}}) \tag{3.29}$$

   Hence, the radial feed rate V_{r} can now be found as

$$V_{\mathrm{r}} = \frac{d}{dt}(d_s) = \omega \frac{d}{dz_{\mathrm{C}}^{\mathrm{T}}} \left(r_{\mathrm{C}}^{\max} - \frac{r_{\mathrm{C}}^{\max}}{r_{\mathrm{T}}^{\max}} \cdot r_{\mathrm{T}}(z_{\mathrm{C}}^{\mathrm{T}}) \right) \cdot \frac{dz_{\mathrm{C}}^{\mathrm{T}}}{d\theta_{\mathrm{C}}} \tag{3.30}$$

3.5 Grinding Simulation

The inverse method grinding simulation is conducted for two different end-mills; a cylindrical ball end-mill and a tapered flat end-mill. The free-form profiles of the grinding-wheels required to grind those end-mills are generated. Then, the radial and the axial feeds are calculated. Finally, a discussion about the final shapes of the end-mills will highlight the major drawbacks of the current method.

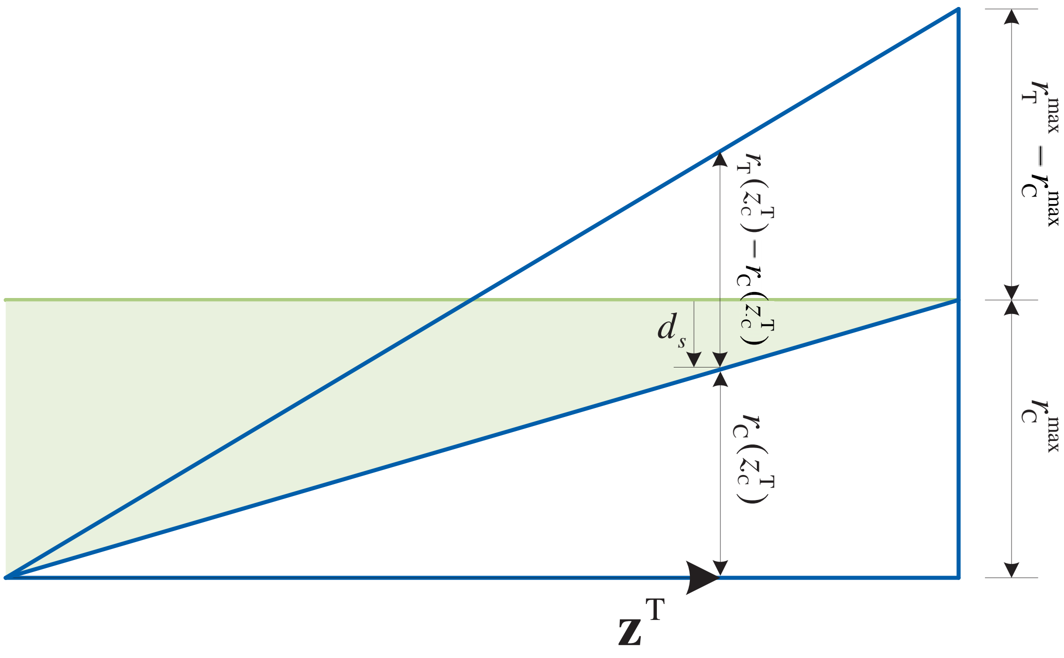

Figure 3.4: The radial displacement of the grinding-wheel along the tool axis.

3.5.1 Cylindrical ball end–mill

A 15mm cylindrical ball end-mill with length $L = 40$mm and a cylinder cross-section as shown in Fig. 3.5 and a helical angle of 60^o is ground using the inverse method described, the grinding-wheel axis is initially located at a distance $a = 1.5 \times r_T^{max} = 22.5$mm from the tool axis. The grinding-wheel profile is shown in Fig. 3.6. As can be depicted from the figure, the profile is consisting of 5 free-form segments with only C^0 continuity between the primary and the secondary relief surfaces; making the production of such wheels impractical.

In order to find the axial and the radial feeds, the side cutting edge of the

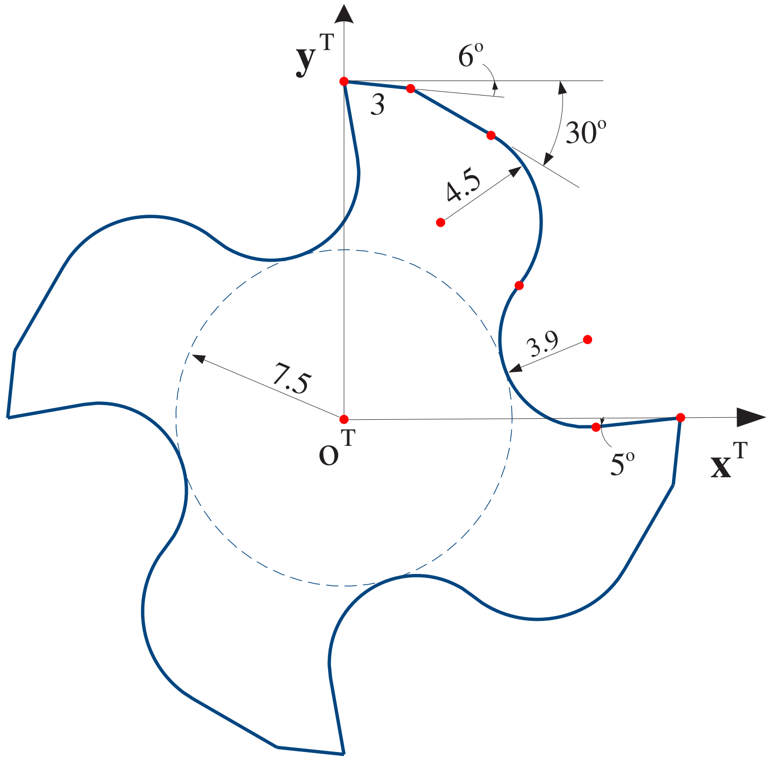

Figure 3.5: Cylindrical ball end-mill cross-section in mm.

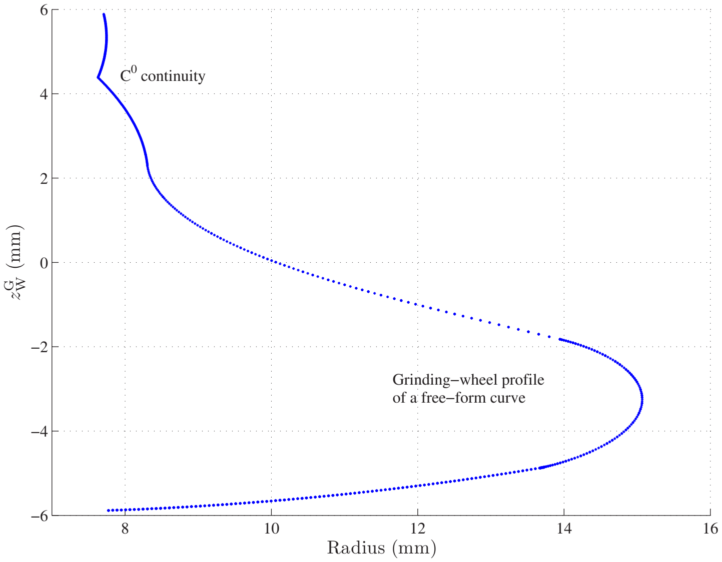

Figure 3.6: The grinding-wheel revolving profile in mm.

end-mill is derived first. It can be expressed as

$$\mathbf{C}_{\mathrm{C}}^{\mathrm{T}} = \begin{bmatrix} r_{\mathrm{T}}^{\max} \cdot \cos\theta_{\mathrm{C}} \\ r_{\mathrm{T}}^{\max} \cdot \sin\theta_{\mathrm{C}} \\ z_{\mathrm{C}}^{\mathrm{T}} \\ 1 \end{bmatrix} \qquad 0 \le z_{\mathrm{C}}^{\mathrm{T}} \le L \tag{3.31a}$$

$$\mathbf{C}_{\mathrm{C}}^{\mathrm{T}} = \begin{bmatrix} \sqrt{(r_{\mathrm{T}}^{\max})^2 - (z_{\mathrm{C}}^{\mathrm{T}})^2}\cos\theta_{\mathrm{C}} \\ \sqrt{(r_{\mathrm{T}}^{\max})^2 - (z_{\mathrm{C}}^{\mathrm{T}})^2}\sin\theta_{\mathrm{C}} \\ z_{\mathrm{C}}^{\mathrm{T}} \\ 1 \end{bmatrix} \qquad -r_{\mathrm{T}}^{\max} \le z_{\mathrm{C}}^{\mathrm{T}} \le 0 \tag{3.31b}$$

where

$$\theta_{\mathrm{C}} = \begin{cases} \frac{z_{\mathrm{C}}^{\mathrm{T}} \cdot \tan\psi}{r_{\mathrm{T}}^{\max}} & 0 \le z_{\mathrm{C}}^{\mathrm{T}} \le L \\ \frac{1}{2}\tan\psi \cdot \left[\ln\left(\frac{r_{\mathrm{T}}^{\max} - z_{\mathrm{C}}^{\mathrm{T}}}{r_{\mathrm{T}}^{\max} + z_{\mathrm{C}}^{\mathrm{T}}}\right)\right] & -r_{\mathrm{T}}^{\max} \le z_{\mathrm{C}}^{\mathrm{T}} \le 0 \end{cases} \tag{3.32}$$

Now, the axial feed rate V_z can be expressed as

$$V_z = \begin{cases} \frac{r_{\mathrm{T}}^{\max}}{\tan\psi}\omega & 0 \le z_{\mathrm{C}}^{\mathrm{T}} \le L \\ \frac{(r_{\mathrm{T}}^{\max})^2 - (z_{\mathrm{C}}^{\mathrm{T}})^2}{r_{\mathrm{T}}^{\max} \cdot \tan\psi}\omega & -r_{\mathrm{T}}^{\max} \le z_{\mathrm{C}}^{\mathrm{T}} \le 0 \end{cases} \tag{3.33}$$

In order to find the radial feed, first we find the radial displacement as

$$d_{\mathrm{s}} = \begin{cases} 0 & 0 \le z_{\mathrm{C}}^{\mathrm{T}} \le L \\ r_{\mathrm{C}}^{\max} - \frac{r_{\mathrm{C}}^{\max}}{r_{\mathrm{T}}^{\max}} \cdot \sqrt{(r_{\mathrm{T}}^{\max})^2 - (z_{\mathrm{C}}^{\mathrm{T}})^2} & -r_{\mathrm{T}}^{\max} \le z_{\mathrm{C}}^{\mathrm{T}} \le 0 \end{cases} \tag{3.34}$$

Hence, the radial feed rate V_{r} can now be found from Eq.(3.30) as

$$V_{\mathrm{r}} = \begin{cases} 0 & 0 \le z_{\mathrm{C}}^{\mathrm{T}} \le L \\ \frac{r_{\mathrm{C}}^{\max}}{r_{\mathrm{T}}^{\max}} \cdot \frac{\sqrt{(r_{\mathrm{T}}^{\max})^2 - (z_{\mathrm{C}}^{\mathrm{T}})^2}}{r_{\mathrm{T}}^{\max} \cdot \tan\psi} \cdot z_{\mathrm{C}}^{\mathrm{T}} \cdot \omega & -r_{\mathrm{T}}^{\max} \le z_{\mathrm{C}}^{\mathrm{T}} \le 0 \end{cases} \tag{3.35}$$

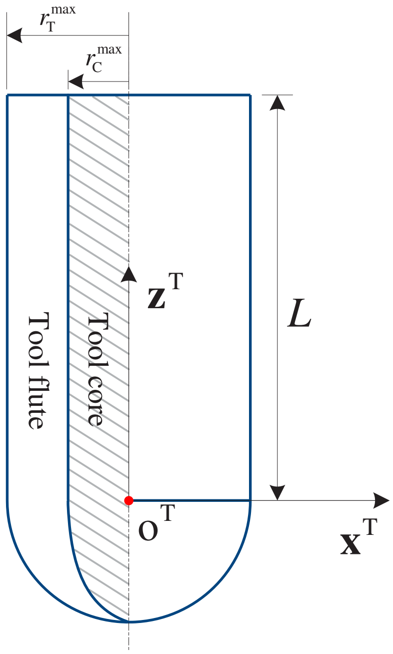

Figure 3.7: Effect of the radial displacement on the cylindrical ball end-mill core shape.

Thus, due to the radial displacement, the core of the end-mill will look as shown in Fig. 3.7. The ground end-mill is now shown in Fig. 3.8. It shows the error in the generated side cutting edge by comparing with the designed one.

3.5.2 Tapered flat end-mill

A tapered flat end-mill having a major radius $r_{\mathrm{T}}^{\max} = 15$mm, a tool length $L = 40$mm, a tapered angle $\varphi_{\mathrm{T}} = 10^{\mathrm{o}}$, a helical angle $\psi = 20^{\mathrm{o}}$ and dimensions at the major cross-section as shown in Fig. 3.9 is also ground using the inverse method. The grinding-wheel axis is initially located at a distance $a = 3 \times r_{\mathrm{T}}^{\max} = 45$mm from the tool axis. The profile of the grinding-wheel is consisting of 5 free-form segments as

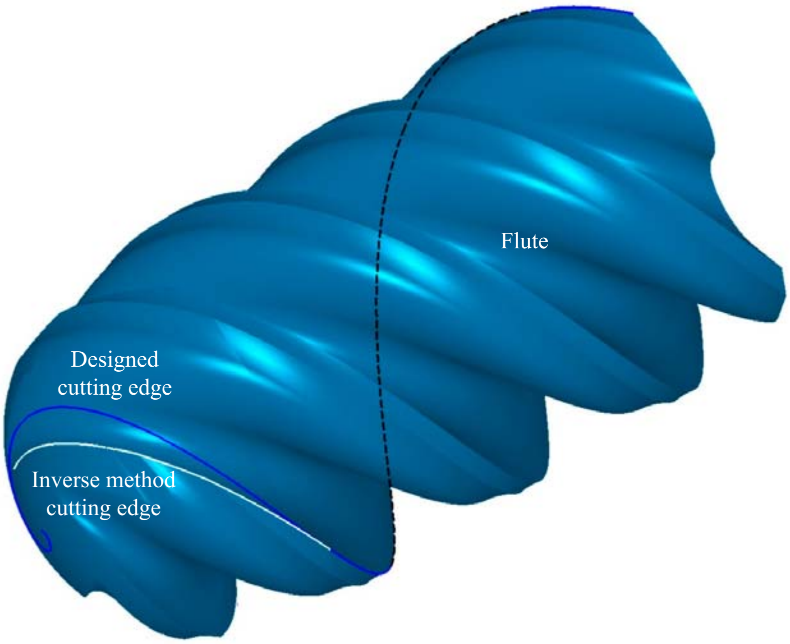

Figure 3.8: Ground ball end-mill using the inverse method simulation.

shown in Fig. 3.10. In order to find the axial and the radial feeds, the cutting edge of the end-mill is derived first. This gives the expression

$$\mathbf{C}_{\mathrm{C}}^{\mathrm{T}} = \begin{bmatrix} \left(r_{\mathrm{T}}^{\max} - \tan\varphi_{\mathrm{T}}(L - z_{\mathrm{C}}^{\mathrm{T}})\right)\cos\theta_{\mathrm{C}} \\ \left(r_{\mathrm{T}}^{\max} - \tan\varphi_{\mathrm{T}}(L - z_{\mathrm{C}}^{\mathrm{T}})\right)\sin\theta_{\mathrm{C}} \\ z_{\mathrm{C}}^{\mathrm{T}} \\ 1 \end{bmatrix} \tag{3.36}$$

where

$$\theta_{\mathrm{C}} = \frac{\tan\psi}{\sin\varphi_{\mathrm{T}}}\left[\ln\left(\frac{r_{\mathrm{T}}^{\max} - L\tan\varphi_{\mathrm{T}}}{\tan\varphi_{\mathrm{T}}} + z_{\mathrm{C}}^{\mathrm{T}}\right) - \ln\left(\frac{r_{\mathrm{T}}^{\max} - L\tan\varphi_{\mathrm{T}}}{\tan\varphi_{\mathrm{T}}}\right)\right] \tag{3.37}$$

Now, the axial feed rate V_z can be expressed as

$$V_z = \frac{r_{\mathrm{T}}^{\max}\cdot\cos\varphi_{\mathrm{T}} - (L - z_{\mathrm{C}}^{\mathrm{T}})\sin\varphi_{\mathrm{T}}}{\tan\psi}\omega \tag{3.38}$$

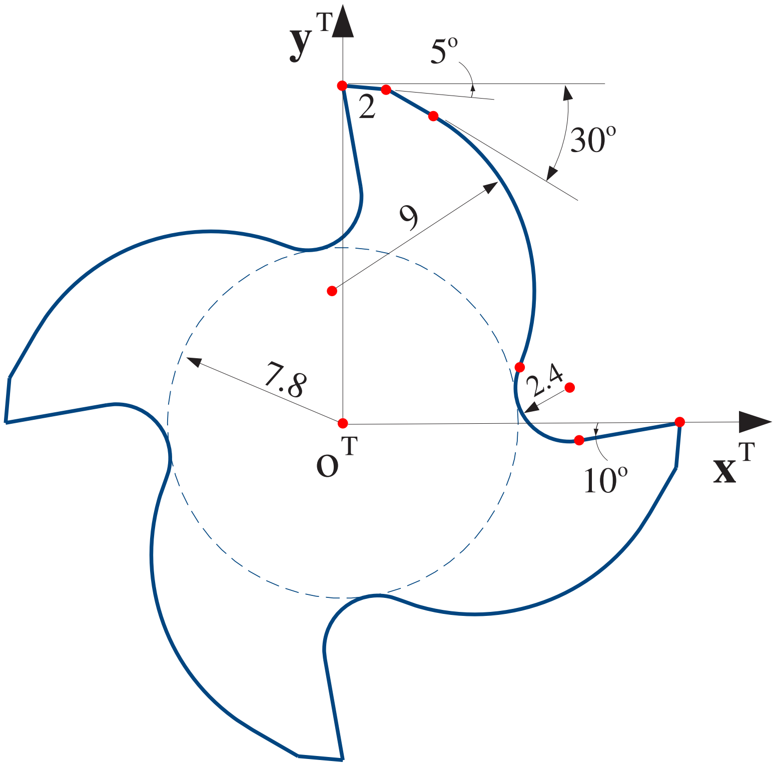

Figure 3.9: Tapered flat end-mill cross-section in mm.

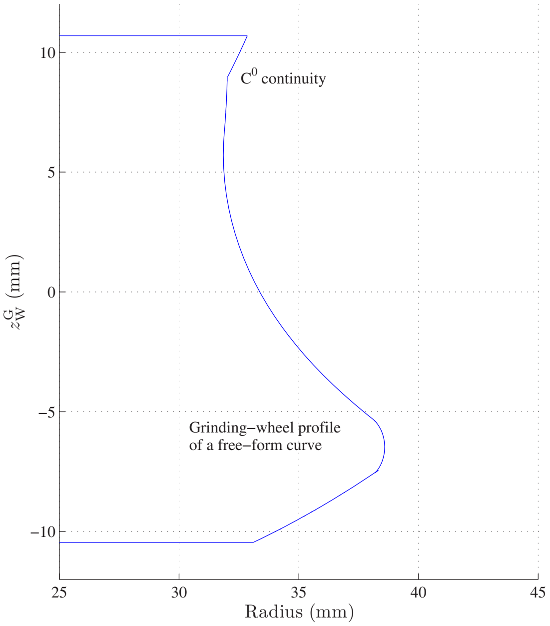

Figure 3.10: The grinding-wheel revolving profile in mm.

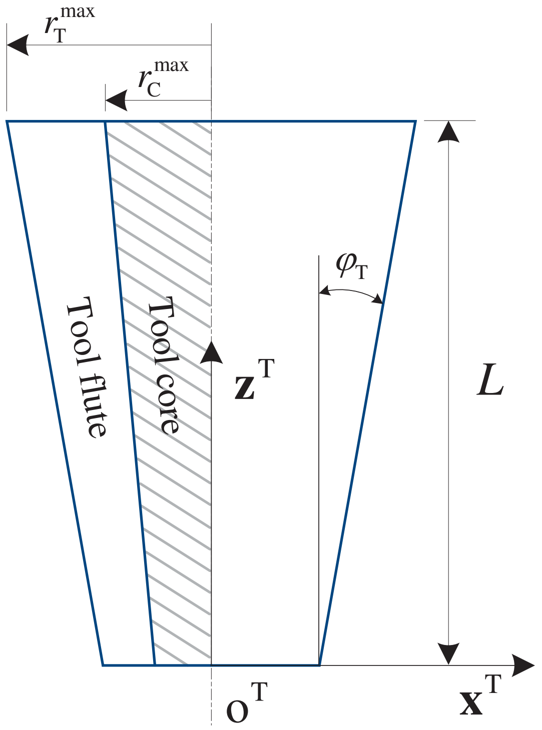

Figure 3.11: Effect of the radial displacement on the tapered flat end-mill core shape.

In order to find the radial feed, first we find the radial displacement as

$$d_{\mathrm{s}} = r_{\mathrm{C}}^{\max} - \frac{r_{\mathrm{C}}^{\max}}{r_{\mathrm{T}}^{\max}} \cdot \left(r_{\mathrm{T}}^{\max} - (L - z_{\mathrm{C}}^{\mathrm{T}}) \tan\varphi_{\mathrm{T}}\right) \tag{3.39}$$

Hence, the radial feed rate V_{r} can now be found from Eq.(3.30) as

$$V_{\mathrm{r}} = r_{\mathrm{C}}^{\max} \cdot \frac{\sin\varphi_{\mathrm{T}} - (L - z_{\mathrm{C}}^{\mathrm{T}}) \sin\varphi_{\mathrm{T}} \tan\varphi_{\mathrm{T}}}{\tan\psi} \omega \tag{3.40}$$

Thus, due to the radial displacement, the core of the end-mill will look as shown in Fig. 3.11. And then, the end-mill will look as shown in Fig. 3.12.

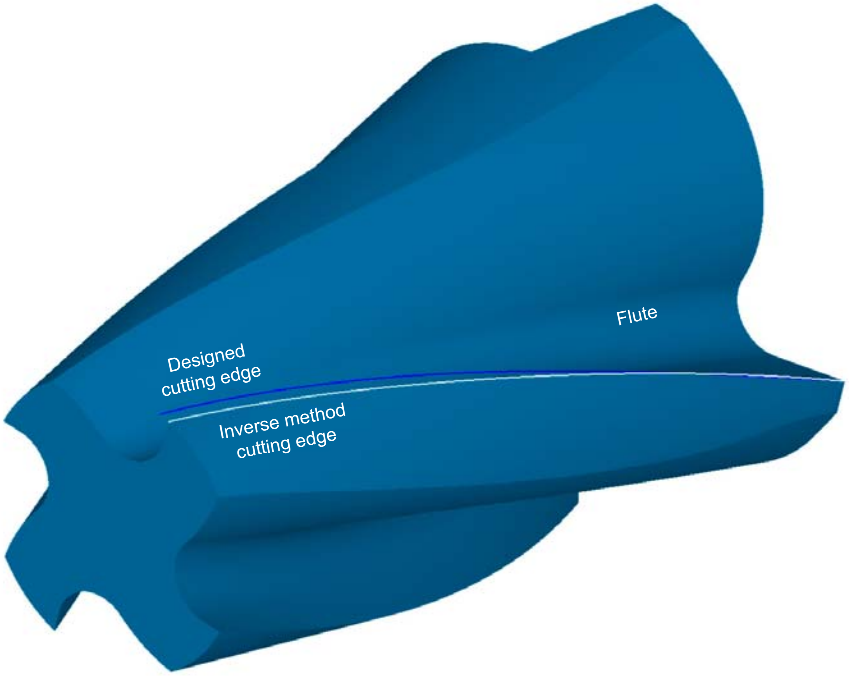

Figure 3.12: Ground tapered flat end-mill using the inverse method simulation.

3.6 The Advantages and the Disadvantages of the Inverse Method

The inverse method grinding is considered as a simple process that grinds the end-mill flutes with simple relative motions between the grinding-wheel and the cutting tool. This approach includes three steps; First, the inverse method is adopted to calculate the grinding-wheel profile, which is represented with a free-form curve; second, the grinding-wheel is made according to the profile; and then the 2-axis CNC grinding operation is applied to machine the flutes. Generally, these flutes are accurate; hence, this approach is applicable. Unfortunately, there are two major drawbacks of this approach. The first drawback is that the special grinding-wheel is difficult to make and dress due to its free-form profile, and the second one is that this approach cannot be used for machining accurate flutes of tapered end-mills. Regarding any flute of a tapered end-mill, its side cutting edge is a helix on the conical end-mill envelope, and the flutes cross-section curve varies along the tool axis. Neither is the flute geometry modeled by sweeping a flute cross-sectional curve along the side cutting edge from one end to the other, nor can it be machined with the 2-axis CNC grinding. A simple example is rendered in the following to explain the problem of the current approach to machining the flutes of the tapered end-mills.

In industry, the conventional 2-axis tool grinding machines are still used to machine end-mills, and a machine of this kind is illustrated in Fig. 3.13. The machine kinematics is that the grinding-wheel can move up and down along the $\mathbf{Y}^{\mathrm{M}}$-axis and rotate about this axis by angle $\mathbf{B}^{\mathrm{M}}$, and the end-mill can move along the $\mathbf{X}^{\mathrm{M}}$-axis and rotate about its axis. Usually, the rotation of $\mathbf{B}^{\mathrm{M}}$ cannot be simultaneously executed with the motions of $\mathbf{X}^{\mathrm{M}}$ and $\mathbf{Y}^{\mathrm{M}}$, so this machine is a 2-axis CNC grinder. This type of machine is often used to grind the flutes of cylindrical end-mills. In machining, the $\mathbf{B}^{\mathrm{M}}$ is set and fixed at the helical angle of the side cutting edge and the specially-made grinding-wheel is set at $\mathbf{Y}^{\mathrm{M}}$ coordinate with a proper height in terms of the end-mill. The grinding-wheel rotates in high speed; and while rotating with a proper angular velocity, the end-mill is fed against the grinding-wheel. Since the cross-sectional curve of the flute is uniform along the side cutting edge, the flute can be precisely ground. However, the flutes of tapered end-mills (or with tapered cores) are more complicated, and the current approach cannot be applied to machining these flutes.

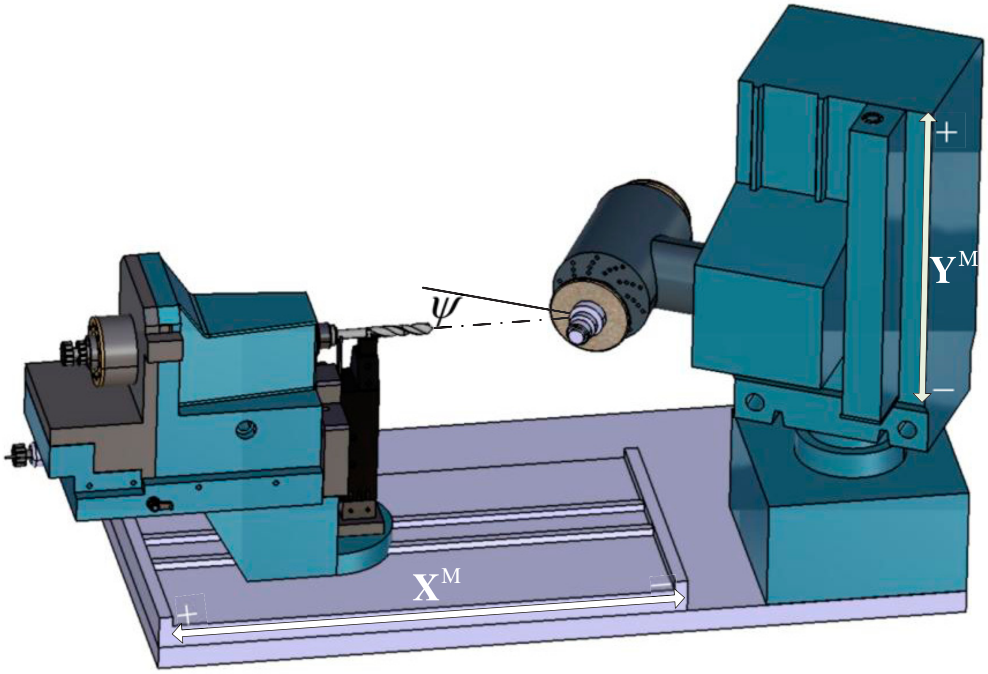

Figure 3.13: Illustration of the kinematics of a 2-axis tool grinding machine.

To illustrate the problem of grinding the flutes of the tapered end-mills in 2-axis CNC grinding, an example of grinding four straight flutes of a tapered end-mill is provided here. Assuming the end-mill flutes shapes as described in Fig. 3.14, and for seeking of simplicity without losing the generality, let the helical angle to be zero. Then, the side cutting edge will be represented on the figure as line coincident with $\mathbf{x}^{\mathrm{T}}$-axis.

It is obvious that the side cutting edge of the ground end-mill is different from the side cutting edge of the designed one. This difference increases with decreasing the cross-section. Moreover, for smaller cross-sections, the rake face is diminishing and resulting in inaccurate radial rake angle, the relief surfaces are also diminishing and thus a compensation method will be required.

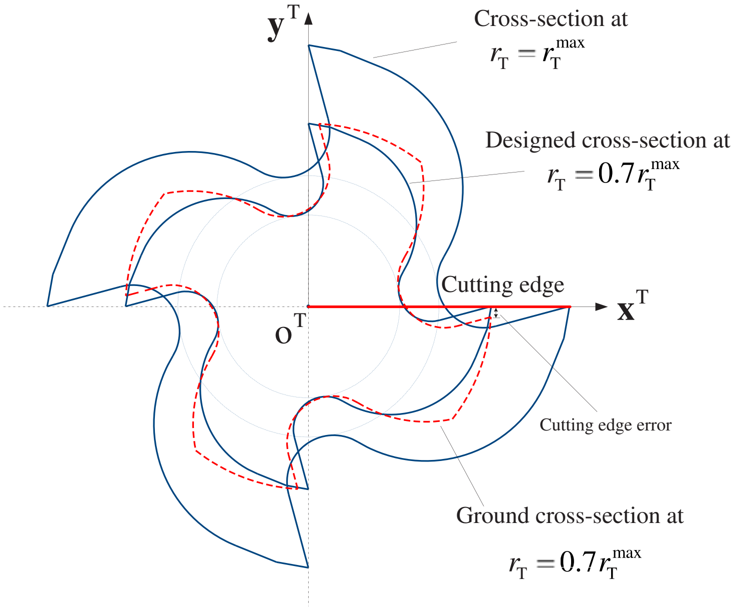

(a) End-mill section at $r_{\mathrm{T}} = 0.7 r_{\mathrm{T}}^{\max}$

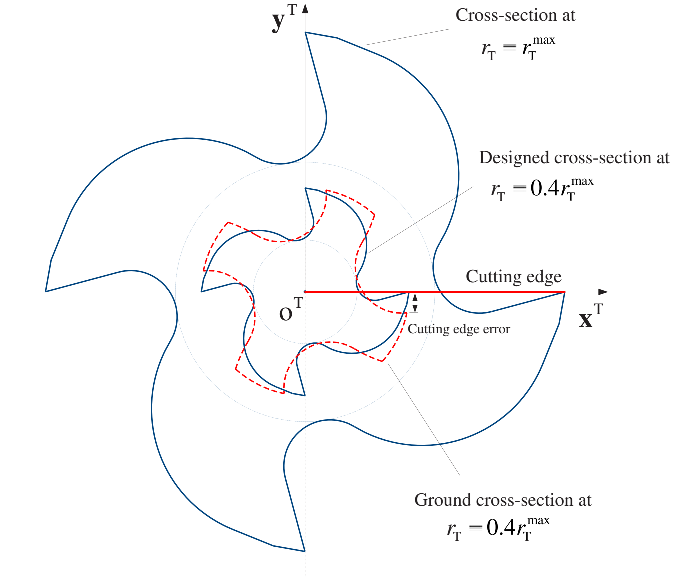

(b) End-mill section at $r_{\mathrm{T}} = 0.4 r_{\mathrm{T}}^{\max}$

Figure 3.14: Effect of the cross-sectional reduction on the final shape of the end-mill and the accuracy of the cutting edge.

In industry, it is necessary to machine the flutes of the tapered end-mills with the prescribed rake angle and flute shape. Besides, it is always expected to make and dress the non-standard grinding-wheel more conveniently and economically. To meet these requirements, the grinding-wheel profile should consist of simple geometries, e.g., line segments and circular arcs, instead of a free-form curve. More importantly, the flutes should be accurately machined in 5-axis CNC grinding. To overcome the aforementioned problems, one goal of this dissertation is to develop a new inverse method for machining the tapered end-mill flutes in 5-axis grinding.

3.7 Summary

The inverse method grinding has a simple relative motion between the grinding-wheel and the end-mill. The flute shape obtained is exact at the major cross-section. However, no control on the flutes shapes exist when moving along the tool axis toward smaller cross-sections, the side cutting edge is inaccurate, the radial rake angle is also inaccurate, the rake face and the relief surfaces are diminishing for smaller cross-sections. This will directly impact the accuracy of the tool strength estimation and the tool dynamic analysis, and more vibrations will appear due to the non uniform cutting forces along the side cutting edge.

Chapter 4

Five-Axis CNC Grinding of End–Mill Flutes using the Direct Method

4.1 Introduction

As a main type of cutting tools, tapered end-mills are often used to machine parts with deep shapes. To cut them, long tools have to be used; unfortunately, long cylindrical end-mills are less rigid, resulting in unacceptable deflection during machining. Comparatively, long tapered end-mills are more rigid to have much less deflection while cutting deep shapes. For a tapered end-mill, its flute geometries substantially affect the tool rigidity and the cutting forces in machining. By definition, a flute includes a flute surface and a rake face along a helical side cutting edge; the two surfaces are next to each other. The rake angle of the rake face determines the cutting forces. The flute surface determines the core radius and the tool area moment of inertia; it also provides space for chip evacuation. Thus, the flutes of a tool affect its cutting performance and life. To make the flutes, currently, there are two methods: the direct and the inverse methods. In the direct method for 5-axis grinding of a flute of a tapered end-mill, a standard wheel is subjectively selected, the wheel orientation and location (WOL) are approximately calculated, and then it grinds the flute along the side cutting edge to generate the rake face and the flute surface simultaneously. This process can make the rake face with the specified rake angle; however, the desired core radius is not guaranteed, and the machining error can reduce the tool rigidity. To address this problem, it is important to develop a new automated and accurate CNC programming approach to 5-axis flute grinding in the direct method so that the rake angle and the core radius can be ensured. Therefore, it is one of the main objectives of our research work.

Thus, our innovative work establishes a NC programming theory for 5-axis grinding of tapered end-mill flutes with standard profile grinding-wheels and constructs genuine geometric models of machined flutes, which are necessary for finite element analysis with high fidelity. In this chapter, first, the current end-mill geometric model is provided. Second, the generic mathematical equations of grinding-wheel locations and orientations in 5-axis grinding of tapered end-mill flutes are derived as a new multi-axis CNC programming theory. Finally, the mechanism of the 5-axis flute grinding machine is introduced and related to the wheel locations and orientations derived.

4.2 Geometric Fundamentals of Solid Carbide Tapered End–Mill Flutes

A solid carbide tapered end-mill mainly includes several geometric features, such as several helical flutes and the corresponding side and bottom cutting edges, the first and the second flank faces of each cutting edge, a gash on the bottom, and the central core. In this work, a helical flute is defined with a flute surface and a rake face along the side cutting edge; the reason for defining a flute in such a way is that a flute is machined with a standard grinding-wheel along a specified path in the direct method. Since the flutes of a solid carbide tapered end-mill are important to the tool performance and life, our research is focused on accurate machining of the flutes. Due to the complex shape of the flutes, they are often machined with 5-axis CNC grinding; unfortunately, the CNC programming technique for 5-axis flute grinding has not fully established and the flute cannot be accurately machined. To develop an advanced programming approach, the basis geometry of a tapered end-mill flute is introduced first.

Theoretically, a solid carbide tapered end-mill can be first designed with a commercial CAD/CAM software system, and then it can be made on a 2-axis CNC grinding machine. This is called the inverse flute machining method. As an important feature of the tool, the flute is designed in a way that the flute cross-section profile is defined and swept along the helical side cutting edge as discussed earlier in Chapter

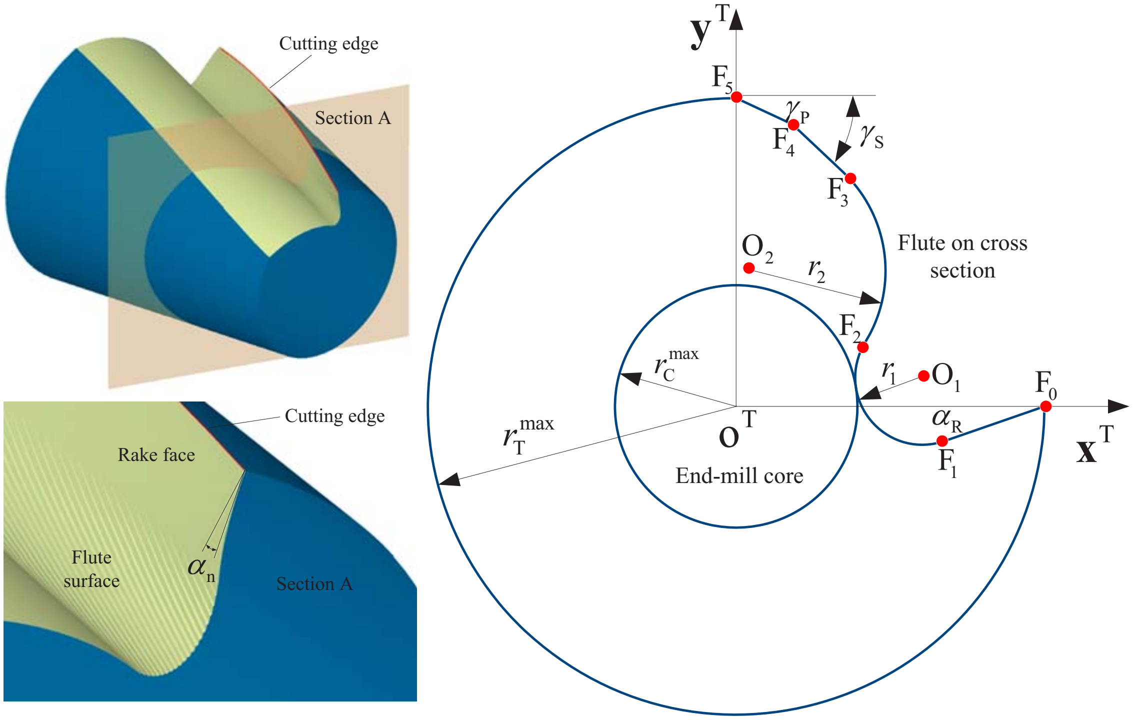

Figure 4.1: A general flute design of a four flute end-mill on the tool coordinate system.

3 (Fig. 4.1).

To machine the flutes, compared to the aforementioned inverse method, the direct method is more popular in the tool manufacturing companies. In this method, a standard grinding-wheel is selected subjectively, and then the grinding-wheel moves along its path in the 5-axis CNC grinding. Since the key parameters of the flutes are the rake angle and the core diameter, their accuracy should be ensured during machining. Regarding the flute shape, it is widely accepted that the flute shape is less important to the tool performance and life; thus, it is more flexible without any machining tolerance specified, and the actual shape is mainly dependent on the shape of the selected grinding-wheel. Therefore, one of the objectives of this work is to establish a new CNC programming technique for 5-axis flute grinding with a variety of standard grinding-wheels. More specifically, based on a selected grinding-wheel, its orientation and location in the 5-axis grinding should be determined automatically and accurately so that the specified rake angle and the core diameter are guaranteed. Due to the large flexibility of the flute shape, the way of grinding-wheel selection is not under investigation in this work.

As guides of the flutes, the side cutting edges of an end-mill are crucial to the 5-axis flute grinding; by natural, they are the paths of the wheel location in the 5-axis CNC program. In this work, the side cutting edges are defined with the parametric representation in the aforesaid tool coordinate system $\Re^{\mathrm{T}}$. Generally, each side cutting edge is a helix on the envelope of the tool, and all of them are evenly distributed around the tool axis. The tool envelope $\mathbf{S}_{\mathrm{T}}$ is a revolution surface, and a longitude of this surface is here called a generatrix. Hence, as a mathematical model of the side cutting edges, the helix has a constant helical angle ψ at any point on the side cutting edge, which is the angle between the corresponding tangent vector of the cutting edge and the generatrix. The end-mill envelope is represented with two parameters: the $\mathbf{z}^{\mathrm{T}}$ coordinate and the rotation angle θ about the $\mathbf{z}^{\mathrm{T}}$-axis. From which, the side cutting edge can be derived as described early in Chapter 3. For instance, the side cutting edge for the tapered ball end-mill shown in Fig. 4.2 can be expressed as

$$\mathbf{C}_{\mathrm{C}}^{\mathrm{T}} = \begin{bmatrix} r(z^{\mathrm{T}})\cos\theta & r(z^{\mathrm{T}})\sin\theta & z^{\mathrm{T}} & 1 \end{bmatrix}^{\mathrm{T}} \tag{4.1}$$

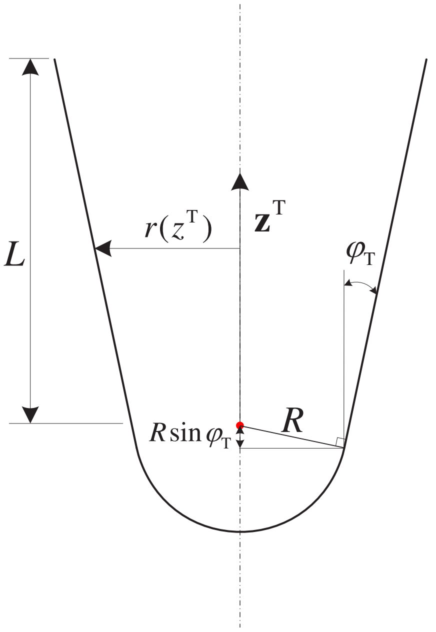

Figure 4.2: Tapered ball end-mill.

where

$$\theta(z^{\mathrm{T}}) = \begin{cases} \frac{\tan\psi}{\sin\varphi_{\mathrm{T}}}\left[\ln\left(\frac{R+z^{\mathrm{T}}\sin\varphi_{\mathrm{T}}}{R\cos^2\varphi_{\mathrm{T}}}\right)\right] & -R\sin\varphi_{\mathrm{T}} \leq z^{\mathrm{T}} \leq L \\ \frac{1}{2}\tan\psi\left[\ln\left(\frac{R+z^{\mathrm{T}}}{R-z^{\mathrm{T}}}\right) - \ln\left(\frac{1-\sin\varphi_{\mathrm{T}}}{1+\sin\varphi_{\mathrm{T}}}\right)\right] & -R \leq z^{\mathrm{T}} \leq -R\sin\varphi_{\mathrm{T}} \end{cases} \tag{4.2}$$

4.3 Unit Normal Vector of the Rake Face

It is well-known that the rake angle of the rake face along the side cutting edge is a critical parameter that determines the cutting forces and the cutting temperature. For clarity, the rake angle is named more specifically according to its position; the radial rake angle α_{R} is the rake angle on a plane perpendicular to the tool axis (see Fig. 4.1), and the normal rake angle is on a plane perpendicular to the tangent vector of the side cutting edge (see Fig. 4.1 and Fig. 4.3). In industry, the rake angle often

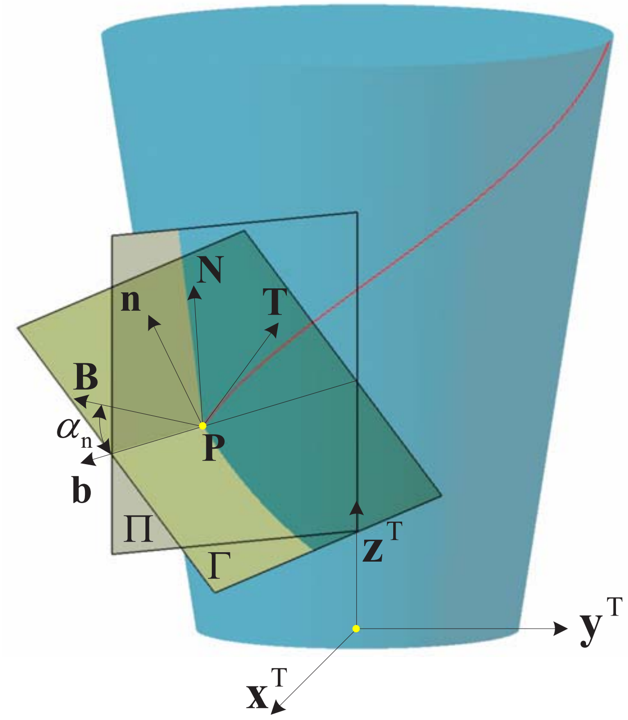

Figure 4.3: The moving coordinate system on the cutting edge.

refers to the normal rake angle. To grind a flute with the specified (normal) rake angle, the grinding-wheel should be properly oriented during machining. Hence, the wheel orientation should be accurately calculated in the 5-axis CNC programming.

According to the geometric model of the 5-axis fluting, a lateral face of the grinding-wheel should be aligned with the rake face, which means that the normal vectors of the two faces are in the same direction. Therefore, it is necessary to find out the unit normal vector of the rake face in the 5-axis CNC programming. To formulate this normal vector, we start with the definition of the normal rake angle. The following diagram, Fig. 4.3, illustrates a normal rake angle at a point on the side cutting edge and the angle-related geometries. The procedure of defining the normal rake angle of a rake face at a cutting edge point **P** is (1) to construct a plane

Γ perpendicular to the cutting edge; and (2) to construct a plane Π perpendicular to the cutting velocity. Here, the plane Γ is perpendicular to the tangent vector $\mathbf{T}$ of the helical cutting edge $\mathbf{C}_{\mathrm{C}}^{\mathrm{T}}$ at point $\mathbf{P}$, and the plane Π passes through the tool axis ($\mathbf{z}^{\mathrm{T}}$-axis) and point $\mathbf{P}$. The intersection between these planes is line $\mathbf{b}$, and the intersection between the plane Γ and the rake face (not shown in Fig. 4.3) is line $\mathbf{B}$. Thus, the angle between the lines $\mathbf{b}$ and $\mathbf{B}$ is the normal rake angle α_{n}. Since the rake face is spanned by $\mathbf{B}$ and $\mathbf{T}$, the normal of this face can be found as the cross product of $\mathbf{B}$ and $\mathbf{T}$. Based on the definition of the normal rake angle, its equation can be formulated in the tool coordinate system $\Re^{\mathrm{T}}$ in the following.

Suppose the coordinate of point $\mathbf{P}$ is $\left(\mathrm{P}_{\mathbf{x}^{\mathrm{T}}}, \mathrm{P}_{\mathbf{y}^{\mathrm{T}}}, \mathrm{P}_{\mathbf{z}^{\mathrm{T}}}\right)$ in the tool coordinate system $\Re^{\mathrm{T}}$. According to the equation of the side cutting edge, Eq.(3.9), the unit tangent vector $\mathbf{T}$ at point $\mathbf{P}$ in $\Re^{\mathrm{T}}$ is

$$\mathbf{T} = \begin{bmatrix} \mathrm{T}_{\mathbf{x}^{\mathrm{T}}} \\ \mathrm{T}_{\mathbf{y}^{\mathrm{T}}} \\ \mathrm{T}_{\mathbf{z}^{\mathrm{T}}} \\ 0 \end{bmatrix} = \frac{d\mathbf{C}_{\mathrm{C}}^{\mathrm{T}}}{\left\| d\mathbf{C}_{\mathrm{C}}^{\mathrm{T}} \right\|} \tag{4.3}$$

To express the unit vector $\mathbf{B}$, first; the normal plane Γ perpendicular to vector $\mathbf{T}$ will have a unit normal vector represented as

$$\mathbf{N}_{\Gamma} = \mathbf{T} \tag{4.4}$$

and second, the reference plane Π will have a unit normal vector expressed as

$$\mathbf{N}_{\Pi} = \begin{bmatrix} -\mathrm{P}_{\mathbf{y}^{\mathrm{T}}} & \mathrm{P}_{\mathbf{x}^{\mathrm{T}}} & 0 & 0 \end{bmatrix}^{\mathrm{T}} \tag{4.5}$$

Now the unit vector $\mathbf{b}$ coinciding with the line of intersection of the two planes is expressed as

$$\mathbf{b} = \begin{bmatrix} \mathrm{b}_{\mathbf{x}^{\mathrm{T}}} & \mathrm{b}_{\mathbf{y}^{\mathrm{T}}} & \mathrm{b}_{\mathbf{z}^{\mathrm{T}}} & 0 \end{bmatrix}^{\mathrm{T}} = \frac{\mathbf{N}_{\Pi} \times \mathbf{N}_{\Gamma}}{\|\mathbf{N}_{\Pi} \times \mathbf{N}_{\Gamma}\|} \tag{4.6}$$

The vector $\mathbf{n}$ is located on the normal plane Γ and perpendicular to both $\mathbf{T}$ and $\mathbf{b}$. Thus

$$\mathbf{n} = \begin{bmatrix} \mathrm{n}_{\mathbf{x}^{\mathrm{T}}} & \mathrm{n}_{\mathbf{y}^{\mathrm{T}}} & \mathrm{n}_{\mathbf{z}^{\mathrm{T}}} & 0 \end{bmatrix}^{\mathrm{T}} = \mathbf{b} \times \mathbf{T} \tag{4.7}$$

Let $\mathbf{b}$ rotate clockwise around $\mathbf{T}$ with angle α_{n}, where α_{n} is the normal rake angle of the rake face along the cutting edge. Then, the unit vector $\mathbf{B}$ is derived as

$$\mathbf{B} = \begin{bmatrix} \mathrm{B}_{\mathbf{x}^{\mathrm{T}}} & \mathrm{B}_{\mathbf{y}^{\mathrm{T}}} & \mathrm{B}_{\mathbf{z}^{\mathrm{T}}} & 0 \end{bmatrix}^{\mathrm{T}} = \begin{bmatrix} \mathrm{T}_{\mathbf{x}^{\mathrm{T}}} & \mathrm{n}_{\mathbf{x}^{\mathrm{T}}} & \mathrm{b}_{\mathbf{x}^{\mathrm{T}}} & 0 \\ \mathrm{T}_{\mathbf{y}^{\mathrm{T}}} & \mathrm{n}_{\mathbf{y}^{\mathrm{T}}} & \mathrm{b}_{\mathbf{y}^{\mathrm{T}}} & 0 \\ \mathrm{T}_{\mathbf{z}^{\mathrm{T}}} & \mathrm{n}_{\mathbf{z}^{\mathrm{T}}} & \mathrm{b}_{\mathbf{z}^{\mathrm{T}}} & 0 \\ 0 & 0 & 0 & 1 \end{bmatrix} \cdot \begin{bmatrix} 0 \\ \sin\alpha_{\mathrm{n}} \\ \cos\alpha_{\mathrm{n}} \\ 0 \end{bmatrix} \tag{4.8}$$

Now, the rake face unit normal vector $\mathbf{N}$ can be expressed as

$$\mathbf{N} = \mathbf{B} \times \mathbf{T} \tag{4.9}$$

In the 5-axis flute grinding, the grinding face should be aligned with the rake face of the tool, therefore, the normal vector of the rake face is used to determine the grinding-wheel orientation in the 5-axis CNC programming.

4.4 Five–axis CNC Grinding of End–Mill Flutes

Solid carbide is very hard, so the grinding manufacturing process has to be used in the tool production. The grinding mechanism is that a large number of tiny grains with sharp edges on the grinding-wheel remove the stock material of parts. Since it is essential for the grains on the wheel peripheral with high cutting speed, the grinding-wheel should be rotated in high angular velocity during machining. Conventionally, the grinding machine tools could only machine parts of regular shapes, i.e., planes, cylinders, and holes; and, as an operation of finish machining, parts are ground by removing a small amount of material for high accuracy and high finish. Now, the 5-axis grinding machine tools can machine complex surfaces by removing relatively a large amount of stock material with high efficiency. The solid carbide end-mills are complex in shape, especially, their flutes; and their two important parameters are the normal rake angle and the core radius. To grind the end-mill flutes with the specified core radius and normal rake angle, the selected grinding-wheel should be properly located and oriented (in terms of the end-mill) on the 5-axis CNC grinding machine tool. Because the volume of the material removed is difficult to determine, currently, the wheel location is approximated, resulting a large deviation of the core radius. Therefore, it is indispensary to accurately model the volume swept by the grinding-wheel in its 5-axis motions; and, with this model, the wheel location can be calculated to ensure the specified core radius after grinding.

Due to the tight tolerances of the core radius and the normal rake angle of a machined tool, the wheel location and orientation should be accurately calculated in the CNC programming. In other words, the specified core radius and the normal rake angle are the criteria for the CNC programming. In this section, the geometric models of the grinding-wheels are established in order to determine the wheel position for 5-axis grinding of an end-mill flute.

4.4.1 Grinding–wheel parametric representations

In industry, there are many types of standard grinding-wheels, and they are often used for production of solid carbide end-mills for these wheels are cheaper, compared to non-standard grinding-wheels. Fig. 4.4 shows three standard grinding-wheels, which are often used to grind the flutes. Since the grinding-wheel in Fig. 4.4b is in the generic shape of the three wheels, the parametric equation of this wheel can be used to represent the other wheels. Thus, the parametric equation is derived here. First, a coordinate system $\Re^{\mathrm{G}} =: \left(\mathrm{o}^{\mathrm{G}}\mathbf{x}^{\mathrm{G}}\mathbf{y}^{\mathrm{G}}\mathbf{z}^{\mathrm{G}}\right)$ is established. The origin o^{G} of $\Re^{\mathrm{G}}$ is located on the right face of the grinding-wheel and the $\mathbf{z}^{\mathrm{G}}$-axis is aligned with the wheel axis and pointing to the left. The $\mathbf{x}^{\mathrm{G}}$- and $\mathbf{y}^{\mathrm{G}}$-axes are on the right face and are perpendicular with each other. The parameters, R_0, t_{G}, α_{G} and T are labeled in the diagram. In this coordinate system, the parametric representation of the wheel is provided in the following.

$$\mathbf{S}_{\mathrm{W}}\left(u,v\right) = \begin{bmatrix} R_{\mathrm{W}}(u)\cdot\cos v & R_{\mathrm{W}}(u)\cdot\sin v & u & 1 \end{bmatrix}^{\mathrm{T}} \tag{4.10}$$

where $0 \leq v \leq 2\pi$,

$$R_{\mathrm{W}}(u) = \begin{cases} R_0 + \frac{u}{\tan\alpha_{\mathrm{G}}} & 0 \leq u \leq t_{\mathrm{G}}\cdot\sin\alpha_{\mathrm{G}} \\ x_{\mathrm{G}} + \sqrt{\rho^2 - \left(u - z_{\mathrm{G}}\right)^2} & t_{\mathrm{G}}\cdot\sin\alpha_{\mathrm{G}} \leq u \leq T \end{cases} \tag{4.11}$$

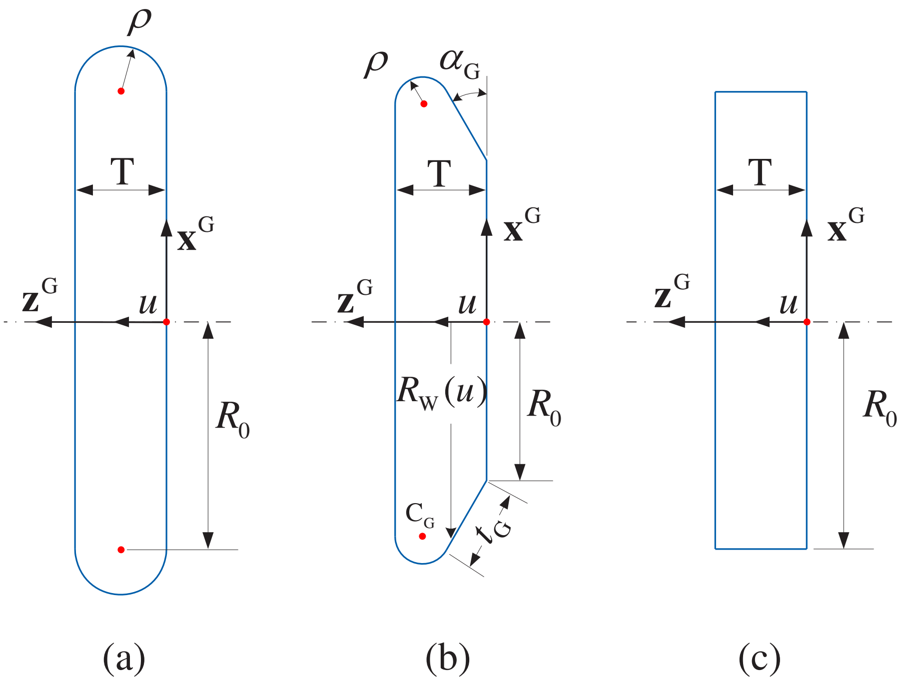

Figure 4.4: Grinding-wheels of standard shapes.

and $C_G = \begin{bmatrix} x_G \\ y_G \\ z_G \end{bmatrix}$

4.4.2 Determination of the grinding–wheel orientation

Solid carbide end-mills have different normal rake angles, and those tools are used to cut different metals. To machine a part of a specific metal, an appropriate rake angle of the tool can effectively reduce the cutting forces and the cutting edge temperature, and it can also increase the cutting edge strength and tool life. The normal rake angle is very important, therefore, it has to be ensured in machining. To grind a rake face with the specified normal rake angle along its corresponding side cutting edge, the selected grinding-wheel should be properly oriented so that one of its lateral faces always contacts with the rake face at any point on the side cutting edge. Thus, the mathematical model of grinding the rake face is that the unit normal of the rake face is in the opposite direction of the unit normal of the lateral face. Based on this model, the wheel axis direction can be found; this direction is the wheel orientation of the 5-axis grinding.

To establish the mathematical model of the rake face grinding, the geometric relationship between the grinding-wheel and the flute of the tool is illustrated in Fig. 4.5. First, a point $\mathbf{P}_{\mathrm{W}}(u,v)$ on the wheel surface and represented in the wheel coordinate system $\Re^{\mathrm{G}}$ is chosen. Second, the surface normal $\mathbf{N}_{\mathrm{W}}(u,v)$ at point $\mathbf{P}_{\mathrm{W}}(u,v)$ in $\Re^{\mathrm{G}}$ is found. Then, assuming the tool coordinate system $\Re^{\mathrm{T}}$ is stationary, the grinding-wheel is re-orientated so that the wheel surface normal $\mathbf{N}_{\mathrm{W}}(u,v)$ is aligned with the rake face normal $\mathbf{N}\left(\mathbf{z}_{\mathrm{C}}^{\mathrm{T}},\theta_{\mathrm{C}}\right)$ but in the opposite direction. Since $\mathbf{N}_{\mathrm{W}}(u,v)$ is represented in $\Re^{\mathrm{G}}$, it has to be transformed into the tool coordinate system $\Re^{\mathrm{T}}$. More specifically, to align $\mathbf{N}_{\mathrm{W}}(u,v)$ with $\mathbf{N}\left(\mathbf{z}_{\mathrm{C}}^{\mathrm{T}},\theta_{\mathrm{C}}\right)$ in the way aforementioned, three steps are proceeded in a consecutive way: (1) to coincide the two coordinate systems, $\Re^{\mathrm{G}}$ with $\Re^{\mathrm{T}}$; (2) to rotate $\mathbf{N}_{\mathrm{W}}(u,v)$ about the $\mathbf{x}^{\mathrm{T}}$-axis by angle μ, and (3) to rotate $\mathbf{N}_{\mathrm{W}}(u,v)$ about the $\mathbf{z}^{\mathrm{T}}$-axis by angle η

Using Eq.(4.9), the unit normal $\mathbf{N}\left(\mathbf{z}_{\mathrm{C}}^{\mathrm{T}},\theta_{\mathrm{C}}\right)$ of the rake face at point $\mathbf{P}\left(\mathbf{z}_{\mathrm{C}}^{\mathrm{T}},\theta_{\mathrm{C}}\right)$ can be calculated in the tool coordinate system $\Re^{\mathrm{T}}$. The unit normal vector $\mathbf{N}_{\mathrm{W}}(u,v)$ at $\mathbf{P}_{\mathrm{W}}(u,v)$, $\mathbf{N}_{\mathrm{W}}^{\mathrm{T}}$, can be derived by first calculating $\mathbf{N}_{\mathrm{W}}^{\mathrm{G}}$, where the superscripts T

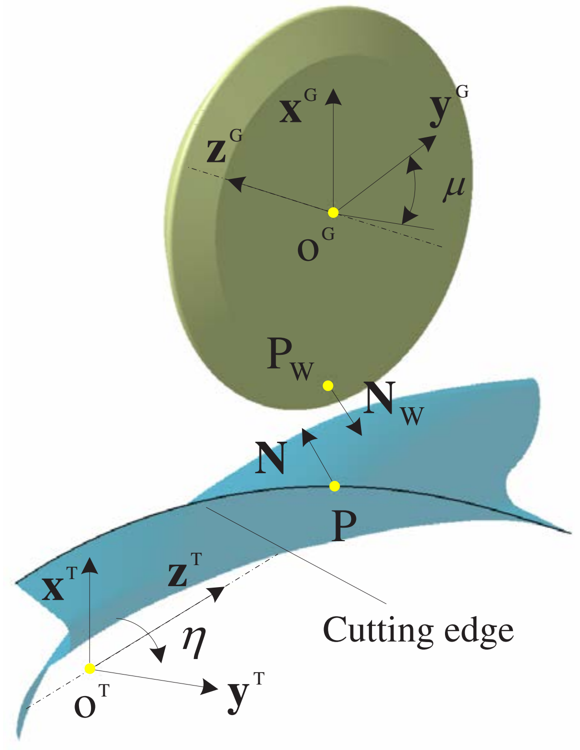

Figure 4.5: Wheel–side cutting edge interaction.

and G are to relate the vector to $\Re^{\mathrm{T}}$ and $\Re^{\mathrm{G}}$ coordinate systems, respectively.

$$\mathbf{N}_{\mathrm{W}}^{\mathrm{G}}(u,v)=\frac{\frac{\partial\mathbf{S}_{\mathrm{W}}}{\partial u}\times\frac{\partial\mathbf{S}_{\mathrm{W}}}{\partial v}}{\left\|\frac{\partial\mathbf{S}_{\mathrm{W}}}{\partial u}\times\frac{\partial\mathbf{S}_{\mathrm{W}}}{\partial v}\right\|}\tag{4.12}$$

Then, $\mathbf{N}_{\mathrm{W}}^{\mathrm{G}}(u,v)$ is rotated about the $\mathbf{x}^{\mathrm{T}}$-axis by angle μ, the transformation matrix is

$$\mathrm{ROT}(\mu,x)=\begin{bmatrix}1 & 0 & 0 & 0\\ 0 & \cos\mu & -\sin\mu & 0\\ 0 & \sin\mu & \cos\mu & 0\\ 0 & 0 & 0 & 1\end{bmatrix}\tag{4.13}$$

Then, $\mathbf{N}_{\mathrm{W}}^{\mathrm{G}}(u,v)$ is rotated about the $\mathbf{z}^{\mathrm{T}}$-axis by angle η, the transformation matrix is

$$\mathrm{ROT}(\eta,z)=\begin{bmatrix}\cos\eta & -\sin\eta & 0 & 0\\ \sin\eta & \cos\eta & 0 & 0\\ 0 & 0 & 1 & 0\\ 0 & 0 & 0 & 1\end{bmatrix}\tag{4.14}$$

Finally, $\mathbf{N}_{\mathrm{W}}(u,v)$ can be represented in the tool coordinate system $\Re^{\mathrm{T}}$ as

$$\mathbf{N}_{\mathrm{W}}^{\mathrm{T}}(u,v)=\mathrm{ROT}(\eta,z)\cdot\mathrm{ROT}(\mu,x)\cdot\mathbf{N}_{\mathrm{W}}^{\mathrm{G}}(u,v)\tag{4.15}$$

Therefore, the wheel surface normal is in the opposite direction of the rake face normal. Since they are represented in the tool coordinate system $\Re^{\mathrm{T}}$, the equation of the mathematical model of grinding the rake face is

$$\mathbf{N}(z_{\mathrm{C}}^{\mathrm{T}},\theta_{\mathrm{C}})+\mathbf{N}_{\mathrm{W}}^{\mathrm{T}}(u,v)=0\tag{4.16}$$

By using Eq.(4.16), the two rotation angles, μ and η, can be solved, and the grinding-wheel can be re-orientated so that the normal rake angle of the rake face can be accuratly obtained in the 5-axis fluting (see the appendix).

4.4.3 Determination of the grinding–wheel location

In order to calculate the wheel location, the point selected previously on the grinding-wheel in the wheel coordinate system $\Re^{\mathrm{G}}$, $\mathbf{P}_{\mathrm{W}}(u,v)$, is first represented in the tool coordinate system $\Re^{\mathrm{T}}$ as

$$\mathbf{P}^{\mathrm{T}}_{\mathrm{W}}(u,v) = \mathbf{T}\left(\mathrm{o}^{\mathrm{G}}_{\mathbf{x}^{\mathrm{T}}}, \mathrm{o}^{\mathrm{G}}_{\mathbf{y}^{\mathrm{T}}}, \mathrm{o}^{\mathrm{G}}_{\mathbf{z}^{\mathrm{T}}}\right) \cdot \mathrm{ROT}(\eta, z) \cdot \mathrm{ROT}(\mu, x) \cdot \mathbf{P}_{\mathrm{W}}(u,v) \tag{4.17}$$

By coinciding $\mathbf{P}^{\mathrm{T}}_{\mathrm{W}}(u,v)$ with point $\mathbf{P}\left(\mathbf{z}^{\mathrm{T}}_{\mathrm{C}}, \theta_{\mathrm{C}}\right)$ at the cutting edge, the grinding-wheel location o^{G} in the tool coordinate system $\Re^{\mathrm{T}}$, $\left(\mathrm{o}^{\mathrm{G}}_{\mathbf{x}^{\mathrm{T}}}, \mathrm{o}^{\mathrm{G}}_{\mathbf{y}^{\mathrm{T}}}, \mathrm{o}^{\mathrm{G}}_{\mathbf{z}^{\mathrm{T}}}\right)$, can be derived (see the appendix).

At this point, it is worth to tell that the grinding-wheel location and orientation are affected by the selection of point $\mathbf{P}_{\mathrm{W}}(u,v)$. Hence, the flute shape will also be affected. Therefore, using a proper point will guarantee accurate core radius for the end-mill cutting tools as will be shown in the proceeding sections.

4.4.4 The effective grinding edge in five–axis CNC grinding

The main objective of the CNC programming for the 5-axis flute grinding is to calculate the grinding-wheel location and orientation in terms of the end-mill. A kernel technique is to accurately and efficiently represent the geometry of the wheel swept volume in the 5-axis CNC grinding. Since the kinematics of the 5-axis grinding and milling are similar and the 5-axis milling has been under extensive research, it would be easier and clearer to describe the 5-axis flute grinding in comparison with the 5-axis surface milling. For the 5-axis milling, the orientation of the cutting tool can be simultaneously changed while the tool moving along the pre-planned paths, in order to achieve better geometric match between the tool and the part local surface without gouging and interference. From the geometric point of view, the tool sweeps a complex volume, in which the stock material is removed; and the exterior surface of this volume mathematically is the envelope of the tool revolving surface at different locations in the 5-axis milling process. This envelope is called cutter swept surface. Actually, a cutter swept surface is composed of the effective cutting edges at different tool locations, which is defined as the silhouette boundary of the tool revolving surface in the tool velocity direction at a location (see Fig. 4.6). With the effective cutting edge, the cutter swept surface can be easily constructed, and the 5-axis CNC tool paths can be generated. Basically, the geometric feature of the 5-axis flute grinding is similar to that of the 5-axis surface milling.

To ensure the specified core radius and normal rake angle of the end-mill flutes, the flutes have to be cut on the 5-axis grinding machine tool, and the disk-alike grinding-wheel should be properly located and oriented, respectively. During machining, the grinding-wheel moves along the helical side cutting edge, sweeping an imaginary volume. In this work, the volume is called wheel swept volume, and any workpiece material inside the volume is removed. The mathematical model of the wheel swept volume is the envelope of the wheel exterior surface at different locations during grinding; and at a wheel location, the envelope element is a curve, which is

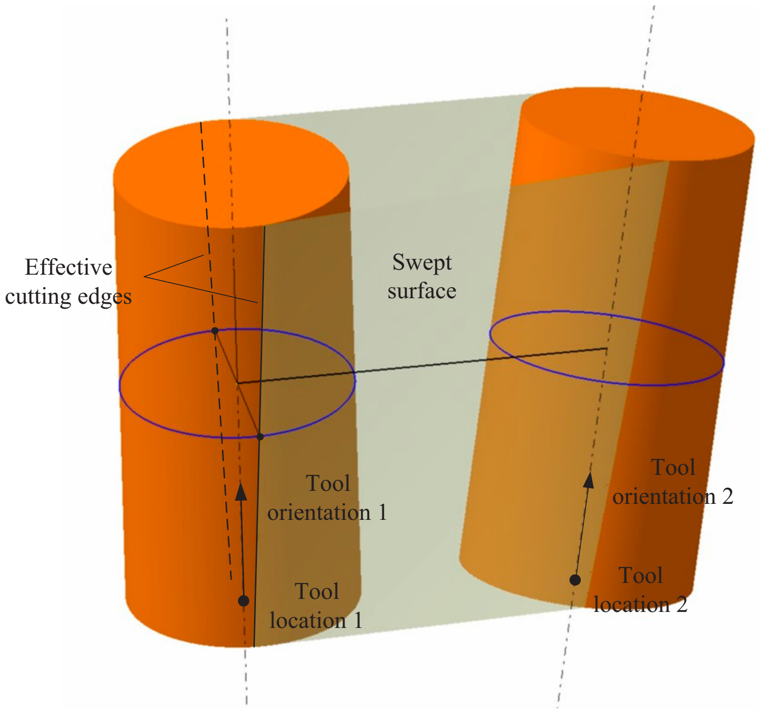

Figure 4.6: The effective cutting edge and the envelope of the tool revolving surface at two adjacent locations.

called the effective grinding edge in this work. An effective grinding edge is defined as the wheel surface points at which the surface normals are perpendicular to the instantaneous wheel velocity at a wheel position (WP). A wheel position refers to the wheel center location and the wheel axis direction in the tool coordinate system $\Re^{\mathrm{T}}$. Therefore, the wheel swept surface can be represented by finding the effective grinding edge of the wheel at any moment of the machining process. Fig. 4.7 shows that a grinding-wheel cuts from position 1 to position 2 in the 5-axis grinding. In this cut, the effective grinding edges at the two locations and the swept surface they generate are plotted. Due to the complicated kinematics of the 5-axis grinding, the effective grinding edge is not simply the wheel profile; it varies at different positions and is a curve on the wheel surface. Therefore, the wheel swept surface could be quite complex in shape. In this work, we derive a closed-form equation of the effective grinding edge by first establishing a mathematical model for the wheel swept surface as shown in the following section.

4.4.5 Mathematical model of the grinding–wheel swept surface

The motion of the grinding-wheel along the wheel path will form the swept volume that can be represented as

$$\mathbf{S}_{\mathrm{V}}\left(u, v, t\right) = \mathrm{T}\left(\mathrm{o}^{\mathrm{G}}_{\mathbf{x}^{\mathrm{T}}}, \mathrm{o}^{\mathrm{G}}_{\mathbf{y}^{\mathrm{T}}}, \mathrm{o}^{\mathrm{G}}_{\mathbf{z}^{\mathrm{T}}}\right) \cdot \mathrm{ROT}(\eta, z) \cdot \mathrm{ROT}(\mu, x) \cdot \mathbf{S}_{\mathrm{W}}(u, v) \tag{4.18}$$

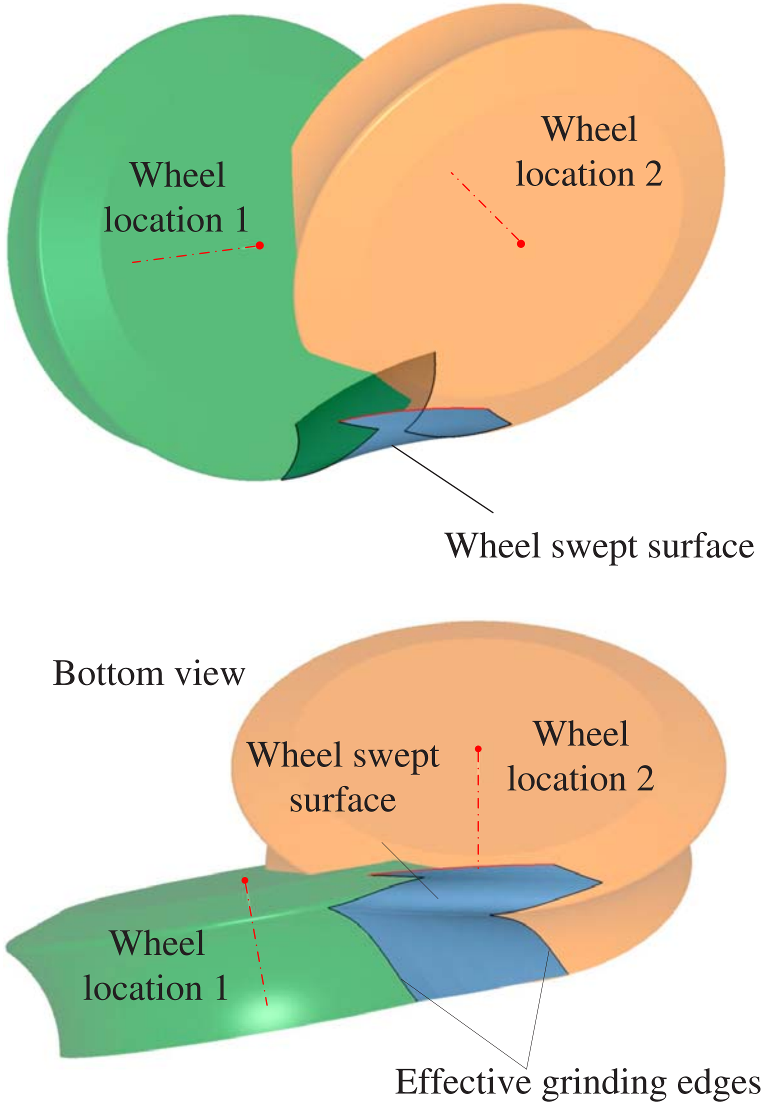

Figure 4.7: The effective grinding edge and the envelope of the grinding-wheel revolving surface at two adjacent locations.

where

$$\mathrm{T}\left(\mathrm{o}^{\mathrm{G}}_{\mathbf{x}^{\mathrm{T}}}, \mathrm{o}^{\mathrm{G}}_{\mathbf{y}^{\mathrm{T}}}, \mathrm{o}^{\mathrm{G}}_{\mathbf{z}^{\mathrm{T}}}\right) = \begin{bmatrix} 1 & 0 & 0 & \mathrm{o}^{\mathrm{G}}_{\mathbf{x}^{\mathrm{T}}} \\ 0 & 1 & 0 & \mathrm{o}^{\mathrm{G}}_{\mathbf{y}^{\mathrm{T}}} \\ 0 & 0 & 1 & \mathrm{o}^{\mathrm{G}}_{\mathbf{z}^{\mathrm{T}}} \\ 0 & 0 & 0 & 1 \end{bmatrix} \tag{4.19}$$

To obtain the swept envelope (flute surface), one parameter should be eliminated from $\mathbf{S}_{\mathrm{V}}$; this is achieved using the envelope theory

$$|J| = \begin{vmatrix} \frac{\partial \mathbf{S}_{\mathrm{V}}}{\partial u} & \frac{\partial \mathbf{S}_{\mathrm{V}}}{\partial v} & \frac{\partial \mathbf{S}_{\mathrm{V}}}{\partial t} \end{vmatrix} = 0 \tag{4.20}$$

Re-arranging, we get Eq.(4.20) in the form

$$a \cdot \cos v + b \cdot \sin v = c \tag{4.21}$$

where

$$\begin{aligned} a &= \left(\dot{\mathrm{o}}^{\mathrm{G}}_{\mathrm{x}^{\mathrm{T}}}\right) \cos\eta + \left(\dot{\mathrm{o}}^{\mathrm{G}}_{\mathrm{y}^{\mathrm{T}}}\right) \cdot \sin\eta - u \cdot \dot{\eta} \cdot \sin\mu + R_{\mathrm{W}} \cdot \tfrac{\partial R_{\mathrm{W}}}{\partial u} \cdot \dot{\eta} \cdot \sin\mu \\ b &= \left(\dot{\mathrm{o}}^{\mathrm{G}}_{\mathrm{y}^{\mathrm{T}}}\right) \cdot \cos\mu\cos\eta - \dot{\mu} \cdot u + \left(\dot{\mathrm{o}}^{\mathrm{G}}_{\mathrm{z}^{\mathrm{T}}}\right) \cdot \sin\mu - \left(\dot{o}^{\mathrm{G}}_{\mathrm{x}^{\mathrm{T}}}\right) \cdot \cos\mu\sin\eta - R_{\mathrm{W}} \cdot \tfrac{\partial R_{\mathrm{W}}}{\partial u} \cdot \dot{\mu} \\ c &= -\left(\dot{\mathrm{o}}^{\mathrm{G}}_{\mathrm{z}^{\mathrm{T}}}\right) \cdot \tfrac{\partial R_{\mathrm{W}}}{\partial u} \cdot \cos\mu + \left(\dot{\mathrm{o}}^{\mathrm{G}}_{\mathrm{y}^{\mathrm{T}}}\right) \cdot \tfrac{\partial R_{\mathrm{W}}}{\partial u} \cdot \sin\mu\cos\eta - \left(\dot{o}^{\mathrm{G}}_{\mathrm{x}^{\mathrm{T}}}\right) \cdot \tfrac{\partial R_{\mathrm{W}}}{\partial u} \cdot \sin\mu\sin\eta \end{aligned} \tag{4.22}$$

If $\left|c/\sqrt{a^2+b^2}\right| \leq 1$, the following relationship will be obtained

$$v(u,t) = \begin{cases} \sin^{-1}\left(\frac{c}{\sqrt{a^2+b^2}}\right) - \phi \\ \pi - \sin^{-1}\left(\frac{c}{\sqrt{a^2+b^2}}\right) - \phi \end{cases} \tag{4.23}$$

where

$$\sin\phi = \frac{a}{\sqrt{a^2+b^2}} \qquad \text{and} \qquad \cos\phi = \frac{b}{\sqrt{a^2+b^2}} \tag{4.24}$$

Substitute the relationship obtained from Eq.(4.23) into Eq.(4.18) to get the flute surface

$$\mathbf{S}_{\mathrm{F}} = \mathbf{S}_{\mathrm{V}}\left(u, v\left(u,t\right), t\right) \tag{4.25}$$

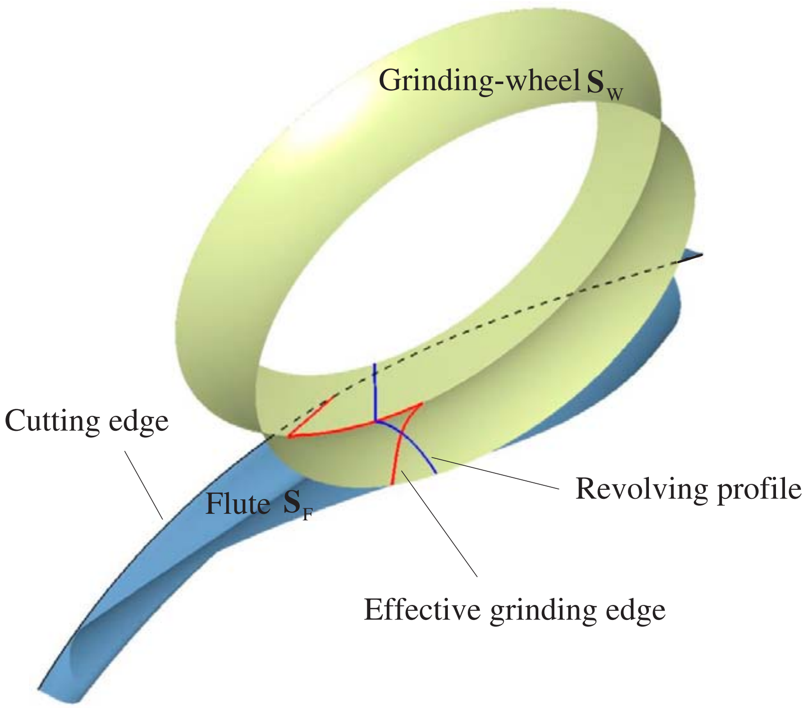

Figure 4.8: The ground flute surface.

as shown in Fig. 4.8. The flute surface can be imagined as an infinite family of contact curves (effective grinding edges) guided by the side cutting edge.

4.5 Five–Axis Tools Grinding Machines

With development of the 5-axis grinding machine tools, such as WALTER, ROLLOMATIC and ANCA machines, solid carbide end-mills can be ground with higher accuracy and quality, compared to the conventional method of grinding tools manually. Particularly, the end-mill flutes have to be machined with the 5-axis CNC grinding since their geometry is quite complicated. Fig. 4.9 shows the configuration of a general 5-axis grinding machine tool, and the machine coordinate system

$\Re^{\mathbf{M}}$ =: $(\mathrm{O}^{\mathrm{M}}\mathbf{X}^{\mathrm{M}}\mathbf{Y}^{\mathrm{M}}\mathbf{Z}^{\mathrm{M}})$ includes the $\mathbf{X}^{\mathrm{M}}$, $\mathbf{Y}^{\mathrm{M}}$, $\mathbf{Z}^{\mathrm{M}}$, $\mathbf{B}^{\mathrm{M}}$ and $\mathbf{C}^{\mathrm{M}}$ axes. On this machine tool, the grinding-wheel can translate along the $\mathbf{X}^{\mathrm{M}}$, $\mathbf{Y}^{\mathrm{M}}$ and $\mathbf{Z}^{\mathrm{M}}$ axes and rotate about the $\mathbf{B}^{\mathrm{M}}$ and $\mathbf{C}^{\mathrm{M}}$ axes simultaneously in order to machine complex geometries.

The relationship governing this coordinate system with $\Re^{\mathrm{T}} := \left(\mathrm{o}^{\mathrm{T}}\mathbf{x}^{\mathrm{T}}\mathbf{y}^{\mathrm{T}}\mathbf{z}^{\mathrm{T}}\right)$ coordinate system is fully dependent on the grinding-machine considered. Here, for the machine adopted, using proper transformations, the axes motions of the grinding-machine can be related to the grinding-wheel locations and orientations obtained previously, those relationships are expressed as

$$\begin{bmatrix} \mathbf{X}^{\mathrm{M}} \\ \mathbf{Y}^{\mathrm{M}} \\ \mathbf{Z}^{\mathrm{M}} \\ 1 \end{bmatrix} = \begin{bmatrix} 0 & -\cos\mathbf{B}^{\mathrm{M}} & -\sin\mathbf{B}^{\mathrm{M}} & d_x \\ 1 & 0 & 0 & d_y \\ 0 & -\sin\mathbf{B}^{\mathrm{M}} & \cos\mathbf{B}^{\mathrm{M}} & d_z \\ 0 & 0 & 0 & 1 \end{bmatrix} \begin{bmatrix} \mathrm{o}^{\mathrm{G}}_{\mathbf{x}^{\mathrm{T}}} \\ \mathrm{o}^{\mathrm{G}}_{\mathbf{y}^{\mathrm{T}}} \\ \mathrm{o}^{\mathrm{G}}_{\mathbf{z}^{\mathrm{T}}} - \mathrm{o}^{\mathrm{T}}\mathrm{o}^{\mathrm{B}} \\ 1 \end{bmatrix} \tag{4.26a}$$

$$\begin{aligned} \mathbf{B}^{\mathrm{M}} &= \mu \\ \mathbf{C}^{\mathrm{M}} &= -\eta \end{aligned} \tag{4.26b}$$

where d_x, d_y and d_z are the $\mathbf{X}^{\mathrm{M}}$, $\mathbf{Y}^{\mathrm{M}}$ and $\mathbf{Z}^{\mathrm{M}}$ components of a vector starting at o^{G} and ending at o^{B} at the time the machine is located at its home position.

4.6 Applications

In order to verify the grinding approach proposed, grinding simulation is conducted for cylindrical end-mills and tapered end-mills using different standard grinding-wheels (Fig. 4.10).

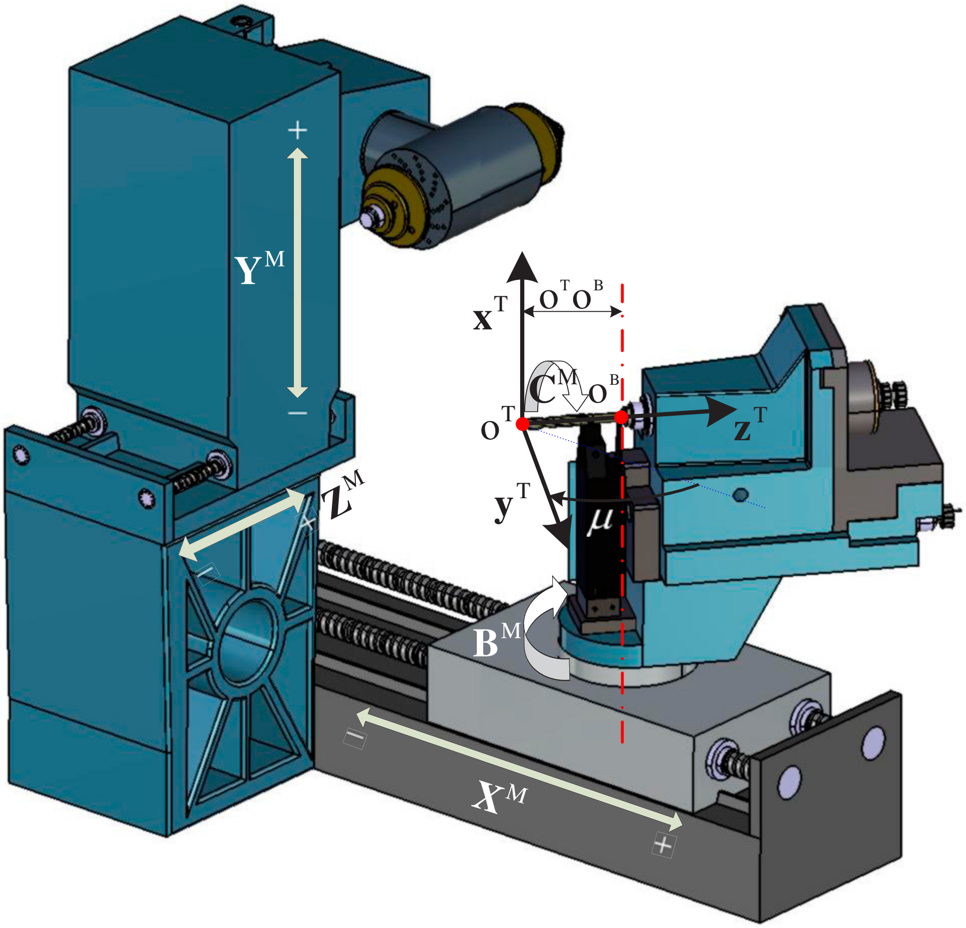

Figure 4.9: The configuration of a 5-axis CNC grinding machine.

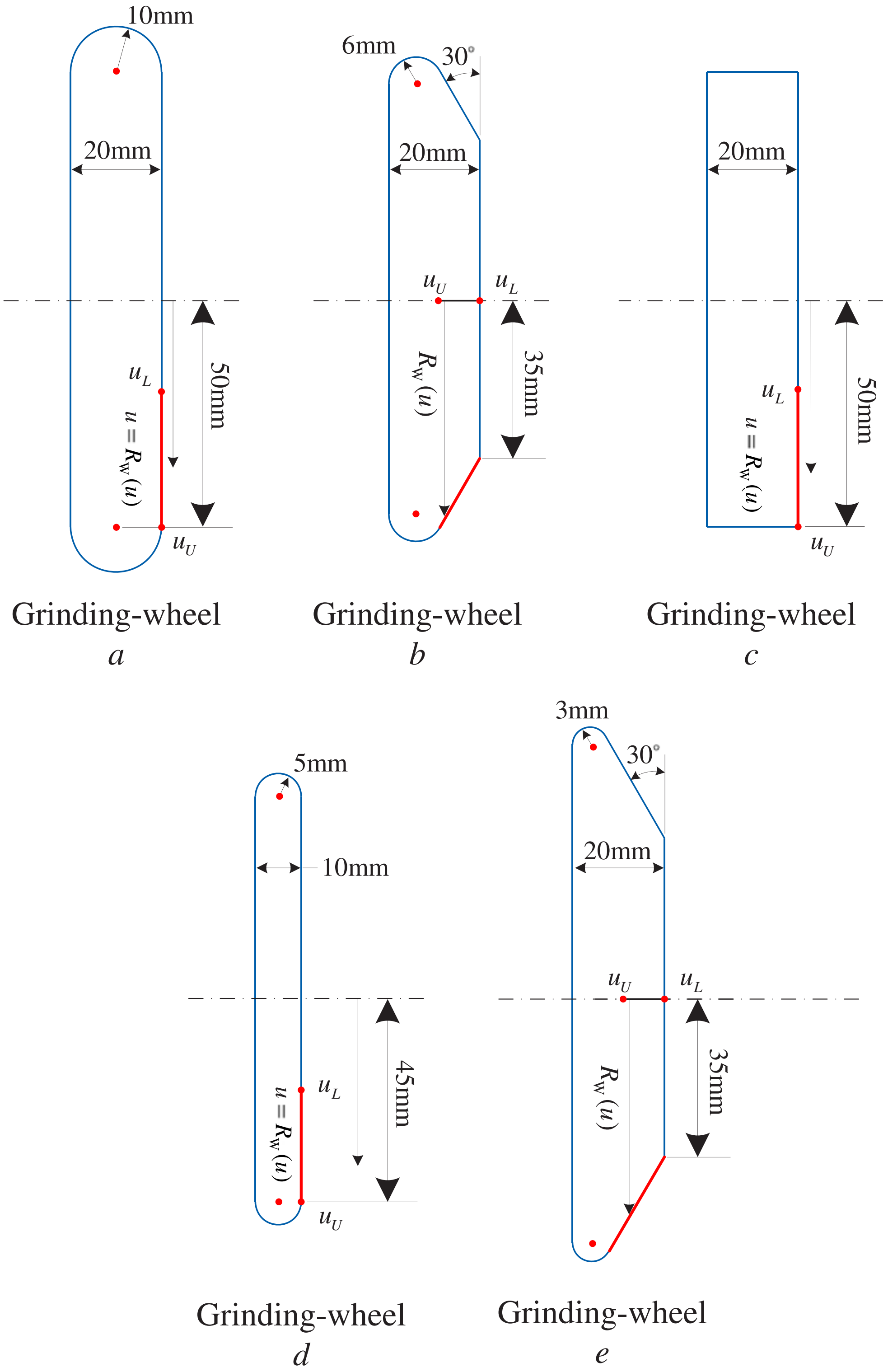

Figure 4.10: Standard grinding-wheels used to grind the end-mill flutes.

Table 4.1: Description of cylindrical end-mills grinding processes.

Grinding Process	Grinding wheel	End-mill outer radius	End-mill core radius	Helical angle (ψ)	Normal rake angle (α_{n})	u_L	u_U
I	a	25mm	12.5mm	20°	10°	45mm	50mm
II	b	25mm	12.5mm	10°	12°	0mm	8.8mm
III	c	25mm	12.5mm	30°	20°	35mm	44mm

4.6.1 Grinding simulation of cylindrical end–mills

Three grinding processes are considered in simulating cylindrical end-mills grinding. The regions that can have contact with the end-mill rake face are highlighted with different color. The parameter u is chosen along the radial direction for wheels a and c, and along the wheel axis for wheel b. The end-mill dimensions and the grinding-wheel used for each process are listed in Table. 4.1.

Changing the point of the grinding-wheel in contact with the side cutting edge, $\mathbf{P}_{\mathrm{W}}(u, v)$, will directly affect the core radius of the ground end-mill. The deviation errors of the ground end-mill cores in comparing with the required cores are represented as a contour plot in Fig. 4.11.

The plot shows that the cores radii are altered by both u and v parameters. Thus, selecting a proper point, $\mathbf{P}_{\mathrm{W}}(u, v)$, is very essential in order to obtain end-mill cores with accurate geometries as shown in Fig. 4.12, Fig. 4.13 and Fig. 4.14 for processes I, II and III, respectively, where the ground flute surface is tangent to

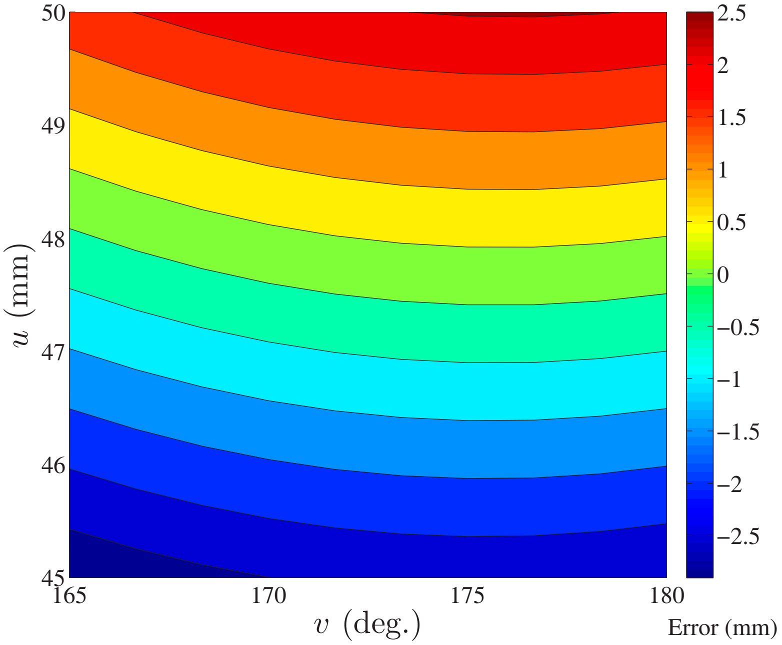

(a) Process I

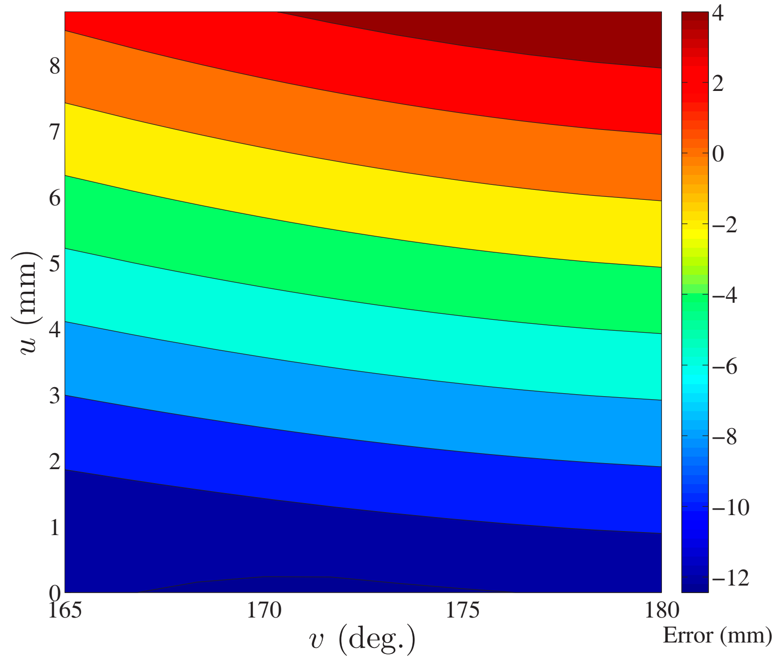

(b) Process II

Figure 4.11: Contour plots for the core deviation errors of cylindrical end-mills.

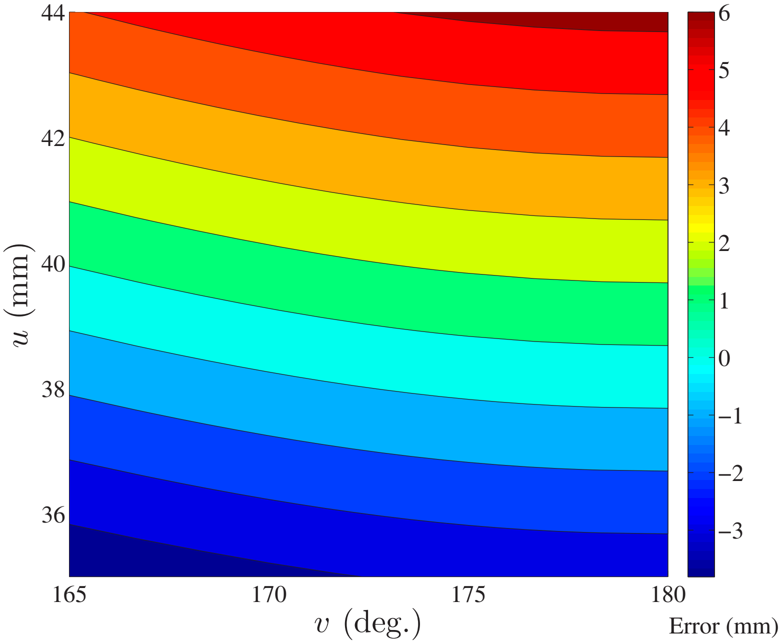

(c) Process III

Figure 4.11: Contour plots for the core deviation errors of cylindrical end-mills.

Table 4.2: Describtion of tapered end-mill grinding processes.

Grinding Process	Grinding wheel	End-mill	Helical angle (ψ)	Normal rake angle (α_{n})	u_L (mm)	u_U (mm)
IV	d	Fig. 4.15a	20^{o}	10^{o}	30	45
V	e	Fig. 4.15b	30^{o}	6^{o}	0	14.4
VI	c	Fig. 4.15c	10^{o}	12^{o}	35	50

the end-mill core and has an exact side cutting edge. The normal rake angle is also accurate and constant along the side cutting edge.

4.6.2 Grinding simulation of tapered end–mills

Grinding simulation is also conducted for three tapered flat end-mills having different geometries as shown in Fig. 4.15, where all dimensions are in millimeters. The end-mills are ground using different grinding-wheels. The details of the grinding processes are listed in Table 4.2.

As the core has a cone shape, its radius will increase when moving along the end-mill axis, the grinding-wheel is required to move far from the end-mill axis in order to account for the increase. Hence, the point on the grinding-wheel in contact with the cutting edge, $\mathbf{P}_{\mathrm{W}}(u, v)$, is varying. In order to simplify the problem, v is assumed (for now) constant during grinding and is assigned a value of 170^{o}. u is

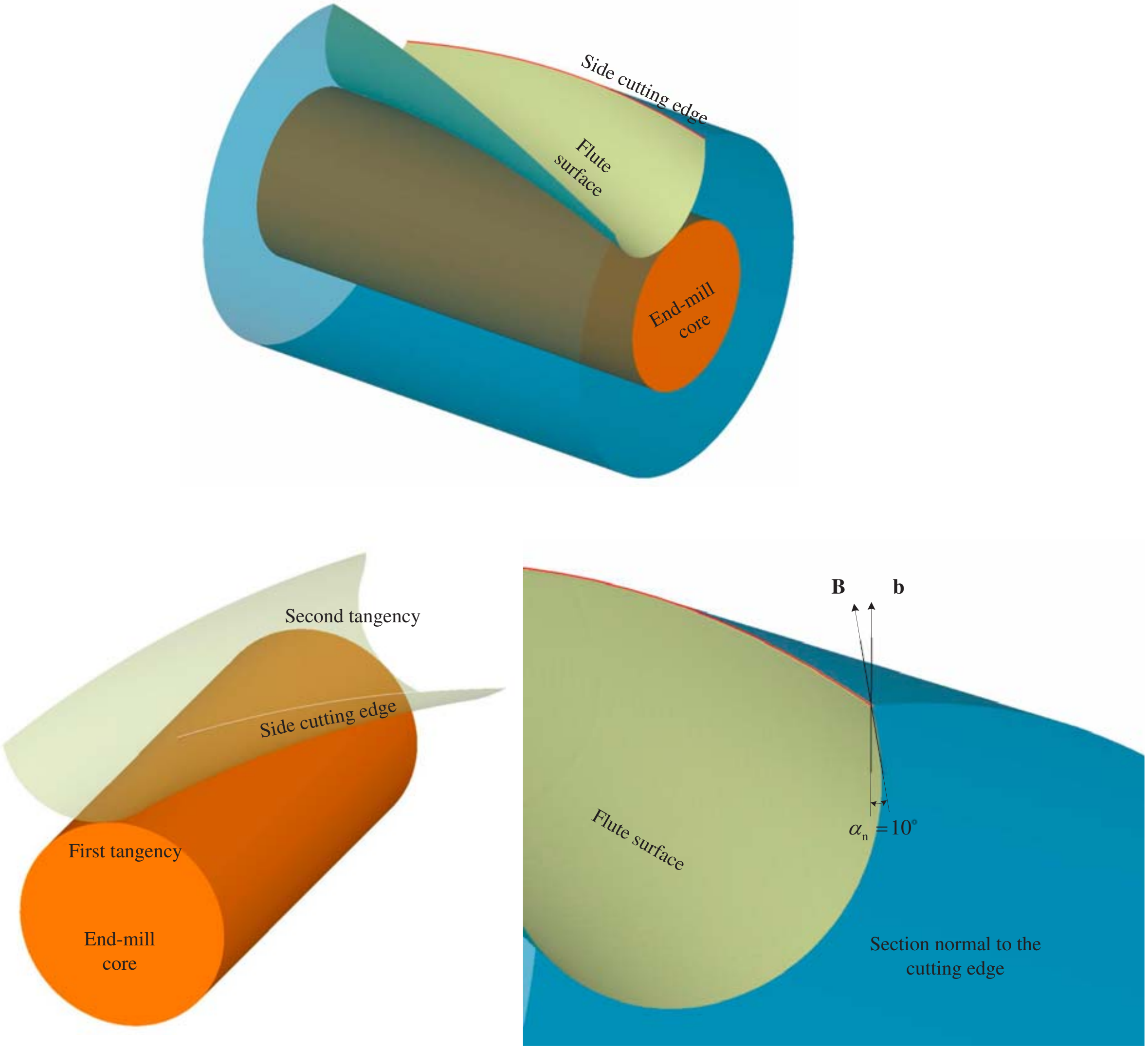

Figure 4.12: Cylindrical flat end-mill ground using grinding process I.

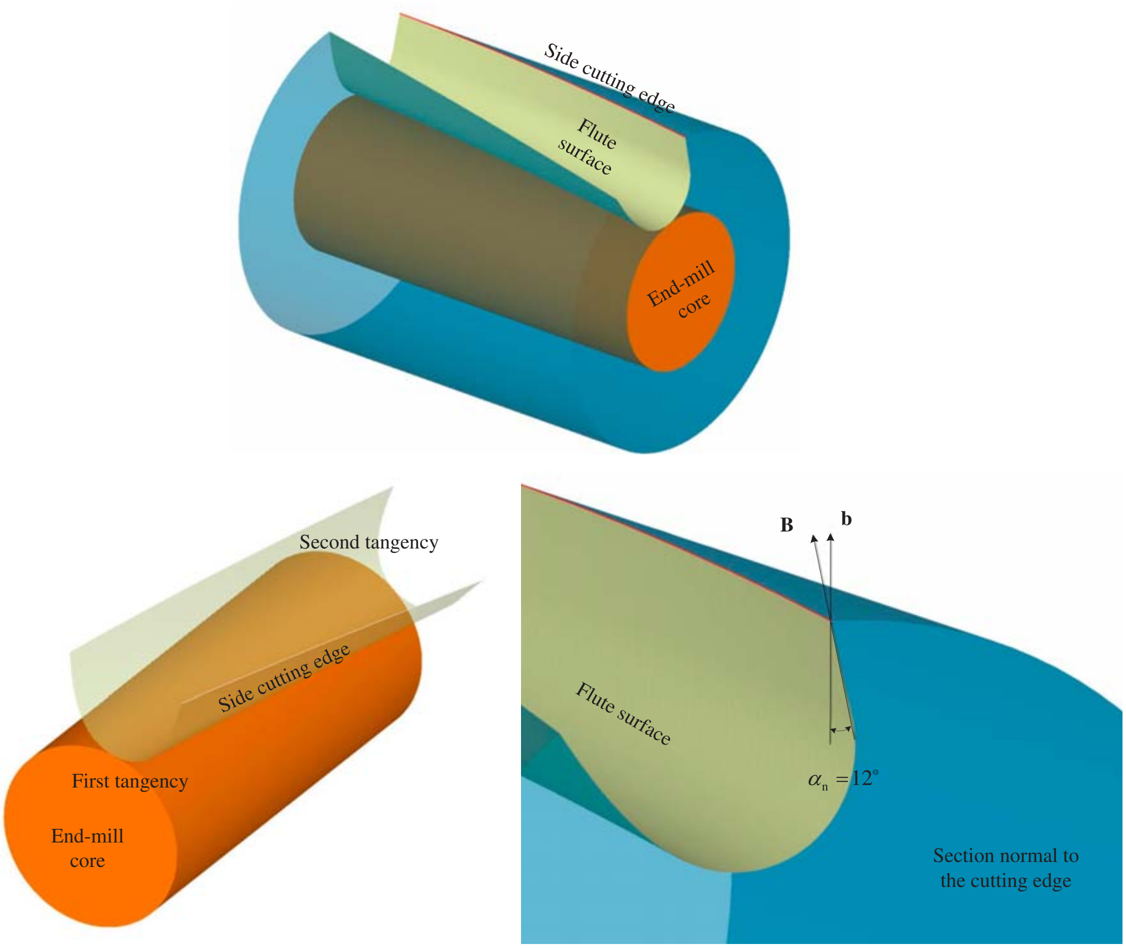

Figure 4.13: Cylindrical flat end-mill ground using grinding process II.

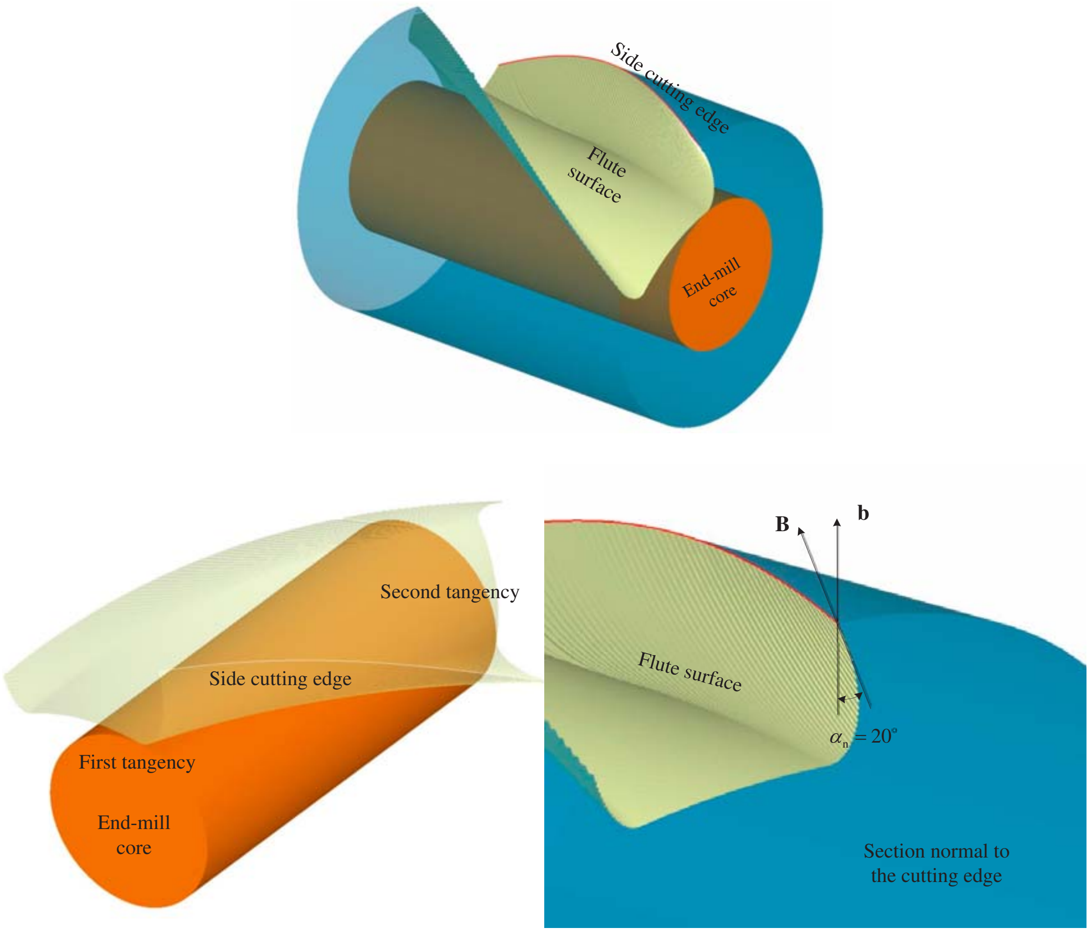

Figure 4.14: Cylindrical flat end-mill ground using grinding process III.

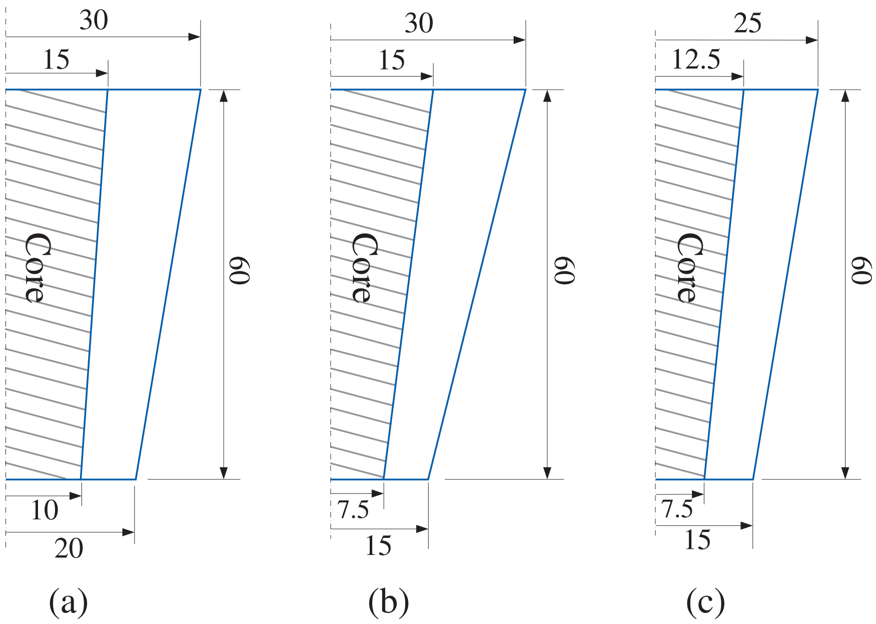

Figure 4.15: Geometries of tapered end-mills ground using the proposed approach.

assumed to vary linearly along the end-mill axis, that is

$$u = u_1 + (u_2 - u_1) l_n \tag{4.27}$$

where l_n is the normalized length along the end-mill axis, and u_1 and u_2 are the values that locate the contact point on the grinding-wheel when it is at the beginning and at the end of the cutting edge, respectively. u_1 and u_2 values will directly affect the core shape of the ground end-mill. The deviation errors between the conical cores of the ground end-mills and the designed conical cores (Fig. 4.16) are used to select the proper values for u_1 and u_2. These values are then used to conduct the grinding simulation as shown in Fig. 4.17, Fig. 4.18 and Fig. 4.19 for the grinding processes IV, V and VI, respectively.

It is obvious from the figures that the approach proposed grinds the end-mills with accurate side cutting edges while ensuring exact normal rake angles. The conical

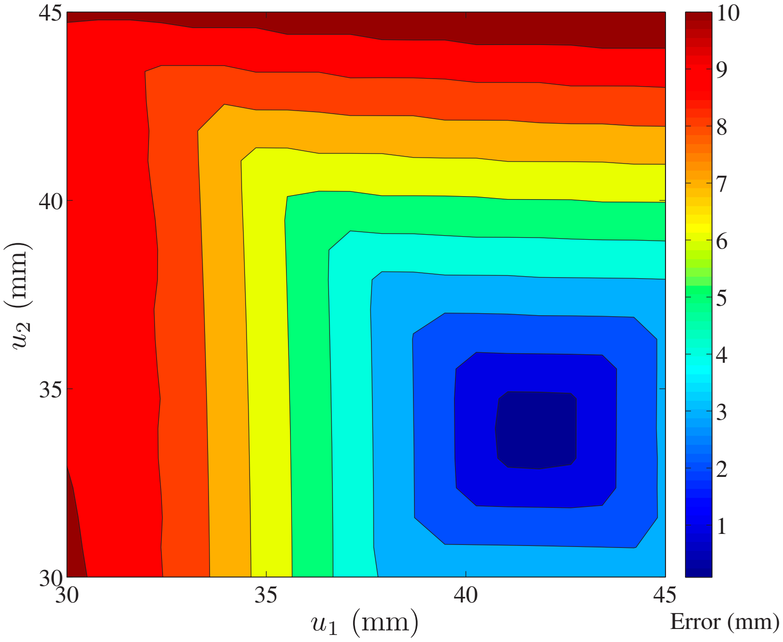

(a) Process IV

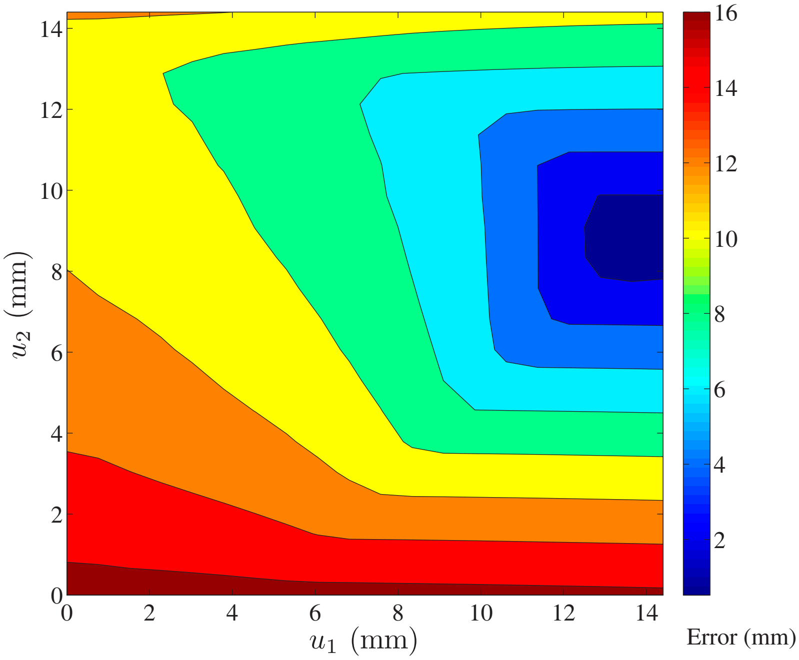

(b) Process V

Figure 4.16: Contour plots for the core deviation errors of tapered end-mill.

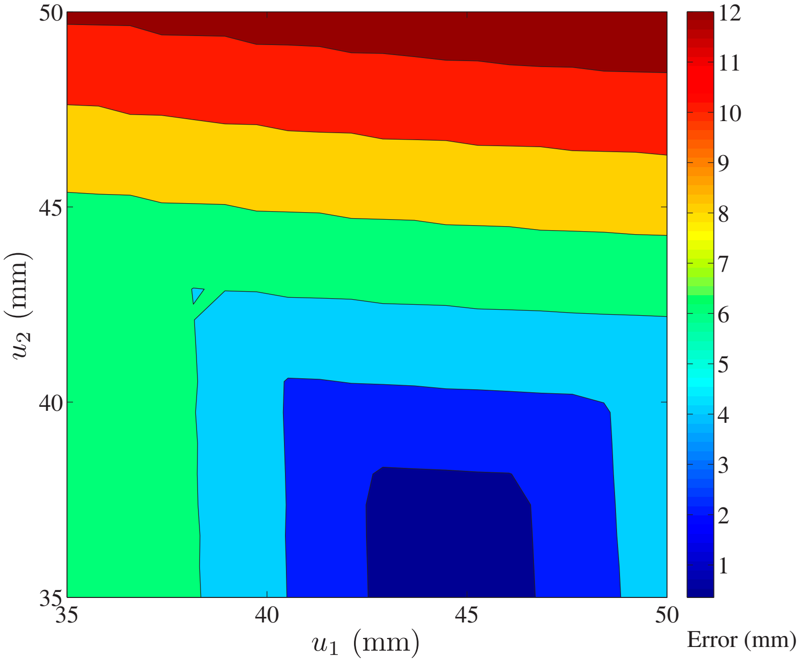

(c) Process VI

Figure 4.16: Contour plots for the core deviation errors of tapered end-mill.

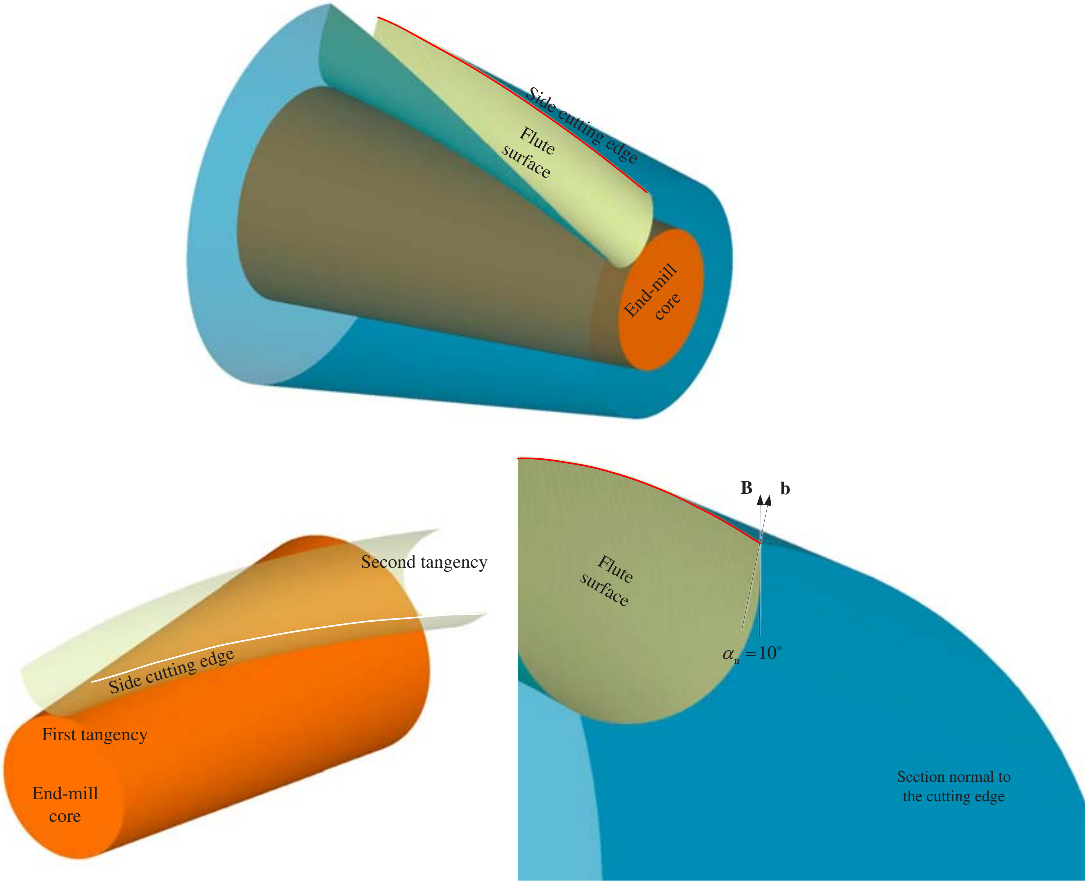

Figure 4.17: Tapered end-mill ground using grinding process IV.

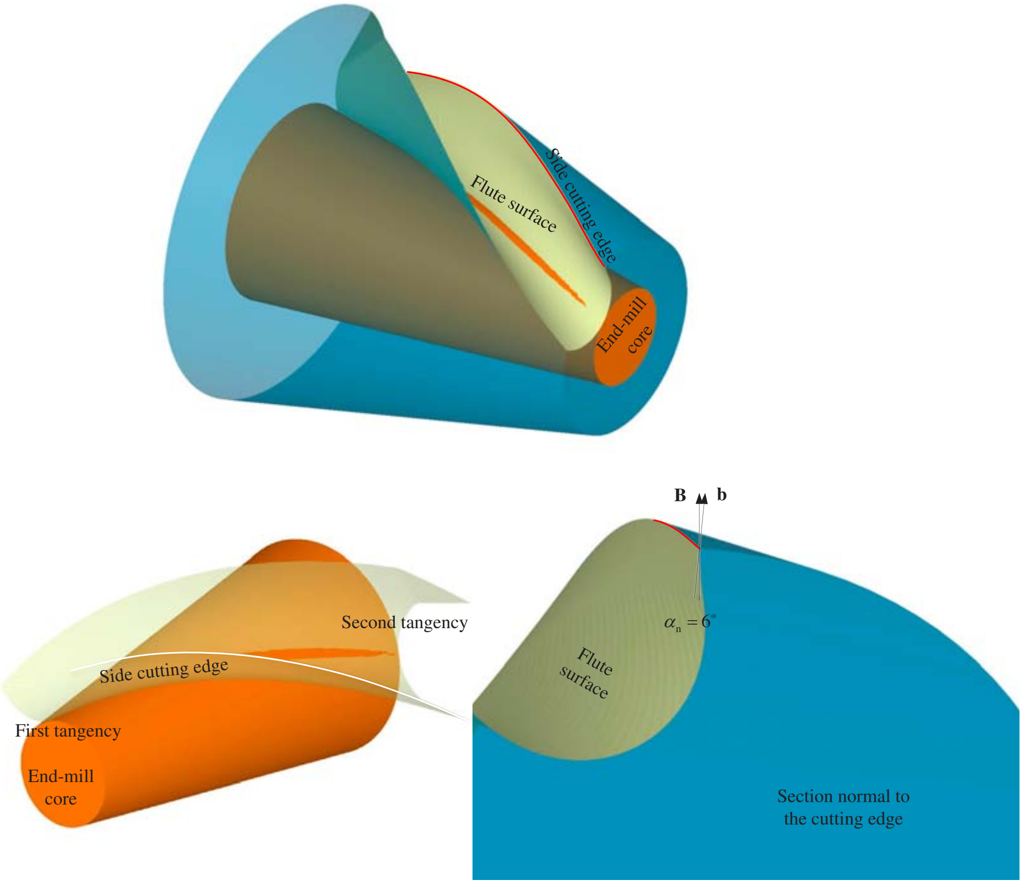

Figure 4.18: Tapered end-mill ground using grinding process V.

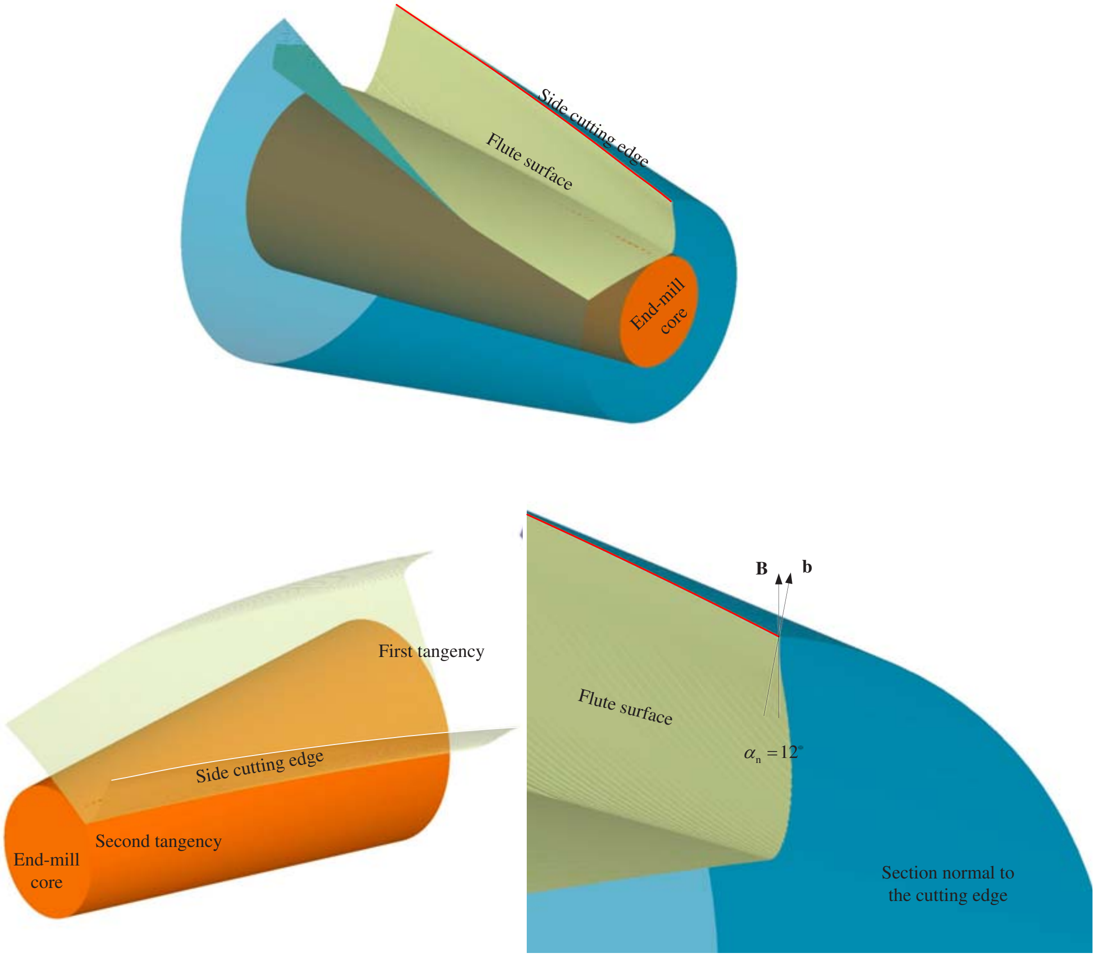

Figure 4.19: Tapered end-mill ground using grinding process VI.

cores can also be controlled by varying u_1 and u_2 in order to obtain accurate ones.

4.7 Conclusions

The five-axis rake face grinding process introduced in this chapter ensures constant normal rake angles on the rake faces along the side cutting edges. The wheel locations and orientations along the wheel path were derived and shown that they are affected by the selection of the wheel point in contact with the cutting edge. The wheel point in contact with the cutting edge can be controlled to produce end-mills with accurate conical cores. Beside the wheel point parameters (u and v), the wheel geometric parameters affect the final shape of the tool flutes. These parameters will be explored to pave the way for wheel path and wheel shape optimizations as will be discussed in the proceeding chapter.

Chapter 5

An Optimal Approach to 5–Axis End –Mill Flutes Grinding

5.1 Introduction

To achieve better tool dynamics for more accurate cutting, and to produce an end-mill with longer tool life, the produced end-mill should be an accurate copy of the designed model. This chapter establishes an optimization algorithm to grind the end-mills flutes in close matching to the designed ones by introducing a novel, yet simple, grinding-wheel , consisting of lines and circular arcs, that moves along the side cutting edge in 5-axis machining to produce accurate flutes and keep constant normal rake angle along the side cutting edge.

5.2 Parametric Representation of the Grinding–Wheel of Simple Geometry

The shape proposed for the grinding-wheel is represented as (Fig. 5.1)

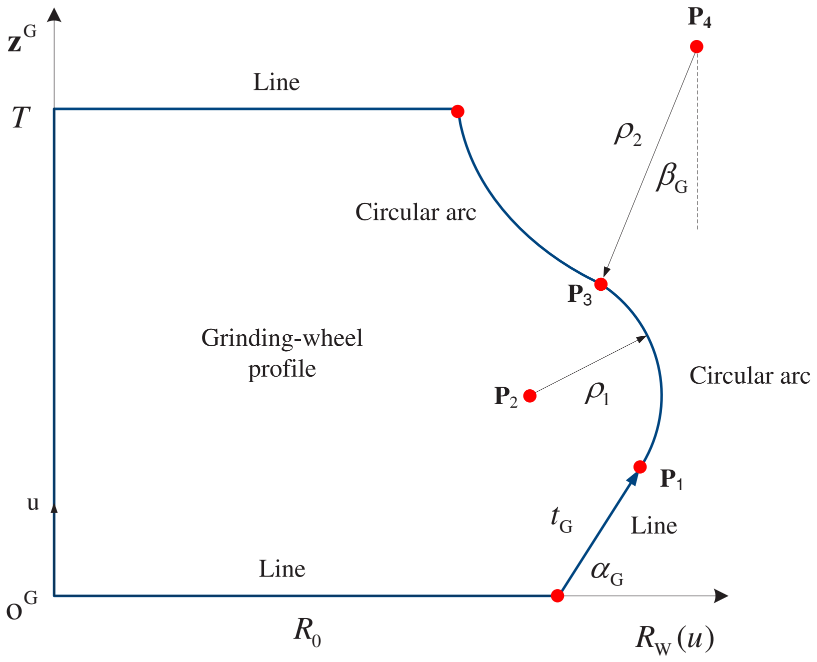

Figure 5.1: The revolving shape of the grinding-wheel.

$$\mathbf{S}_W(u,v) = \begin{bmatrix} R_W(u)\cdot\cos v & R_W(u)\cdot\sin v & u & 1 \end{bmatrix}^{\mathrm{T}} \tag{5.1}$$

where $0 \leq v \leq 2\pi$, and

$$R_W(u) = \begin{cases} R_0 + \frac{u}{\tan\alpha_G} & 0 \leq u \leq t_G\cdot\sin\alpha_G \\ x_{G2} + \sqrt{{\rho_1}^2 - (u - z_{G2})^2} & t_G\cdot\sin\alpha_G \leq u \leq z_G \\ x_{G4} - \sqrt{{\rho_2}^2 - (u - z_{G4})^2} & z_{G3} \leq u \leq T \end{cases} \tag{5.2}$$

and $P_i = \begin{bmatrix} x_{Gi} \\ y_{Gi} \\ z_{Gi} \end{bmatrix}$ for $i = \{1, ..., 4\}$, where $P_1 = \begin{bmatrix} R_0 + t_G\cdot\cos\alpha_G \\ 0 \\ t_G\cdot\sin\alpha_G \end{bmatrix}$, $P_2 = P_1 + \begin{bmatrix} -\rho_1\cdot\sin\alpha_G \\ 0 \\ \rho_1\cdot\cos\alpha_G \end{bmatrix}$, $P_3 = P_2 + \begin{bmatrix} \rho_1\cdot\sin\beta_G \\ 0 \\ \rho_1\cdot\cos\beta_G \end{bmatrix}$ and $P_4 = P_2 + \begin{bmatrix} (\rho_1+\rho_2)\cdot\sin\beta_G \\ 0 \\ (\rho_1+\rho_2)\cdot\cos\beta_G \end{bmatrix}$.

5.3 Five–Axis Grinding of End–Mill Flutes

In order to conduct accurate flute grinding, the flute is required to be modeled accurately and efficiently; for tapered end-mills, flutes are often designed with their solid models built using commercial CAD software, thus, they should be ground within the specified tolerance in production. Technically, the model of the tapered end-mill flutes is more complicated than that of the cylindrical end-mills. In modeling a flute of a cylindrical end-mill, the cross-sectional profile of the flute is swept along a helical side cutting edge. However, a flute of a tapered end-mill cannot be modeled in the same way; on the contrary, it is much more difficult to model. Basically, all of the flute profiles of a tapered end-mill should include the rake face with the prescribed rake angle and should be tangent to the core of the tool; but they are not the same in shape. Since only one grinding-wheel is used to machine the flute for high efficiency, the flute profiles are determined by the grinding-wheel. Therefore, a tapered end-mill flute can be modeled in the following way.

First, the flute profile at one end of the tapered end-mill is designed based on the requirements of high performance cutting. Second, according to an approach to programming for 5-axis flute grinding, the grinding-wheel orientation is determined. Then, the grinding-wheel profile with line segments and circular arcs is optimized so that the given flute profile is ensured in machining.

Compared to the aforesaid 2-axis grinding machines, the 5-axis grinding machines are more flexible in changing the orientation of the grinding-wheel with regard

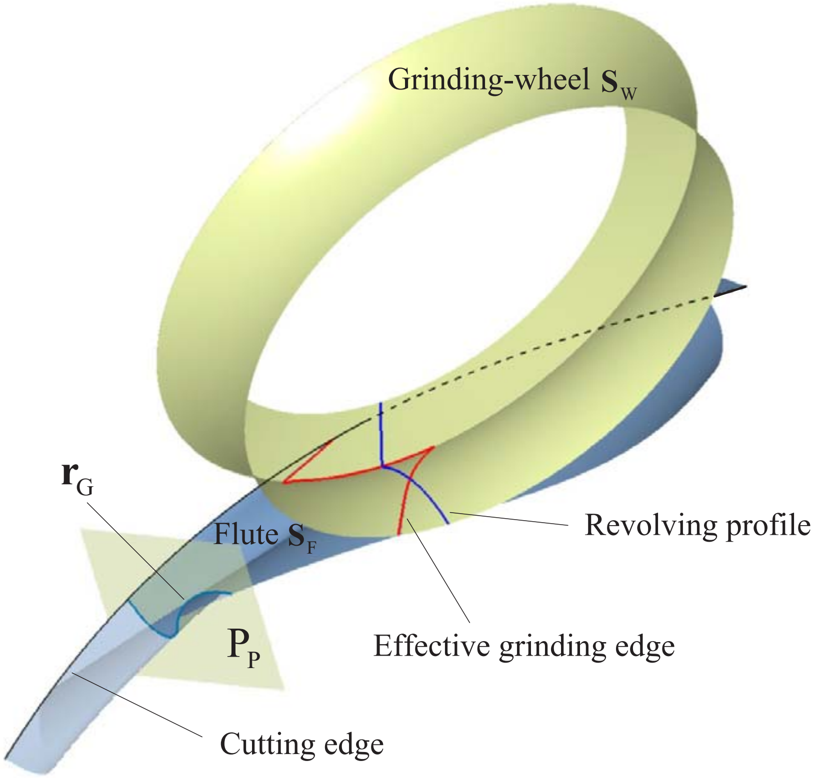

Figure 5.2: Cross-sectional profile of the ground flute

to the workpiece of the end-mill. With this advanced function, these machines can grind the flutes including the rake faces with their prescribed normal rake angles. Hence, it is always required that, at any moment of the machining process, the grinding-wheel is tangent to the side cutting edge at a point and the rake face at this point. Therefore, the same approach proposed in the previous chapter can be used to derive the equations of the grinding-wheel path (see the appendix) and the grinding-wheel swept envelope $\mathbf{S}_{\mathrm{F}}$.

The cross-sectional profile of the end-mill flute surface $\mathbf{r}_{\mathrm{G}}$ at any plane P_{P} perpendicular to the end-mill axis ($z^{\mathrm{T}} = k$) is obtained by first solving the equation

$$z_{\mathrm{F}}^{\mathrm{T}}(u,t) = k \tag{5.3}$$

in order to establish a relationship between u and t (Fig. 5.2). Here, $z^{\mathrm{T}}_{\mathrm{F}}$ is the z^{T}-component of $\mathbf{S}_{\mathrm{F}}$ as obtained early in Eq.(4.25). Then, $\mathbf{r}_{\mathrm{G}}$ will be simply represented as

$$\mathbf{r}_{\mathrm{G}} = \mathbf{S}_{\mathrm{F}}(u) \tag{5.4}$$

Since the grinding-wheel locations and orientations are obtained for any point $\mathbf{P}$ on the side cutting edge in terms of θ_{C}, establishing a relationship between θ_{C} and the time t is necessary to represent the wheel locations and orientations for real time machining. This relationship can be expressed as

$$\left\| \frac{d\mathbf{C}^{\mathrm{T}}_{\mathrm{C}}}{d\theta_{\mathrm{C}}} \right\| = \left\| \frac{d\mathbf{C}^{\mathrm{T}}_{\mathrm{C}}}{dt} \right\| \cdot \frac{dt}{d\theta_{\mathrm{C}}} \tag{5.5}$$

where $\left\| \frac{d\mathbf{C}^{\mathrm{T}}_{\mathrm{C}}}{dt} \right\|$ is the feed f. Then

$$\int \left\| \frac{d\mathbf{C}^{\mathrm{T}}_{\mathrm{C}}}{d\theta_{\mathrm{C}}} \right\| \cdot d\theta_{\mathrm{C}} = \int f \cdot dt \tag{5.6}$$

For example, this relationship can be expressed for cylindrical flat-end mills of radius r_{T} as

$$\theta_{\mathrm{C}} = \frac{f}{\sqrt{r_{\mathrm{T}} + \left(\frac{r_{\mathrm{T}}}{\tan\psi}\right)^2}} \cdot t \tag{5.7}$$

and for tapered flat end-mills as

$$z_{\mathrm{C}} = f \cdot \cos\psi \cdot \cos\varphi_{\mathrm{T}} \cdot t \tag{5.8}$$

where z_{C} is related to θ_{C} as discussed early in chapter 3.

And now, it is worth to emphasize on the fact that the wheel path will be different for different selection of $\mathbf{P}_{\mathrm{W}}$. This means that the shape of the ground flute is changed by varying the values of u and v; the thing that gives more flexibility to control the ground flute toward better end-mill cutting dynamics and life.

5.4 Wheel Path and Wheel Profile Optimization

The main objective of the optimization method is to grind the end-mills with precise flutes while keeping constant normal rake angle. In other words, to minimize the maximum deviation between the ground flute cross-sectional profile $\mathbf{r}_{\mathrm{G}}$ and the designed one, $\mathbf{F}(l)$. Since $\mathbf{F}(l)$ is commonly described in terms of the radial angles (rake, primary and secondary), a relationship should be established to connect these radial angles to their corresponding normal angles. Then the parameters affecting $\mathbf{r}_{\mathrm{G}}$ will be analyzed. These parameters will then be optimized using global optimum determination by linking and interchanging kindred evaluators (GODLIKE) to obtain optimal wheel shapes grinding precise end-mill flutes along optimal paths.

5.4.1 Normal–radial rake angles relationship

As the end-mill is commonly described via the cross-sectional profile of the flute surface; the normal rake angle, the primary normal relief angle and the secondary normal relief angle are all derived from their corresponding radial angles in the follow.

The radial rake angle at point $\mathbf{P}$ on the cutting edge is the angle bounded between vector $\mathbf{A}_{\theta_{\mathrm{C}}}$, resulted from projecting a vector connecting point $\mathbf{P}$ with the origin on the $\mathbf{x}^{\mathrm{T}}\mathbf{y}^{\mathrm{T}}$ plane, and $\mathbf{A}_{\mathrm{R}}$ as shown in Fig. 5.3.

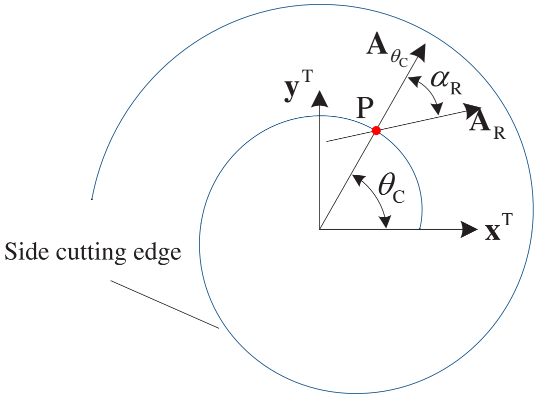

Figure 5.3: Radial rake angle.

Mathematically, $\mathbf{A}_{\theta_\mathrm{C}}$ can be expressed as

$$\mathbf{A}_{\theta_\mathrm{C}} = \begin{bmatrix} \cos\theta_\mathrm{C} \\ \sin\theta_\mathrm{C} \\ 0 \end{bmatrix} \tag{5.9}$$

so

$$\mathbf{A}_\mathrm{R} = \begin{bmatrix} \cos\alpha_\mathrm{R}\cos\theta_\mathrm{C} + \sin\alpha_\mathrm{R}\sin\theta_\mathrm{C} \\ \cos\alpha_\mathrm{R}\sin\theta_\mathrm{C} - \cos\theta_\mathrm{C}\sin\alpha_\mathrm{R} \\ 0 \end{bmatrix} \tag{5.10}$$

Since $\mathbf{A}_\mathrm{R}$ is located on the rake face, the following relationship is valid

$$\mathbf{A}_\mathrm{R} \cdot \mathbf{N} = 0 \tag{5.11}$$

where $\mathbf{N}$ is the rake face unit normal vector at point $\mathbf{P}$ as derived previously in Eq.(4.9). Simplifying Eq.(5.11) will reveal the normal-radial rake angles relationship. For cylindrical cutters the relationship is expressed as

$$\alpha_\mathrm{n} = \tan^{-1}(\tan\alpha_\mathrm{R}\cos\psi) \tag{5.12}$$

Table 5.1: Values of the wheel parameters for cylindrical end-mill grinding

R_0 (mm)	t_{G} (mm)	t_w (mm)	α_{G} (deg.)	β_{G} (deg.)	ρ_1 (mm)	ρ_2 (mm)
20	15	30	15	50	2	35

and for tapered cutters as

$$\alpha_{\mathrm{n}} = \tan^{-1}\left(\frac{\cos\psi\sin\alpha_{\mathrm{R}} + \cos\alpha_{\mathrm{R}}\sin\psi\sin\varphi_{\mathrm{T}}}{\cos\alpha_{\mathrm{R}}\cos\varphi_{\mathrm{T}}}\right) \tag{5.13}$$

The normal-radial rake angles relationship derived can be used directly to represent the relationships between the normal and the radial relief angles.

5.4.2 Optimization problem description

The shape of $\mathbf{r}_{\mathrm{G}}$ is controlled by both the wheel shape and the wheel path. The wheel shape can be controlled simply by the geometric parameters of the wheel profile. Mainly, these are $R_0, \alpha_{\mathrm{G}}, \beta_{\mathrm{G}}, \rho_1$ and ρ_2. The wheel path is controlled by changing the location of point $\mathbf{P}_{\mathrm{W}}$ on the grinding-wheel surface (i.e. u and v).

Consider grinding a cylindrical flat-end mill by keeping constant normal rake angle of 10^{o} and values assigned to the wheel parameters as listed in Table 5.1. Also consider the contact point $\mathbf{P}_{\mathrm{W}}$ is defined by assuming $u = 0.5$mm and $v = 175^{\mathrm{o}}$. By changing only one at a time, the effect of the parameters on the flute shape can be represented as shown in Fig. 5.4.

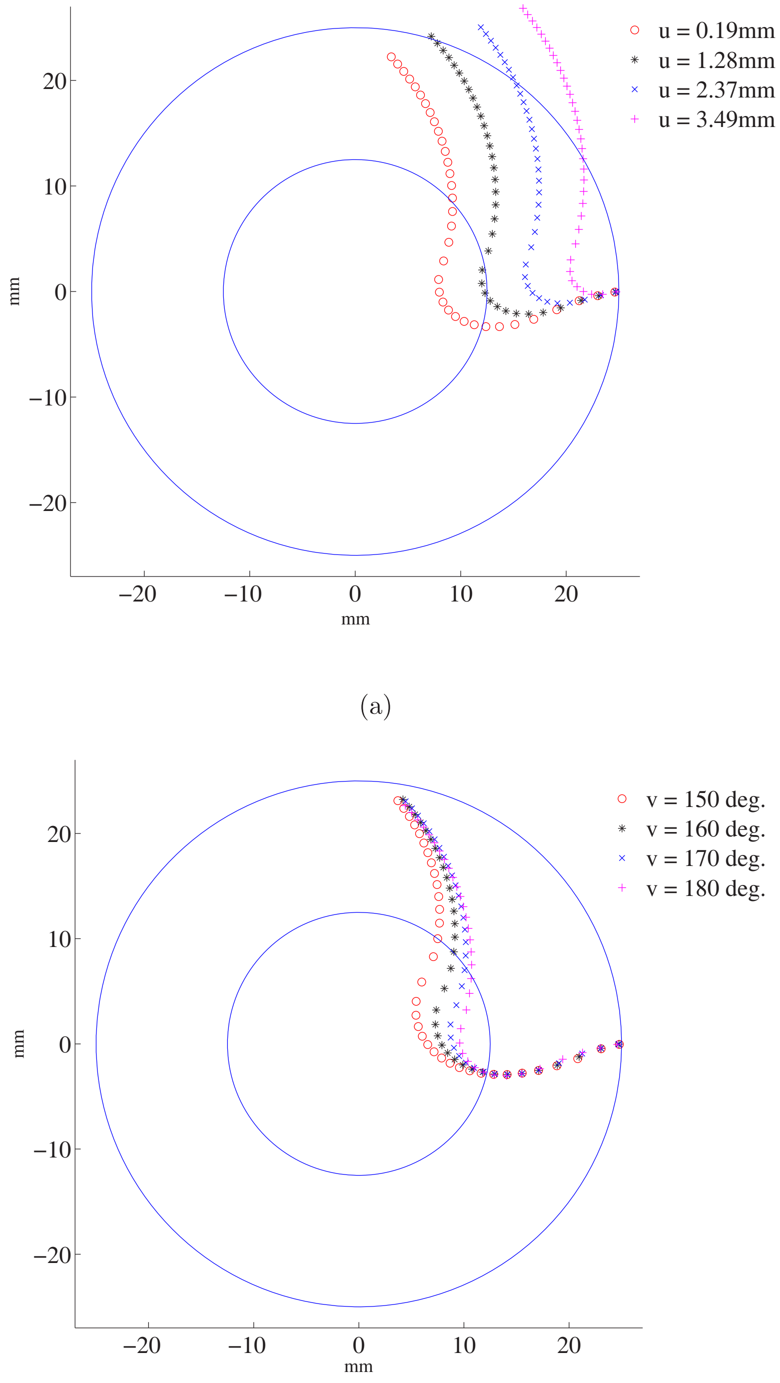

(a)

(b)

Figure 5.4: Effect of the wheel shape and the wheel path parameters on the flute shape.

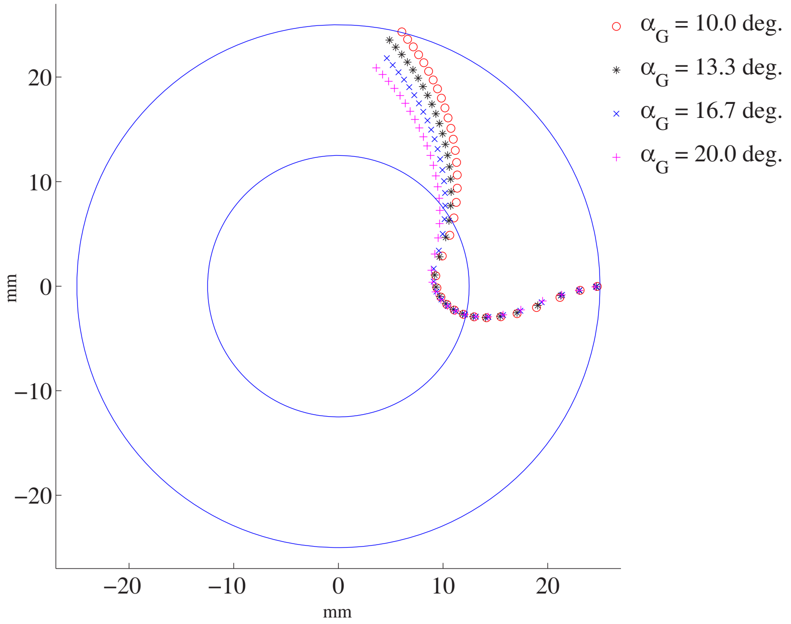

(c)

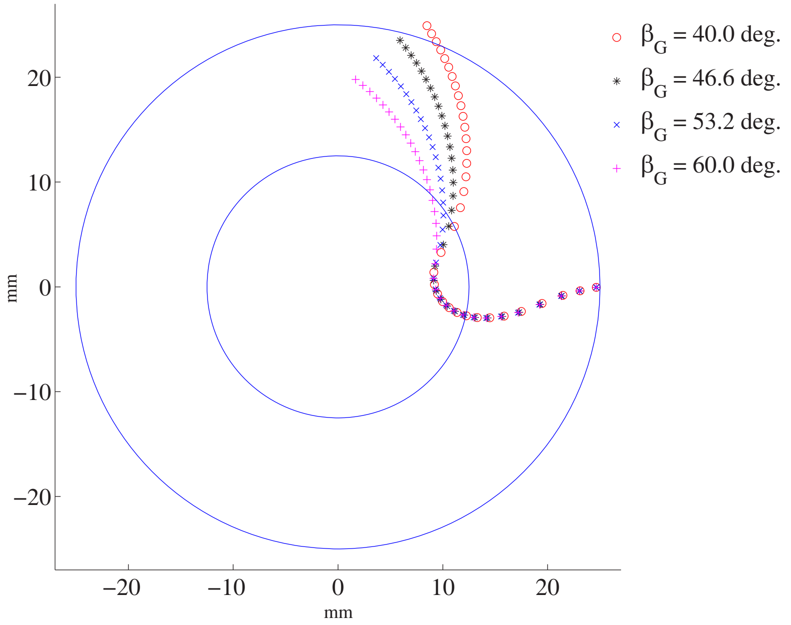

(d)

Figure 5.4: Effect of the wheel shape and the wheel path parameters on the flute shape.

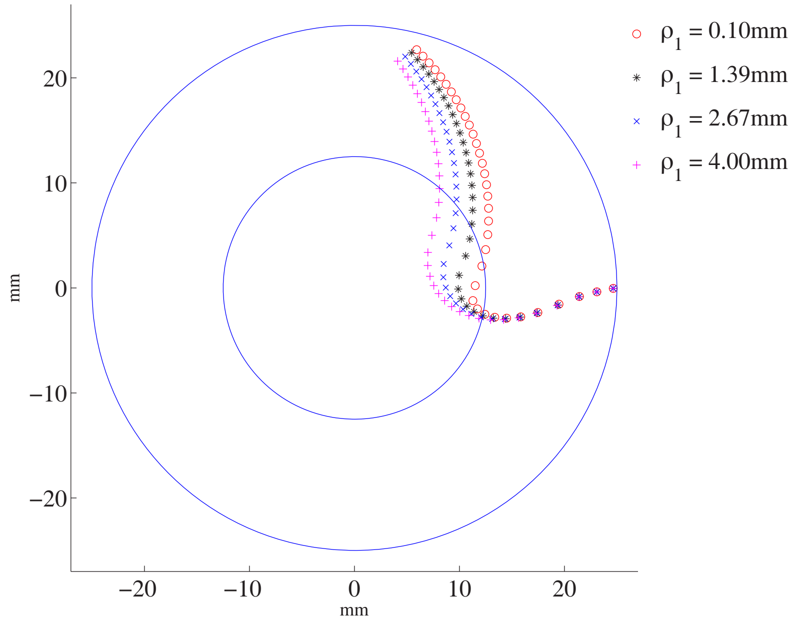

(e)

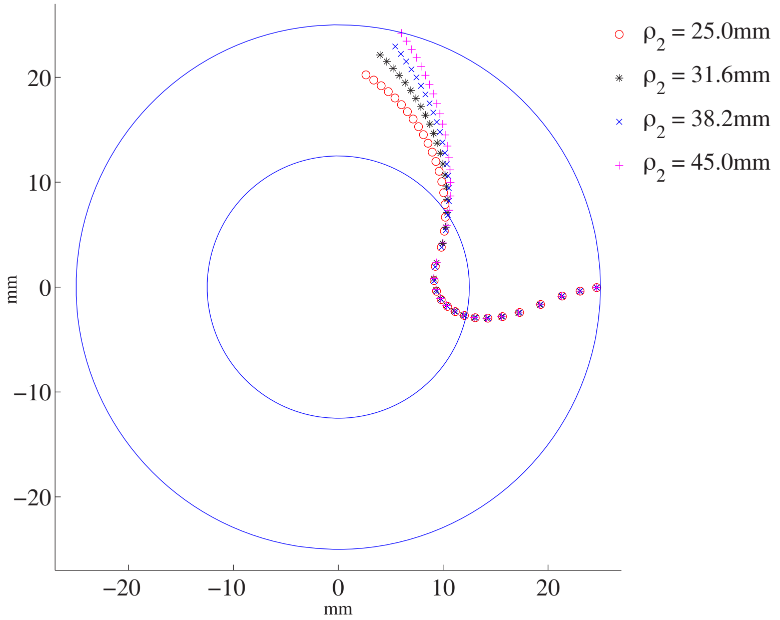

(f)

Figure 5.4: Effect of the wheel shape and the wheel path parameters on the flute shape.

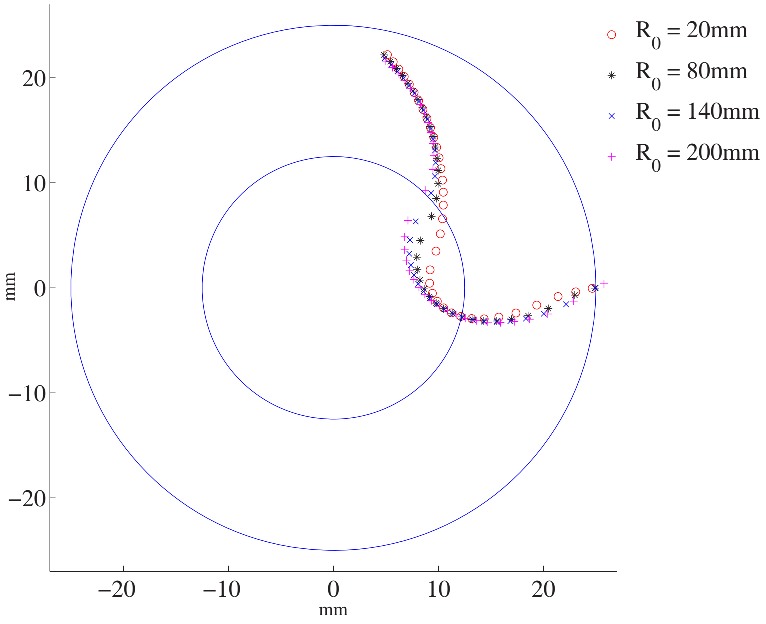

(g)

Figure 5.4: Effect of the wheel shape and the wheel path parameters on the flute shape.

Now, the optimization problem can be described mathematically for the cylindrical flat end-mills as

$$\min_{x \in R^7} \max \|(\mathbf{F}(l) - \mathbf{r}_{\mathrm{G}})\| \tag{5.14}$$

subject to

$$x_L \leq x \leq x_U$$

where $x = \{R_0, \alpha_{\mathrm{G}}, \beta_{\mathrm{G}}, \rho_1, \rho_2, u, v\}$. Here, x_L and x_U are the lower and the upper bounds of x, respectively.

As described in the previous sections, since the flute cross-sectional profile of the tapered end-mill $\mathbf{F}$(l) is changing along the end-mill axis, more complexities are added to the problem in order to ensure exact end-mill flute shapes and conical cores. This can be solved by considering more than one flute cross-sectional profile along the end-mill axis. The objective function will then be to minimize the maximum deviation existed in all cross-sections. Mathematically this can be expressed as

$$\min_{x \in R} \max \left\{ \max \left\| \left(\mathbf{F}(l)^i - \mathbf{r}_{\mathrm{G}}{}^i \right) \right\| \right\}, \quad i = 1, ..., m \tag{5.15}$$

subject to

$$x_L \leq x \leq x_U$$

where m is the number of considered flute cross-sectional profiles along the end-mill axis.

Thus, as the grinding-wheel is moving along the side cutting edge, it is required to (1) move far from the end-mill axis in order to account for the core variation and (2) obtain close matching between $\mathbf{F}(l)$ and $\mathbf{r}_{\mathrm{G}}$ in the considered end-mill cross-sections. In other words, point $\mathbf{P}_{\mathrm{W}}$ on the grinding-wheel contacting the side cutting edge should be changed; this means that u and v should also be changed. Assuming that their variation along the side cutting edge is linear. Then, they can be expressed as

$$\begin{aligned} u &= u_1 + (u_2 - u_1)l_n \\ v &= v_1 + (v_2 - v_1)l_n \end{aligned} \tag{5.16}$$

where (u_1, v_1) and (u_2, v_2) are the optimal values for (u, v) at the start and at the end of the side cutting edge, respectively, and l_n is the end-mill normalized length between the two cross-sections considered. Due to this flexibility of changing point $\mathbf{P}_{\mathrm{W}}$, close matching between the designed and the ground flutes is attainable for the tapered end-mills.

5.4.3 GODLIKE Algorithm

To efficiently solve the optimization problem in this work, a global optimization method, called the global optimum determination by linking and interchanging kindred evaluators (GODLIKE) is employed [55]. This method simultaneously uses the existing global optimization solvers, the genetic algorithm (GA), the differential evolution (DE), and the adaptive simulated annealing (ASA) to find the global optimum. The main purpose of employing different existing solvers is to increase the robustness of finding the global optimum solution and to decrease the chance of premature convergence to a local solution, which could diminish the time-consuming fine tune in each solver.

GODLIKE randomly separates the main population (Pop) of size ($Popsize$) into three sub-populations ($sub\_pop(i)$, $i = \{1, 2, 3\}$) with random sizes (Fig. 5.5). However, the size of each sub-population should not be less than the pre-specified value ($MinIndiv$). The sub-populations are then continuously updated by the optimization solvers until the convergence criteria takes place or the maximum iterations (t_i) corresponding to each algorithm are exceeded. The value of the maximum iterations corresponding to each solver is randomly generated for each generation. This value should not be less than a specified number of iterations ($ItersLb$) to avoid premature results, and the sum of all iterations $\sum_{i=1}^{3} t_i$ should not exceed a certain value ($ItersUb$) to force the individuals to interchange more often through the involved solvers. The sub-populations are then combined to form the main population for the next generation. This procedure is repeated until all algorithms are converged to the global solution or until the maximum function evaluations ($MaxFuneval$) or the maximum generations ($MaxIters$) are exceeded.

In other words, the GODLIKE optimization method simultaneously executes several conventional global optimization solvers for the same optimization problem; and it constantly shares the results of the solvers after each generation. A salient feature of the GODLIKE method is that the individuals of the solvers are interchanged after each generation in the optimization process, thus the initial values of the individuals for the new generation are well selected, based on the results of the iterations of the previous generation of the solvers. Although this method seems take longer time to converge to the optimum solution because several solvers are involved, this

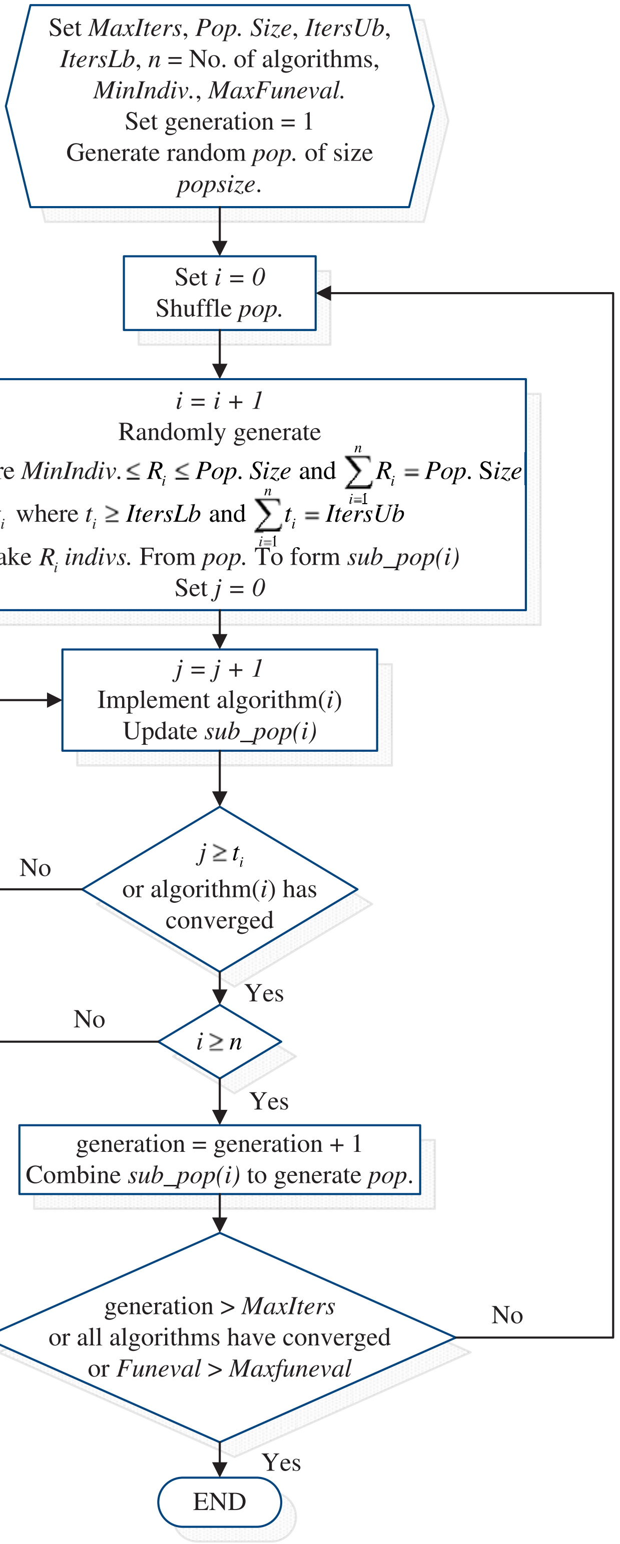

Figure 5.5: GODLIKE scheme flowchart.

method can effectively avoid invalid convergence to a local optimum and can remain efficient by using well selected initial values of the individuals. This method is applied to the optimization of the grinding-wheel profile and path, and the results are quite satisfactory.

5.5 Application

To validate this practical and optimal approach to CNC programming for 5-axis grinding of the prescribed flutes of the tapered end-mills and to demonstrate the advantages of this new approach over the current inverse method, two grinding examples of cylindrical and tapered end-mills flutes are simulated. Given prescribed flute profiles for the end-mills, the grinding-wheels profiles and the grinding-wheels paths are simultaneously optimized. The programming for the 5-axis flute grinding is conducted, and the grinding simulation is provided.

5.5.1 Five–axis grinding of cylindrical end-mill flutes

In the first example, a cylindrical end-mill with a flute profile is provided. Since cylindrical end-mills are special types of the tapered end-mills, it is easier to understand this new approach, if it is applied to a cylindrical end-mill. The parameter values of the flute profile and the tool are listed in Table 5.2. The flute profile is plotted in Fig. 5.6.

Based on the given flute profile, this new approach is applied on CNC pro-

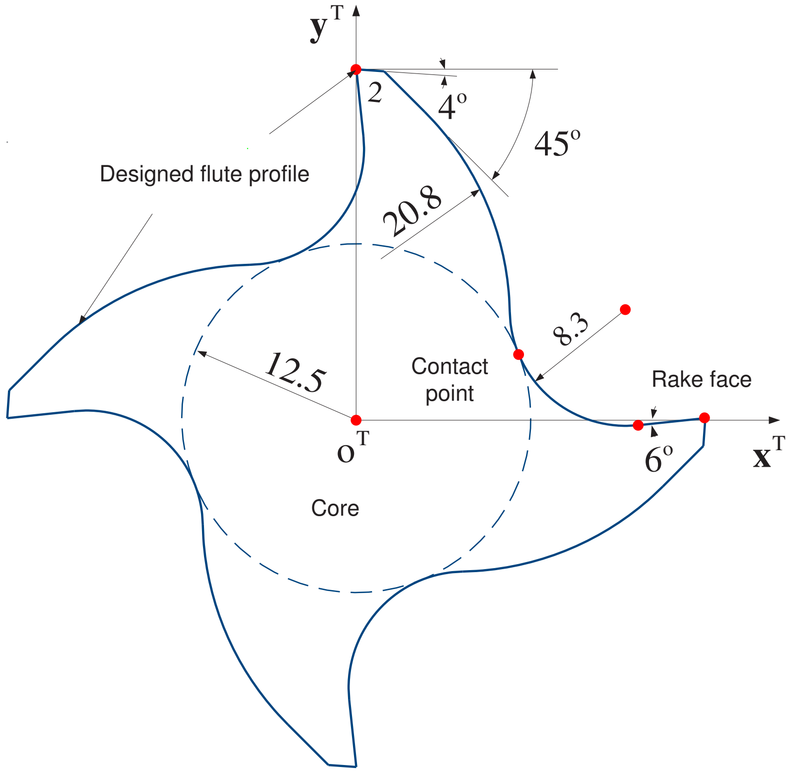

Figure 5.6: Plot of the designed flute profile of the cylindrical end-mill.

Table 5.2: The parameters values of the cylindrical end-mill.

Tool Radius (mm)	Core radius (mm)	Tool length (mm)	Helical angle (deg.)	Radial rake angle (deg.)
25	12.5	40	45	6
r_1 (mm)	r_2 (mm)	γ_P (deg.)	γ_S (deg.)	
8.3	20.8	4	45	

gramming for the 5-axis grinding of this flute. To machine the rake face with the specified rake angle, the orientation angles μ and η of the grinding-wheel are calculated as 33.07^o. and -30.83^o, respectively. The wheel location at the first point of the side cutting edge is (50.05mm, -31.24mm, -13.47mm) in the tool coordinate system. In the process of optimizing the grinding-wheel profile, the population size is 500, the function evaluation number and the maximum deviations between the designed flute profile and the machined flute profiles of GODLIKE, GA, ASA, and DE solvers are listed in Table 5.3. Using this special grinding-wheel to machine the flutes of the cylindrical end-mill in 5-axis grinding, the effective grinding edge and the machined flute profile can be computed. It is evident that the GODLIKE solver is more accurate and efficient in optimizing the grinding-wheel profile. For comparison, the machined flute profile and the designed flute profile are plotted in Fig. 5.7, and the machining error curve is plotted in Fig. 5.8. The maximum deviation between the profiles of the machined and the designed flutes is 0.32mm.

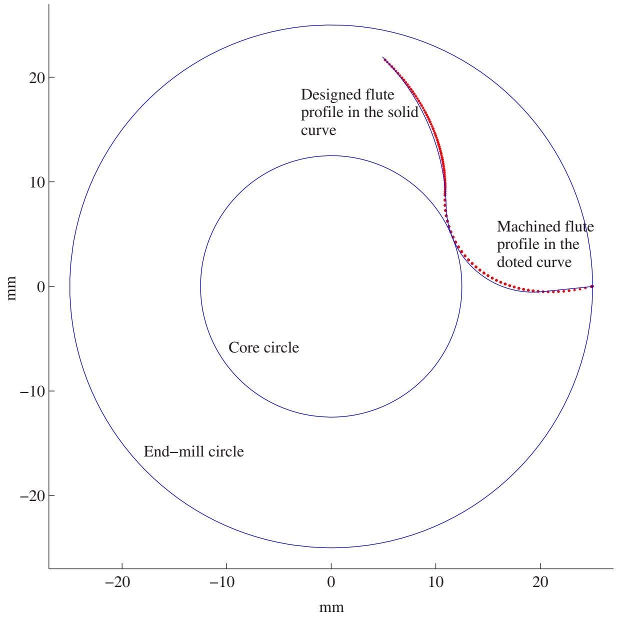

Figure 5.7: Designed vs. generated flute cross-sections.

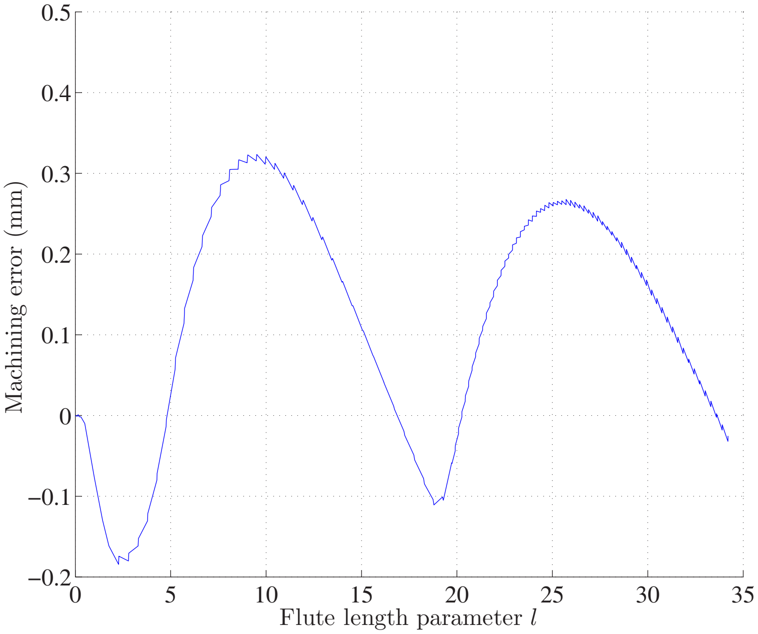

Figure 5.8: The deviation error of the generated flute cross-section from the designed one.

Table 5.3: Performance comparison of the GODLIKE solver and the other solvers.

Solver	GODLIKE	GA	ASA	DE
Function evaluations	29026	31001	97001	100460
Maximum deviation (mm)	0.3168	0.3869	0.4717	0.3251

To show the difference between this new approach and the aforesaid inverse method, the inverse method is applied to this example. The grinding-wheel profile generated using the inverse method is a free-form curve, which is plotted in Fig. 5.9a. So, it is difficult and expensive to dress and make the grinding-wheel. Using our approach, the grinding-wheel profile is optimized with simple geometric features, which is plotted in Fig. 5.9b. The values of the grinding-wheel profile parameters R_0, α_G , β_G, ρ_1 and ρ_2 are 31.34mm, 19.91^o, 64^o, 1.81mm and 428mm, respectively. Moreover, the flute machined with the optimized grinding-wheel is simulated and shown in Fig. 5.10.

5.5.2 Five–axis grinding of tapered end–mill flutes

The main advantage of this new approach, compared to the current inverse method, is that this approach can precisely grind the flutes of the tapered end-mills while the inverse method cannot. To demonstrate this advantage, the second example employs a tapered end-mill with its flute designed, and the CNC programming for the 5-axis grinding of the flute is generated using this approach. The tool parameter values are

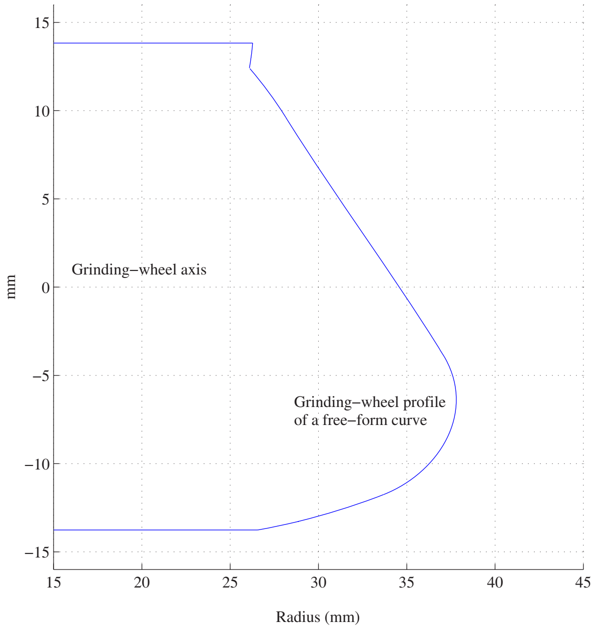

(a) The revolving profile of the inverse method grinding-wheel.

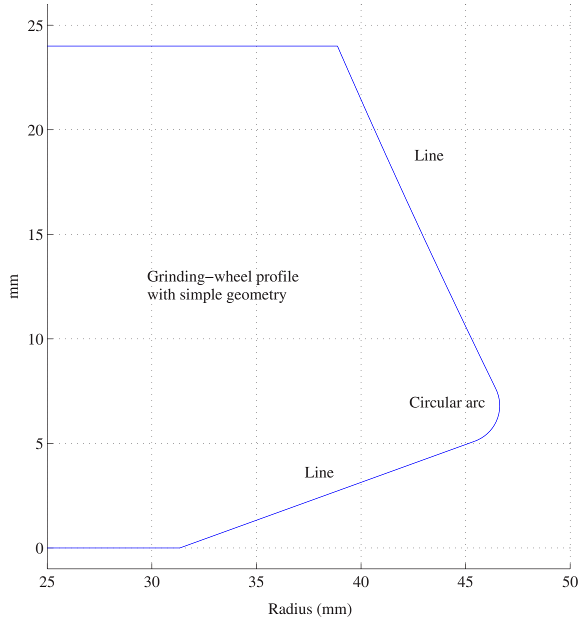

(b) The revolving profile of the optimized grinding-wheel.

Figure 5.9: The grinding-wheels used to grind the cylindrical end-mill.

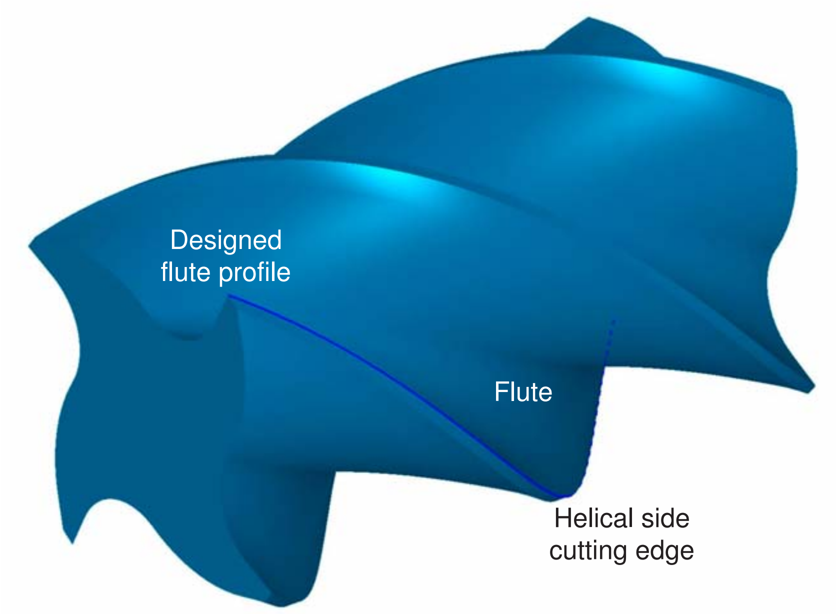

Figure 5.10: The ground end-mill having an exact side cutting edge.

listed in Table 5.4. The flute profile on the larger tool end is plotted in Fig. 5.11.

First, the aforementioned inverse method is used to determine the grinding-wheel profile based on the designed flute profile at the larger tool end. The calculated profile is a free-form curve plotted in Fig. 5.12. The flute is machined in 2-axis CNC grinding and is simulated in a computer system. The simulation model of the machined tapered end-mill is provided in Fig. 5.13. It is clear that the machined side cutting edge deviates from the designed one and the flute on the smaller tool end does not have any rake face.

Second, this new approach is employed for machining similar tapered end-mill. For grinding the rake face with the specified rake angle in the 5-axis flute, two cross-sectional profiles for the designed flute are considered; these are the smallest and the largest cross-sections. The designed parameters R_0, α_{G}, β_{G}, ρ_1, ρ_2, u_1, v_1, u_2 and

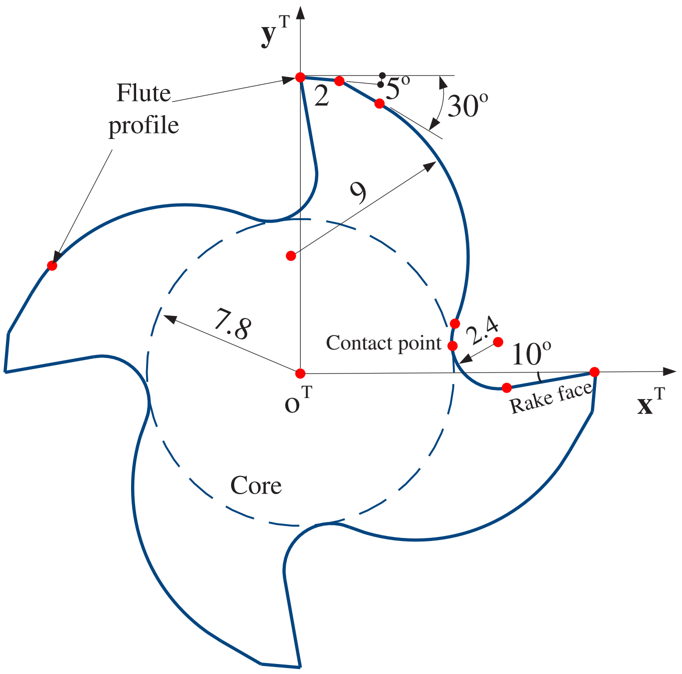

Figure 5.11: Design of the flute profile of the tapered end-mill on the large tool end.

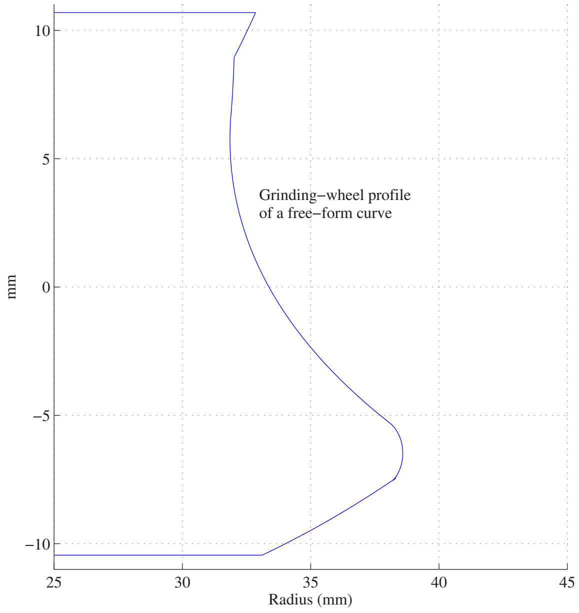

Figure 5.12: The grinding-wheel profile determined using the inverse method based on the designed flute profile at the larger tool end.

Table 5.4: The parameters values of the tapered end-mill.

Helical angle (deg.)	Radial rake angle (deg.)	Tool tapered angle (deg.)	Tool radius at the larger end (deg.)	Core radius at the larger end (deg.)
20	10	10	15	7.8
Tool length (mm)	r_1 (mm)	r_2 (mm)	γ_P (deg.)	γ_S (deg.)
40	2.4	9	5	30

v_2 are obtained from the optimization solver as 37.75mm, 19.60°, 49.11°, 1.22mm, 20.10mm, 3.00mm, 179.48°, 1.06mm and 165.11° , respectively. The optimization solver used a population of 500 individuals to minimize the maximum deviation that results from those cross-sections. The outputs obtained from the solver are an optimal grinding-wheel profile as shown in Fig. 5.14, and an optimal grinding-wheel path as described in the follow.

For complete flute machining, point $\mathbf{P}_{\mathrm{w}}(u, v)$ is calculated along the side cutting edge with u and v are assumed to change linearly as described previously in Eq.(5.16). Hence, for each point on the side cutting edge, a proper contacting point on the grinding-wheel is calculated and the optimal grinding-wheel path is generated. This assumption can be verified by comparing the generated end-mill core with the designed one as shown in Fig. 5.15.

Now, to compare the flute profiles generated using this new approach and the inverse method, the profiles of these methods on the smaller tool end are plotted in

Figure 5.13: The simulation model of the tapered end-mill with the machined flutes by using the inverse method.

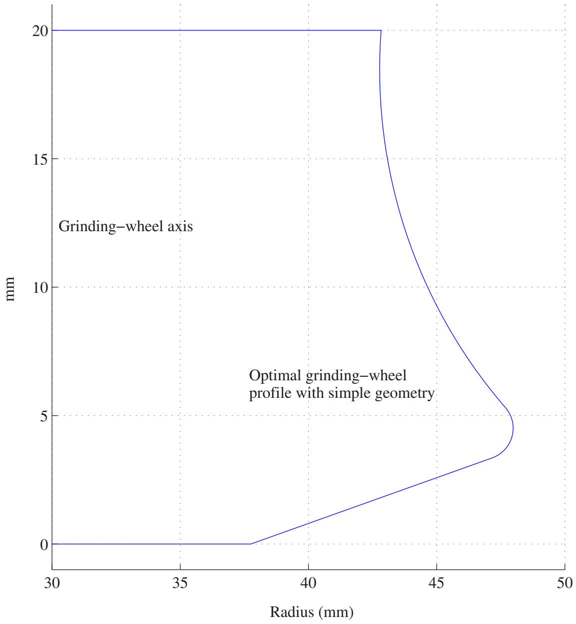

Figure 5.14: The revolving profile of the optimized grinding-wheel used to grind the tapered end-mill.

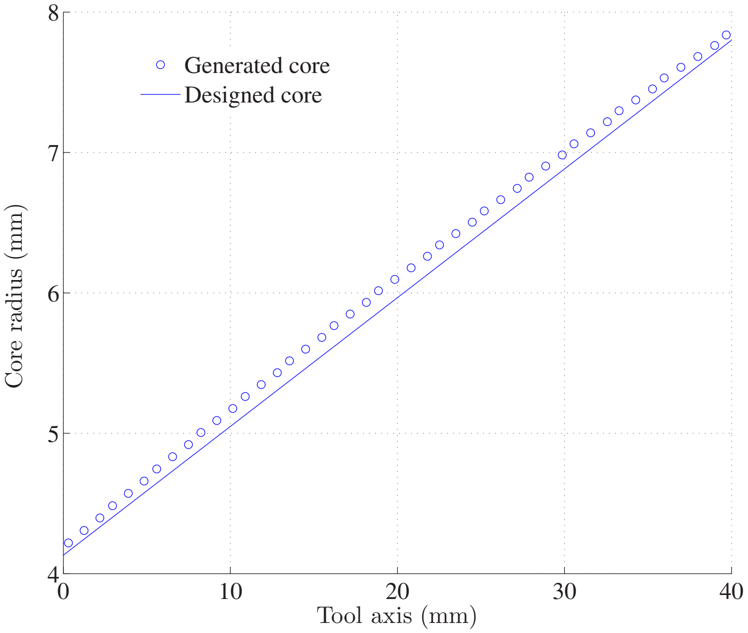

Figure 5.15: The end-mill core designed vs. generated using the proposed approach.

Fig. 5.16a together with the designed flute profile. It is evident that the flute profile of the inverse method is far from the designed profile, and the flute profile of the new approach is close to the designed one. The machining error curve is plotted in Fig. 5.16b. Since the maximum deviation is 0.3mm, a main reason is that the given flute profile is not reasonable, for example, the rake face cannot be a straight line. It is not possible for a grinding-wheel with simple geometries to generate such a rake face, unless the grinding-wheel profile is a free-form curve.

Also, in this example the flute profile generated using the new approach and the designed flute profile at the largest end-mill cross-section are compared and plotted in Fig. 5.17a. The machining error curve is plotted in Fig. 5.17b, and the maximum error is 0.322 mm. The simulation model of the tapered end-mill is provided in Fig.

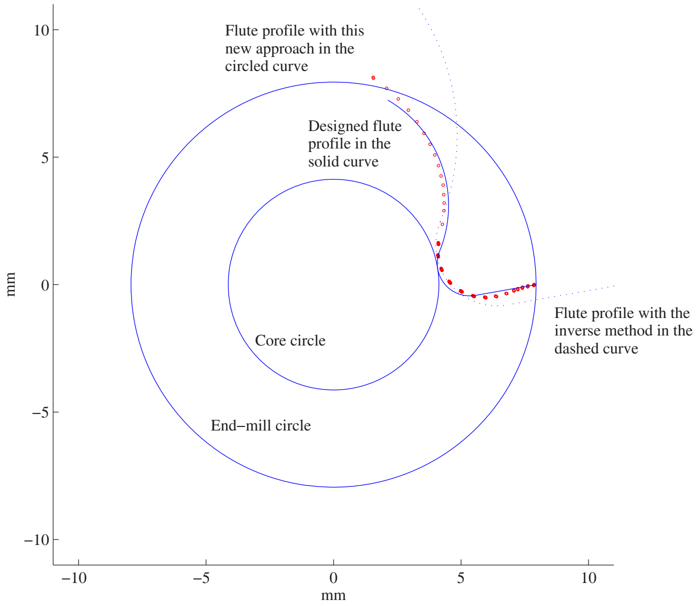

(a) The flute profiles generated with both the new approach and the inverse method vs. the designed one.

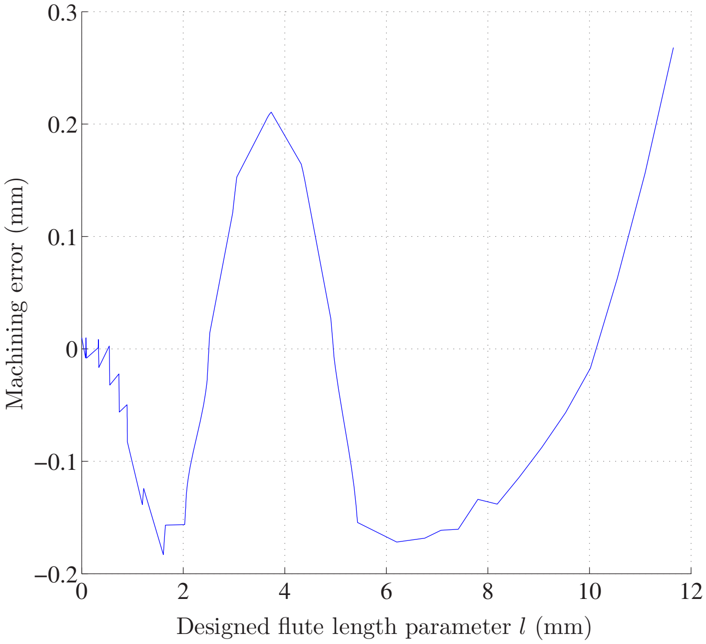

(b) The machining error curve between the flute profile generated with the new approach and the designed one.

Figure 5.16: Profile of the end-mill flute at the smaller cross-section

5.18.

5.6 Conclusion

The main objectives of the end-mill flutes are the chips evacuation, ensuring enough strength, reducing the vibration and extending the tool life. This leads to designing end-mill flute shapes that require accurate grinding. Beside satisfying this, the proposed method replaces the use of complex grinding-wheel shapes by simple ones and generates constant normal rake angles along the side cutting edge for better tool dynamics. This is conducted by exploiting the flexibility available in the 5-axis machining, where the grinding-wheel can change its orientation and location simultaneously to generate an accurate flute and satisfy, on the same time, the tangency condition between the contact point and the side cutting edge to produce end-mills with the the required normal rake angles.

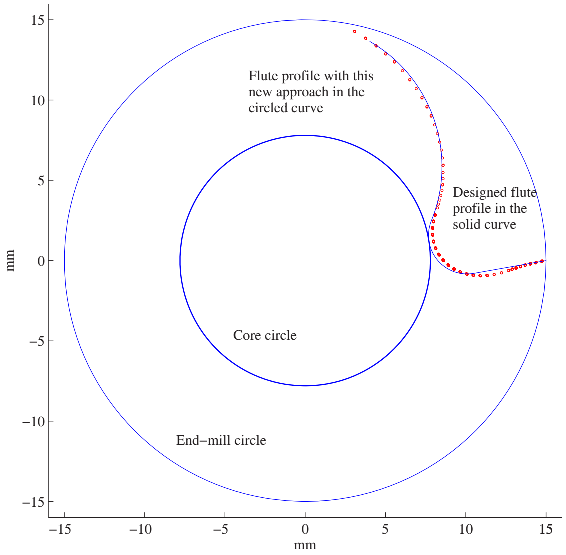

(a) The flute profiles generated with both the new approach and the inverse method vs. the designed one.

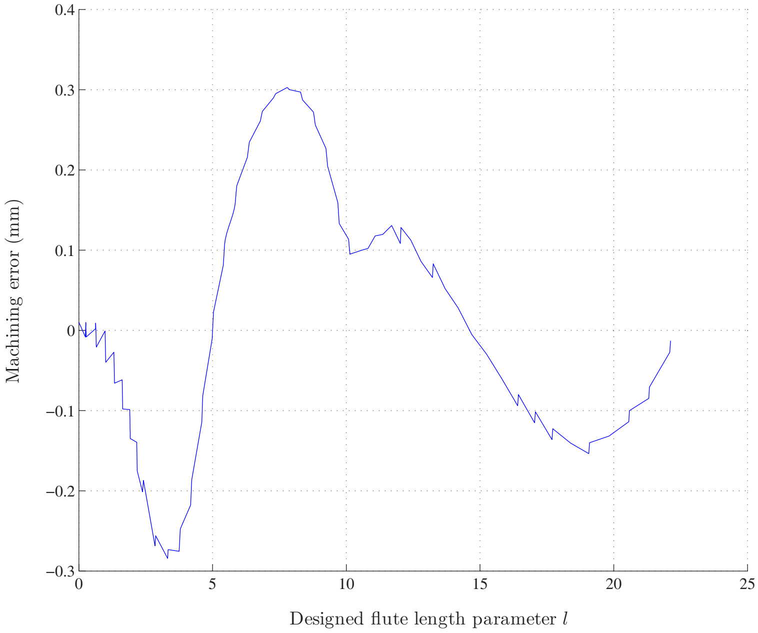

(b) The machining error curve between the flute profile generated with the new approach and the designed one.

Figure 5.17: Profile of the end-mill flute at the larger cross-section

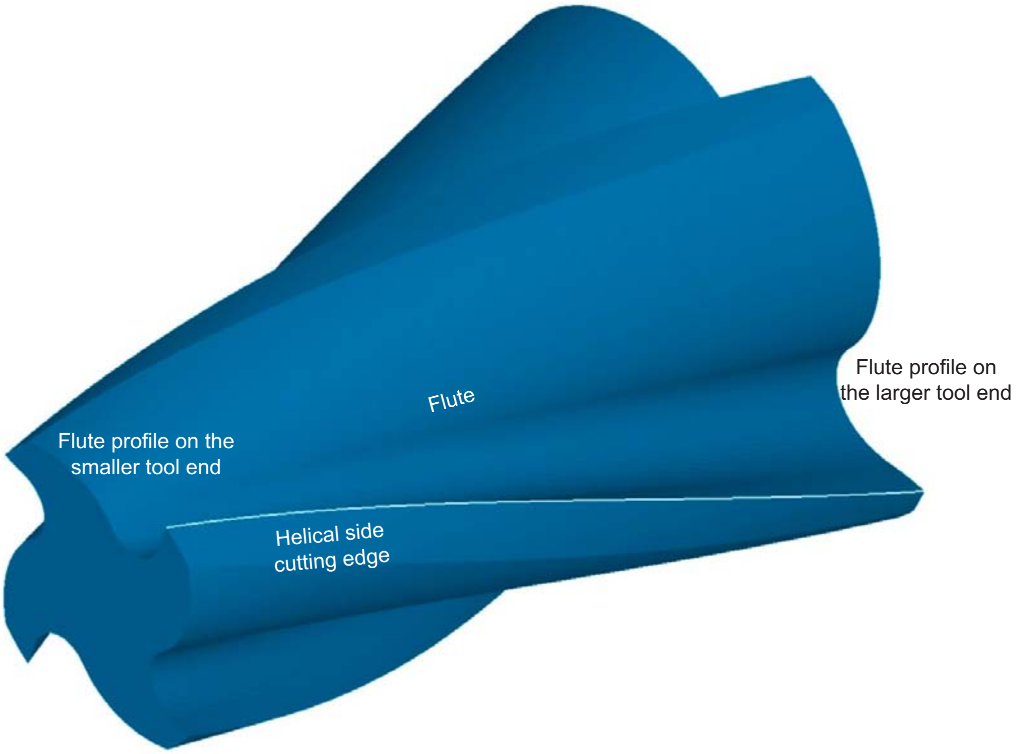

Figure 5.18: The model of the tapered end-mill in the proposed grinding approach simulation.

Chapter 6

Conclusions and Future Work

6.1 Summary

Two main methods are available in industry to grind the end-mills: the direct and the inverse method. In the direct method, standard grinding-wheels can be used in multi-axis CNC grinding machines to grind the end-mill flutes. The flute shapes will be the natural result of the process without any control. On the other side, the inverse method requires a free-form profile for the grinding-wheel to grind the end-mill flutes in a 2-axis grinding machine. While this method seems accurate, it is unable to produce accurate side cutting edges and constant normal rake angles for tapered end-mills. Hence, the need arose to develop new methods that can produce accurate flute shapes for better tool dynamics and life, in the same time, the side cutting edge should be accurate and the normal rake angle should be constant.

The new approach proposed in this dissertation introduces a simple shape of the grinding-wheel consisting of lines and circular arcs that grinds the end-mills with accurate flute shapes using 5-axis CNC machines. The side cutting edge obtained in this process is accurate and the normal rake angle is constant. This approach is developed by exploiting the tangency between the helical surface of the flute and the surface of the grinding-wheel. In other words, a point on the grinding-wheel must have its normal aligned with the normal of a point on the side cutting edge, and both points should be coincident. Doing this will build the basic foundation for the new 5-axis grinding theory proposed in this dissertation.

The geometric parameters of the grinding-wheel proposed and the location of the point on the grinding-wheel surface in contact with the side cutting edge can be optimized for better control on the flute shape along the side cutting edge. The result will be an optimal shape of the grinding-wheel moving along an optimal path to grind accurate end-mill flutes in 5-axis grinding machines.

The optimization algorithm used in this dissertation combines three well-known solvers (GA, DE and ASA) that work together to produce the optimal solution. The solvers share the same individuals after each generation to guarantee non pre-matured results and to eliminate the fine-tuning impact on the final solution.

A relationship between the normal rake angle and the radial rake angle is also established in this work. The importance of this relationship comes from the fact that the engineers mostly build their end-mill models based on the flute cross-sections. Thus, the radial rake angle is mostly the given, and converting this angle to a normal rake angle is required for this approach.

6.2 Future Work

Due to the importance of the tapered ball-end-mills in CNC machining, the future work will focus on building the CNC programming theory for these end-mills. The ground end-mills will have constant normal rake angles along the side cutting edges and the flutes shapes will be under control for better tool dynamics and life. Same principles can be used as those discussed in this work to achieve this goal. However, controlling the flute shape and avoiding gauging the side cutting edge in the ball section is not an easy task and is currently under research.

A general form of equations for the grinding-wheel locations and orientations will also be derived in order to grind flutes with constant normal rake angles for end-mills with free-form revolving profiles. This can be achieved by first representing the revolving profile of the end-mill as a NURBS curve. Then, the side cutting edge can be derived numerically, and the same procedure described in this dissertation can be followed to obtain this goal. However, side cutting edge gauging is still the main obstacle in achieving this goal and this will require more investigations and may lead to developing a side cutting edge gauging theory in 5-axis CNC end-mill grinding.

Finally, a real 5-axis CNC grinding can be conducted and the produced end-mills can be compared with those available in the market in two main criteria; these are: the vibration produced during cutting and the end-mill life. However, accomplishing this is based on the facilities that will be available in the future.

References

[1] Groover, M., 2007, "Fundamentals of modern manufacturing: materials, processes and systems," 3rd edition, Wiley, USA.

[2] Kalpakjian, S., and Schmid, S., 2006, "Manufacturing engineering and technology," 5th edition, Pearson prentice hall, USA.

[3] Rababah, M., and Chen, C., "Five axis CNC tool grinding, part I: rake face grinding," ASME 2011 International Manufacturing Science and Engineering Conference, Corvallis, Oregon, USA, June 13–17, 2011. (Accepted)

[4] Rababah, M., and Chen, C., "Five axis CNC tool grinding, part II: flute surface grinding," ASME 2011 International Manufacturing Science and Engineering Conference, Corvallis, Oregon, USA, June 13–17, 2011. (Accepted)

[5] Rababah, M., and Chen, C., "Automated and accurate CNC programming for five-axis grinding of tapered end-mill flutes using the direct method," Journal of Manufacturing Science and Engineering, Transactions of the ASME. (Submitted)

[6] Chen, C., and Rababah, M., "A Practical and optimal approach to CNC programming for five-Axis grinding of the prescribed end-mill flutes," CAD Computer Aided Design. (Submitted)

[7] Ferry, W.B., and Altintas, Y., 2008, "Virtual five-axis flank milling of jet engine impellers-part I: Mechanics of five axis flank milling," Journal of Manufacturing Science and Engineering, Transactions of the ASME, vol. 130, no. 1, pp. 011005–1-11.

[8] Ferry, W.B., and Altintas, Y., 2008, "Virtual five-axis flank milling of jet engine impellers-part II: Feed rate optimization of five-axis flank milling," Journal of Manufacturing Science and Engineering, Transactions of the ASME, vol. 130, no. 1, pp. 011013–1-13.

[9] Ferry, W.B., and Yip-Hoi, D., 2008, "Cutter-workpiece engagement calculations by parallel slicing for five-axis flank milling of jet engine impellers," Journal of Manufacturing Science and Engineering, Transactions of the ASME, vol. 130, no. 5, pp. 051011–1-12.

[10] Aras, A., and Yip-Hoi, D., 2008, "Geometric modeling of cutter-workpiece engagements in three-axis milling using polyhedral representations," Journal of computing and information Science in Engineering, Transactions of the ASME, vol. 8, no. 3, pp. 031007–1-13.

[11] Yip-Hoi, D., and Huang, X., 2006, "Cutter-workpiece engagement feature extraction from solid models for end milling," Journal of Manufacturing Science and Engineering, Transactions of the ASME, vol. 128, no. 1, pp. 249–260.

[12] Frey, D.D., Otto, K.N., and Pflager, W., 1997, "Swept envelopes of cutting tools in integrated machine and workpiece error budgeting," CIRP Annals -

Manufacturing Technology, vol. 46, no. 1, pp. 475–480.

[13] Wang, W.P., and Wang, K.K., 1986, “Geometric modeling for swept volume of moving solids,” IEEE Computer Graphics and Applications, vol. 6, no. 12, pp. 8–17.

[14] Sambandan, K., and Wang, K.K., 1989, “Five-axis swept volumes for graphic NC simulation and verification,” Advances in Design Automation, Publ. by ASME, Montreal, Canada, pp. 143–150.

[15] Chung, Y.C., Park, J.W., Shin, H., and Choi, B.K., 1998, “Generalized cutter for NC verification,” CAD Computer Aided Design, vol. 30, no. 8, pp. 587–94.

[16] Chiou, C., and Lee, Y., 2002, “Swept surface determination for five-axis numerical control machining,” International Journal of Machine Tools and Manufacture, vol. 42, no. 14, pp. 1497–1507.

[17] Weinert, K., Du, S., Damm, P., and Stautner, M., 2004, “Swept volume generation for the simulation of machining processes,” International Journal of Machine Tools and Manufacture, vol. 44, no. 6, pp. 617–628.

[18] Du, S., Surmann, T., Webber, O., and Weinert, K., 2005, “Formulating swept profiles for five-axis tool motions,” International Journal of Machine Tools and Manufacture, vol. 45, no. 7-8, pp. 849–861.

[19] Li, M.Z., Zheng, G., and Ding, H., 2009, “Formulating the swept envelope of rotary cutter undergoing general spatial motion for multi-axis NC machining,”

International Journal of Machine Tools and Manufacture, vol. 49, no. 2, pp. 199–202.

[20] Aras, E., 2009, “Generating cutter swept envelopes in five-axis milling by two-parameter families of spheres,” CAD Computer Aided Design, vol. 41, no. 2, pp. 95–105.

[21] Chen, Z.C., and Wei, C., 2008, “An efficient, accurate approach to representing cutter-swept envelopes and its applications to three-axis virtual milling of sculptured surfaces,” Journal of Manufacturing Science and Engineering, Transactions of the ASME, vol. 130, no. 3, pp. 0310041–03100412.

[22] Park, J.W., Shin, Y.H., and Chung, Y.C., 2005, “Hybrid cutting simulation via discrete vector model,” CAD Computer Aided Design, vol. 37, no. 4, pp. 419–430.

[23] Jerard, R.B., Hussaini, S.Z., Drysdale, R.L., and Schaudt, B., 1989, “Approximate methods for simulation and verification of numerically controlled machining programs,” Visual Computer, vol. 5, no. 6, pp. 329–48.

[24] Seung, R.M., Baek, N., Sung, Y.S., and Byoung, K.C., 2004, “A fast NC simulation method for circularly moving tools in the Z-map environment,” Geometric Modeling and Processing, IEEE Comput. Soc, Los Alamitos, CA, USA, pp. 319–328.

[25] Seung, R.M., Baek, N., Sung, Y.S., and Byoung, K.C., 2003, “A Z-map update method for linearly moving tools,” CAD Computer Aided Design, vol. 35, no. 11, pp. 995–1009.

[26] Chiou, J.C., 2007, "Virtual clay: an enhanced marching cubes algorithm for in-process geometry modeling," Journal of Manufacturing Science and Engineering, Transactions of the ASME, vol. 129, no. 3, pp. 566–74.

[27] Mann, S., and Bedi, S., 2002, "Generalization of the imprint method to general surfaces of revolution for NC machining," CAD Computer Aided Design, vol. 34, no. 5, pp. 373–378.

[28] Roth, D., Bedi, S., Ismail, F., and Mann, S., 2001, "Surface swept by a toroidal cutter during 5-axis machining," CAD Computer Aided Design, vol. 33, no. 1, pp. 57–63.

[29] Chappel, I.T., 1983, "The use of vectors to simulate material removed by numerically controlled milling," CAD Computer Aided Design, vol. 15, no. 3, pp. 156–8.

[30] Tandon, P., Gupta, P., and Dhande, SG., 2008, "Geometric modeling of fluted cutters," Journal of Computing and Information Science in Engineering, vol. 8, pp. 1–15.

[31] Tandon, P., and Khan, MR., 2009, "Three dimensional modeling and finite element simulation of a generic end mill," CAD Computer-Aided Design, vol. 41, pp. 106–114.

[32] Lu, Y., Takeuchi, Y., Takahashi, I., and Anzai, M., 2005, "An integrated system development for ball end mill design, creation and evaluation," International Journal of Advanced Manufacturing Technology, vol. 25, pp. 628–46.

[33] Tsai, Y., and Hsieh, J., 2001, “A study of a design and NC manufacturing model of ball-end cutters,” Journal of Materials Processing Technology, vol. 117, no. 1, pp. 183–192.

[34] Ren, B., Tang, Y., and Chen, C., 2001, “The general geometrical models of the design and 2-axis NC machining of a helical end-mill with constant pitch,” Journal of Materials Processing Technology, vol. 115, no. 3, pp. 265–270.

[35] Chen, W., Lai, H., and Chen, C., 2001, “A precision tool model for concave cone-end milling cutters,” International Journal of Advanced Manufacturing Technology, vol. 18, no. 8, pp. 567–578.

[36] Chang, W., and Chen, C., 2001, “Manufacturing models for the design and NC grinding of a revolving tool with a circular arc generatrix,” Journal of Materials Processing Technology, vol. 116, no. 2, pp. 114–123.

[37] Chen, W., and Chen, W., 2002, “Design and NC machining of a toroid-shaped revolving cutter with a concave-arc generator,” Journal of Materials Processing Technology, vol. 121, no. 2, pp. 217–225.

[38] Hsieh, C.M, 2008, “Manufacturing models for the design and NC grinding of truncated-cone ball-end cutters,” International Journal of Advanced Manufacturing Technology, vol. 35, no. 11, pp. 1124–1135.

[39] Han, C.S., Tang, Y.Y., and Dong, C., 2005, “A research on the non-NC machining of two kinds of revolving cutters,” Journal of Materials Processing Technology, vol. 161, no. 3, pp. 485–490.

[40] Hsieh, J.M., and Tsai, Y.C., 2006, “Geometric modeling and grinder design for toroid-cone shaped cutters,” International Journal of Advanced Manufacturing Technology, vol. 29, no. 9, pp. 912–921.

[41] Lin, S., and Lai, H., 2001, “A mathematical model for manufacturing ball-end cutters using a two-axis NC machine,” International Journal of Advanced Manufacturing Technology, vol. 17, no. 12, pp. 881–888.

[42] Chen, W.Y., Chang, P.C., Liaw, S.D., and Chen, W.F., 2005, “A study of design and manufacturing models for circular-arc ball-end milling cutters,” Journal of Materials Processing Technology, vol. 161, no. 3, pp. 467–77.

[43] Chen, C., Wang, F., Chang, P., Hwang, J., and Chen, W., 2006, “A precision design and NC manufacturing model for concave-arc ball-end cutters,” International Journal of Advanced Manufacturing Technology, vol. 31, no. 3, pp. 283–296.

[44] Chen, C., and Lin, R., 2001, “A study of manufacturing models for ball-end type rotating cutters with constant pitch helical grooves,” International Journal of Advanced Manufacturing Technology, vol. 18, no. 3, pp. 157–167.

[45] Lv, G.M., Wang, H.B., Tang, Y.Y., and Peng, L.G., 2004, “Cutting edge curve models for equal pitch cutters and their applications,” Journal of Harbin Institute of Technology, vol. 11, no. 1, pp. 46–48.

[46] Chen, W., 2004, “A mathematical solution to the design and manufacturing problems of ball-end cutters having a cutting edge with constant angle to the

axis," Proceedings of the Institution of Mechanical Engineers, Part C (Journal of Mechanical Engineering Science), vol. 218, no. 1, pp. 301–308.

[47] Engin, S., and Altintas, Y., 2001, "Mechanics and dynamics of general milling cutters. Part I: Helical end mills," International Journal of Machine Tools and Manufacture, vol. 41, no. 15, pp. 2195–2212.

[48] Kim, S.J., and Yang, M.Y., 2005, "Triangular mesh offset for generalized cutter," CAD Computer Aided Design, vol. 37, no. 10, pp. 999–1014.

[49] Kaldor, S., and Messinger, D., 1988, "On the CAD of profiles for cutters and helical flutes, geometrical aspects," Annals of the CIRP, vol. 37, no. 1, pp. 53–55.

[50] Sung, L., 1994, "Geometrical analysis of helical flute grinding and application to end mill," Transaction of NAMRI/SME, vol. 22, no. 1, pp. 165–172.

[51] Puig, A., Perez-vidal, L., and Tost, D., 2003, "3D simulation of tool machining," Computers and graphics, vol. 27, no. 1, pp. 99–106.

[52] Kim, Y., and Ko, S., 2002, "Development of design and manufacturing technology for end mills in machining hardened steel," Journal of Materials Processing Technology, vol. 130-131, no. 1, pp. 653–661.

[53] Chen, F., and Bin, H., 2009, "A novel CNC grinding method for the rake face of a taper ball-end mill with a CBN spherical grinding wheel," International Journal of Advanced Manufacturing Technology, vol. 41, no. 9, pp. 846–857.

[54] Feng, X., and Bin, H., 2003, “CNC rake grinding for a taper ball-end mill with a torus-shaped grinding wheel,” International Journal of Advanced Manufacturing Technology, vol. 21, no. 8, pp. 549–55.

[55] www.mathworks.com/matlabcentral/fileexchange.

Appendix A

Grinding–Wheel Orientation and Location for Cylindrical End-Mills

The side cutting edge for cylindrical end-mills of radius r_T can be expressed as

$$\mathbf{C}_\mathrm{C}^\mathrm{T} = \begin{bmatrix} r_\mathrm{T} \cdot \cos\theta_\mathrm{C} & r_\mathrm{T} \cdot \sin\theta_\mathrm{C} & \frac{r_\mathrm{T}}{\tan\psi} \cdot \theta_\mathrm{C} & 1 \end{bmatrix}^\mathrm{T} \tag{A.1}$$

Then, the wheel orientation is expressed by the angles μ and η as:

$$\mu = \begin{cases} \sin^{-1}\left(\frac{c}{\sqrt{a^2+b^2}}\right) - \phi \\ \pi - \sin^{-1}\left(\frac{c}{\sqrt{a^2+b^2}}\right) - \phi \end{cases} \tag{A.2}$$

where

$$\sin\phi = \frac{a}{\sqrt{a^2+b^2}}, \quad \cos\phi = \frac{b}{\sqrt{a^2+b^2}} \tag{A.3a}$$

$$\begin{aligned} a &= \cos\alpha_\mathrm{G} \\ b &= -\sin\alpha_\mathrm{G} \cdot \sin v \\ c &= \cos\alpha_\mathrm{n} \cdot \sin\psi \end{aligned} \tag{A.3b}$$

Also

$$\eta = \begin{cases} \eta_1 \quad \text{if} \quad \eta_1 = \eta_{3,4} \\ \eta_2 \quad \text{if} \quad \eta_2 = \eta_{3,4} \end{cases} \tag{A.4}$$

where

$$\eta_{1,2} = \begin{cases} \sin^{-1}\left(\frac{c_1}{\sqrt{{a_1}^2+{b_1}^2}}\right) - \phi_1 \\ \pi - \sin^{-1}\left(\frac{c_1}{\sqrt{{a_1}^2+{b_1}^2}}\right) - \phi_1 \end{cases} \tag{A.5}$$

where

$$\sin\phi_1 = \frac{a_1}{\sqrt{{a_1}^2+{b_1}^2}}, \quad \cos\phi_1 = \frac{b_1}{\sqrt{{a_1}^2+{b_1}^2}} \tag{A.6a}$$

$$\begin{aligned} a_1 &= \sin\alpha_{\mathrm{G}} \cdot \cos v \\ b_1 &= -\cos\alpha_{\mathrm{G}} \cdot \sin\mu - \cos\mu \cdot \sin\alpha_{\mathrm{G}} \cdot \sin v \\ c_1 &= -\cos\psi \cdot \cos\alpha_{\mathrm{n}} \cdot \sin\theta_{\mathrm{C}} + \cos\theta_{\mathrm{C}} \cdot \sin\alpha_{\mathrm{n}} \end{aligned} \tag{A.6b}$$

Also

$$\eta_{3,4} = \begin{cases} \sin^{-1}\left(\frac{c_2}{\sqrt{{a_2}^2+{b_2}^2}}\right) - \phi_2 \\ \pi - \sin^{-1}\left(\frac{c_2}{\sqrt{{a_2}^2+{b_2}^2}}\right) - \phi_2 \end{cases} \tag{A.7}$$

where

$$\sin\phi_2 = \frac{a_2}{\sqrt{{a_2}^2+{b_2}^2}}, \quad \cos\phi_2 = \frac{b_2}{\sqrt{{a_2}^2+{b_2}^2}} \tag{A.8a}$$

$$\begin{aligned} a_2 &= \cos\alpha_{\mathrm{G}} \cdot \sin\mu + \cos\mu \cdot \sin\alpha_{\mathrm{G}} \cdot \sin v \\ b_2 &= \sin\alpha_{\mathrm{G}} \cdot \cos v \\ c_2 &= \cos\psi \cdot \cos\alpha_{\mathrm{n}} \cdot \cos\theta_{\mathrm{C}} + \sin\theta_{\mathrm{C}} \cdot \sin\alpha_{\mathrm{n}} \end{aligned} \tag{A.8b}$$

Now the orientation of the wheel axis is expressed as

$$\mathbf{I}_{\mathrm{G}} = \mathrm{ROT}(\eta, z) \cdot \mathrm{ROT}(\mu, x) \cdot \begin{bmatrix} 0 \\ 0 \\ 1 \\ 0 \end{bmatrix} \tag{A.9}$$

The wheel location can also be obtained as

$$
\begin{aligned}
\mathrm{o}^{\mathrm{G}}_{\mathbf{x}^{\mathrm{T}}} &= r_{\mathrm{T}} \cdot \cos\theta_{\mathrm{C}} - u \cdot \sin\mu \cdot \sin\eta + \left(R_0 + \tfrac{u}{\tan\alpha_{\mathrm{G}}}\right) \cdot (\cos\mu \cdot \sin\eta \cdot \sin v - \cos\eta \cdot \cos v) \\
\mathrm{o}^{\mathrm{G}}_{\mathbf{y}^{\mathrm{T}}} &= r_{\mathrm{T}} \cdot \sin\theta_{\mathrm{C}} + u \cdot \sin\mu \cdot \cos\eta - \left(R_0 + \tfrac{u}{\tan\alpha_{\mathrm{G}}}\right) (\cos\mu \cdot \cos\eta \cdot \sin v - \sin\eta \cdot \cos v) \\
\mathrm{o}^{\mathrm{G}}_{\mathbf{z}^{\mathrm{T}}} &= \tfrac{\theta_{\mathrm{C}}}{\tan\psi} \cdot r_{\mathrm{T}} - u \cdot \cos\mu - \sin\mu \cdot \sin v \cdot \left(R_0 + \tfrac{u}{\tan\alpha_{\mathrm{G}}}\right)
\end{aligned}
\tag{A.10}
$$

Appendix B

Grinding–Wheel Orientation and Location for Tapered End-Mills

For the tapered flat end-mill shown in Fig. B.1, the side cutting edge is expressed as

$$\mathbf{C}_{\mathrm{C}}^{\mathrm{T}} = \begin{bmatrix} r_{\mathrm{T}}\left(z^{\mathrm{T}}\right) \cdot \cos\theta_{\mathrm{C}} & r_{\mathrm{T}}\left(z^{\mathrm{T}}\right) \cdot \sin\theta_{\mathrm{C}} & z^{\mathrm{T}} & 1 \end{bmatrix}^{\mathrm{T}} \tag{B.1}$$

where

$$r_{\mathrm{T}}(z^{\mathrm{T}}) = r_0 + z^{\mathrm{T}} \tan\varphi_{\mathrm{T}} \tag{B.2}$$

and

$$\theta_{\mathrm{C}}\left(z^{\mathrm{T}}\right) = \frac{\tan\psi}{\sin\varphi_{\mathrm{T}}} \cdot \left[\ln\left(\frac{r_0 + z^{\mathrm{T}} \cdot \tan\varphi_{\mathrm{T}}}{r_0}\right)\right] \tag{B.3}$$

Now the wheel orientation is expressed by μ and η as:

$$\mu = \begin{cases} \sin^{-1}\left(\frac{c}{\sqrt{a^2+b^2}}\right) - \phi \\ \pi - \sin^{-1}\left(\frac{c}{\sqrt{a^2+b^2}}\right) - \phi \end{cases} \tag{B.4}$$

where

$$\sin\phi = \left(\frac{a}{\sqrt{a^2+b^2}}\right), \quad \cos\phi = \left(\frac{b}{\sqrt{a^2+b^2}}\right) \tag{B.5a}$$

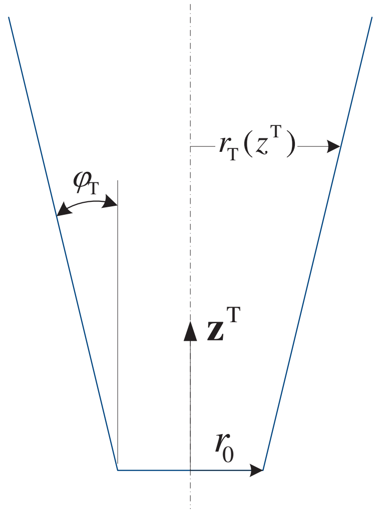

Figure B.1: Schematic of a general tapered end-mill.

$$\begin{aligned} a &= \cos\alpha_\mathrm{G} \\ b &= -\sin v \sin\alpha_\mathrm{G} \\ c &= \cos\alpha_\mathrm{n}\cos\varphi_\mathrm{T}\sin\psi + \sin\alpha_\mathrm{n}\sin\varphi_\mathrm{T} \end{aligned} \tag{B.5b}$$

And

$$\eta = \begin{cases} \eta_1 & \text{if} \quad \eta_1 = \eta_{3,4} \\ \eta_2 & \text{if} \quad \eta_2 = \eta_{3,4} \end{cases} \tag{B.6}$$

where

$$\eta_{1,2} = \begin{cases} \sin^{-1}\left(\frac{c_1}{\sqrt{{a_1}^2+{b_1}^2}}\right) - \phi_1 \\ \pi - \sin^{-1}\left(\frac{c_1}{\sqrt{{a_1}^2+{b_1}^2}}\right) - \phi_1 \end{cases} \tag{B.7}$$

where

$$\sin\phi_1 = \left(\frac{a_1}{\sqrt{{a_1}^2+{b_1}^2}}\right), \quad \cos\phi_1 = \left(\frac{b_1}{\sqrt{{a_1}^2+{b_1}^2}}\right) \tag{B.8a}$$

$$\begin{aligned} a_1 &= \sin\alpha_\mathrm{G}\cos v \\ b_1 &= -\cos\alpha_\mathrm{G}\sin\mu - \cos\mu\sin\alpha_\mathrm{G}\sin v \\ c_1 &= -\cos\psi\cos\alpha_\mathrm{n}\sin\theta_\mathrm{C} + \cos\theta_\mathrm{C}\sin\alpha_\mathrm{n}\cos\varphi_\mathrm{T} - \cos\alpha_\mathrm{n}\cos\theta_\mathrm{C}\sin\psi\sin\varphi_\mathrm{T} \end{aligned} \tag{B.8b}$$

and

$$\eta_{3,4} = \begin{cases} \sin^{-1}\left(\frac{c_2}{\sqrt{{a_2}^2+{b_2}^2}}\right) - \phi_2 \\ \pi - \sin^{-1}\left(\frac{c_2}{\sqrt{{a_2}^2+{b_2}^2}}\right) - \phi_2 \end{cases} \tag{B.9}$$

where

$$\sin\phi_2 = \left(\frac{a_2}{\sqrt{{a_2}^2+{b_2}^2}}\right), \quad \cos\phi_2 = \left(\frac{b_2}{\sqrt{{a_2}^2+{b_2}^2}}\right) \tag{B.10a}$$

$$\begin{aligned} &a_2 = \cos\alpha_{\mathrm{G}}\sin\mu + \cos\mu\sin\alpha_{\mathrm{G}}\sin v \\ &b_2 = \sin\alpha_{\mathrm{G}}\cos v \\ &c_2 = \cos\psi\cos\alpha_{\mathrm{n}}\cos\theta_{\mathrm{C}} + \sin\theta_{\mathrm{C}}\sin\alpha_{\mathrm{n}}\cos\varphi_{\mathrm{T}} - \cos\alpha_{\mathrm{n}}\sin\theta_{\mathrm{C}}\sin\psi\sin\varphi_{\mathrm{T}} \end{aligned} \tag{B.10b}$$

Now the orientation of the wheel axis is expressed as

$$\mathbf{I}_{\mathrm{G}} = \mathrm{ROT}(\eta, z)\cdot\mathrm{ROT}(\mu, x)\cdot\begin{bmatrix} 0 \\ 0 \\ 1 \\ 0 \end{bmatrix} \tag{B.11}$$

The wheel location can also be obtained as

$$\begin{aligned} &\mathrm{o}^{\mathrm{G}}_{\mathbf{x}^{\mathrm{T}}} = \left(r_0 + z^{\mathrm{T}}\tan\varphi_{\mathrm{T}}\right)\cos\theta_{\mathrm{C}} - u\sin\mu\sin\eta + \left(R_0 + \tfrac{u}{\tan\alpha_{\mathrm{G}}}\right)(\cos\mu\sin\eta\sin v - \cos\eta\cos v) \\ &\mathrm{o}^{\mathrm{G}}_{\mathbf{y}^{\mathrm{T}}} = \left(r_0 + z^{\mathrm{T}}\tan\varphi_{\mathrm{T}}\right)\sin\theta_{\mathrm{C}} + u\sin\mu\cos\eta - \left(R_0 + \tfrac{u}{\tan\alpha_{\mathrm{G}}}\right)(\cos\mu\cos\eta\sin v + \sin\eta\cos v) \\ &\mathrm{o}^{\mathrm{G}}_{\mathbf{z}^{\mathrm{T}}} = z^{\mathrm{T}} - u\cos\mu - \sin\mu\sin v\left(R_0 + \tfrac{u}{\tan\alpha_{\mathrm{G}}}\right) \end{aligned} \tag{B.12}$$